Spring 2022

Fundamental Study of Multiphase Solid/Molten Carbonate Membranes for CO_2 Capture and Conversion

Xin Li

FUNDAMENTAL STUDY OF MULTIPHASE SOLID/MOLTEN CARBONATE MEMBRANES FOR CO_2 CAPTURE AND CONVERSION

by

Xin Li

Bachelor of Science
Harbin University of Science and Technology, 2016

Master of Engineering
Northeastern University, 2019

Submitted in Partial Fulfillment of the Requirements

For the Degree of Doctor of Philosophy in

Mechanical Engineering

College of Engineering and Computing

University of South Carolina

2022

Accepted by:

Kevin Huang, Major Professor

Ralph White, Committee Member

Andrew Gross, Committee Member

Frank Chen, Committee Member

Tracey L. Weldon, Interim Vice Provost and Dean of the Graduate School

ACKNOWLEDGMENTS

First, I would like to express my sincere thanks to my advisor, Dr. Kevin Huang who brought me to this field and guided my research study and life with his broad knowledge, rich experience, and his patience. The experience of working with him was definitely a treasure of my life and will further affect me for my whole life. Also, I would like to convey my appreciation to Dr. Xinfang Jin, for her continuous help with my modeling work. Without their help, I will not be able to finish my thesis work in such a short time.

I would also like to convey my appreciation to my committee members, Dr. Andrew Gross, Dr. Frank Chen, Dr. Ralph White, for their invaluable advice and continuous help during my Ph.D. study, and my groupmate, Dr. Shichen Sun, Dr. Yeting Wen, Dr. Yongliang Zhang, Dr. Viki Mattick, and Qiming Tang, for their care and help in my study and life.

Also, I would like to express my special appreciation to Dr. Kitty Chang, Dr. David Shure, for taking care of me for the past three years.

ABSTRACT

Due to the burning of fossil fuels and human activities, many greenhouse gases such as carbon dioxide are released into the atmosphere, which causes global warming and has a significant negative impact on the human living environment. Therefore, it is imperative to develop carbon capture technologies that can prevent carbon dioxide emission and reduce carbon dioxide concentration in the air. Further, if the captured carbon dioxide can be converted back to fossil fuels, the emission of carbon dioxide is delayed, and more time is gained to develop new and advanced carbon free and clean energy technologies. Motivated by this thought, a multiphase carbonate membrane that can capture carbon dioxide from the point source and convert a fossil fuel such as methane into valuable chemicals with the captured carbon dioxide as a soft oxidizer has been proposed.

In this thesis, mathematical models of four types of solid/molten-carbonate CO_2 transport membranes were first developed with analytical and numerical approaches. These four types of membranes are mixed oxygen-vacancy and carbonate-ion conducting membrane (MOCC), mixed electron and carbonate-ion conducting membrane (MECC), mixed electron and oxygen-vacancy conducting/ molten carbonate dual-phase membrane (MOECC), and mixed electron and oxygen-vacancy conducting /metal/molten carbonate triple-phase membrane (MOEECC). The analytical solutions can be derived for two basic types of membranes, MOCC and MECC, and they agree well with numerical solutions.

For membranes with more charge carriers, numerical solutions are the only way to calculate flux since the analytical solutions cannot solve the nonlinear concentrations of charge carriers across the membrane. The models developed are the foundations for improving the membrane performance and designing next-generation high-performance CO_2 transport membranes. After validated by experimental data, a new type of plug flow chemical potential driven reactor based on MOEECC membrane was modeled and the results were compared with the co-fed fixed-bed reactor in terms of C2 yield, selectivity, and CH_4 conversion rate of the oxidative coupling of methane reaction. The overall results indicated the plug flow membrane reactors have much improved OCM performance over the co-fed fixed-bed reactor in terms of C2 yield and coking resistance.

A new kind of MOEECC membrane was also experimentally studied in this thesis. The oxygen flux was improved by Mn-doping CeO_2 (MDC) as a replacement of benchmark Sm-doped CeO_2. The upper limit of Mn-doping was determined by XRD to be 6mol%. The co-precipitation method was used to synthesize the nanosized power mixture of MDC and NiO, from which a porous MDC-NiO matrix was obtained after sintering at high temperatures. A eutectic molten carbonate (MC) was then allowed to fill the pores in the porous matrix and in-situ react with NiO to form electronically conducting LNO phase. The best MC loading was determined to be 0.1g for a matrix with 16% porosity, 0.916 cm^2 surface area and 0.75 mm thickness. With this membrane, the flux densities of CO_2 and O_2 were obtained and the CO_2 and O_2 pathways were confirmed by specially designed experiments.

TABLE OF CONTENTS

Acknowledgments iii

Abstract iv

List of Tables ix

List of Figures x

List of Symbols xv

List of Abbreviations xvi

Chapter 1 General Introduction: CO_2 Capture and Separation Technologies Overview 1

1.1 Introduction 1

1.2 CO_2 Capture Systems 2

1.3 CO_2 Capture Technologies 7

1.4 Methane Convert Process 15

1.5 Methane Convert Reactor Design 21

Chapter 2 Fundamental of High Temperature Multiphase CO_2 Capture and Conversion Membranes and Reactors 26

2.1 Working Principle of High-Temperature CO_2 Capture and Conversion Membranes 26

2.2 Newly Developed CO_2/O_2 co-Transport Membranes with Enhanced Electron Conduction 29

2.3 Theoretical Transport Flux Model for CO_2 Separation Membranes 32

Chapter 3 Synthesis and Characterization of High-Temperature CO_2 Transport Membranes 39

3.1 Synthesis of Porous Matrix and Membranes 39

3.2 Characterization Techniques for Porous Matrix and Membranes 44

3.3 Conclusion 59

Chapter 4 Analytical Solutions of High Temperature CO_2 Capture Membrane 61

4.1 Derivation of MOCC Analytical Solution 63

4.2 Derivation of MECC Analytical Solution 65

4.3 Derivation of MOECC Analytical Solution 67

4.4 Derivation of MDC/LNO/MC Membrane Analytical Solution 70

4.5 Conclusion 73

Chapter 5 Mathematical Modeling of High-Temperature Multiphase Solid/Molten Carbonate Membranes for CO_2 Capture 74

5.1 Introduction 75

5.2 Types of Membranes Modeled 78

5.3 Mathematical Models 78

5.4 Materials Property Data 88

5.5 Results and Discussion 90

5.6 Conclusion 101

Chapter 6 Performance Projection of a High Temperature CO_2 Transport Membrane Reactor for Combined CO_2 Capture and Methane-to-Ethylene Conversion 103

6.1 Introduction 104

6.2 Types of Reactors Simulated 106

6.3 Mathematical Models 107

6.4 Parameters and Model Validation 109

6.5 Set up for COMSOL Multiphysics 113

6.6 Results and Discussion 115

6.7 Conclusion 125

Chapter 7 Performance Projection of a High-temperature CO_2 transport Membrane Reactor for Methane-to-Syngas Conversion 127

7.1 Membrane reactor 128
7.2 Mathematical Models..... 129
7.3 Validation..... 131
7.4 Results and Discussion 133
7.5 Conclusion 136
Chapter 8 Concluding Remarks 137
References 140

LIST OF TABLES

Table 1.1 Materials and conditions in CO_2 absorption 9

Table 1.2 Details of different carbon species formed on the catalyst surface 21

Table 3.1 Feed gas compositions to verify the activation of three paths 59

Table 5.1 Governing equations and boundary conditions for different membranes..... 83

Table 5.2 Interfacial chemical reactions and equilibria 84

Table 5.3 Parameter definitions 84

Table 5.4 Analytical solutions of carbonate-ion flux* 85

Table 5.5 Materials properties under different gas compositions/temperatures 88

Table 5.6 Operating conditions and membrane parameter 90

Table 6.1 Reactions and kinetic rates 108

Table 6.2 Governing equations and boundary conditions for different domains 110

Table 6.3 Kinetic parameters for catalytic and bulk reactions..... 112

Table 6.4 Parameters and operating conditions for both fixed-bed and membrane reactors 112

Table 7.1 Reaction kinetics of all DOMR reactions 130

Table 7.2 Parameters and conditions of the DOMR validation 132

LIST OF FIGURES

Figure 1.1 Carbon capture and conversion cycle 2

Figure 1.2 Post-combustion CO_2 capture process 4

Figure 1.3 Schematic of pre-combustion capture process for power generation 5

Figure 1.4 Typical process flow diagram of an oxy-combustion system 6

Figure 1.5 Process flow diagram for CO_2 capture from flue gas by chemical absorption 8

Figure 1.6 Schematic of the membrane separation technology for CO_2 capture 10

Figure 1.7 Schematic of high temperature CO_2 transport membranes 13

Figure 1.8 Single chamber adsorption system 14

Figure 1.9 Two-chamber pressure adsorption system 15

Figure 1.10 Simplified reaction network of the oxidative coupling of methane at oxides 17

Figure 1.11 Pore plugging in a supported metal catalyst owing to carbon deposition 20

Figure 1.12 Schematic of fixed-bed reactors 22

Figure 1.13 Schematic of catalytic mixed conducting ceramic membrane reactors for various reactions 23

Figure 1.14 Schematic diagram of two-stage membrane reactor for syngas production .. 25

Figure 2.1 Transport principle of MOCC membranes 27

Figure 2.2 Transport principle of MECC membranes 28

Figure 2.3 Transport principle of MOECC membranes 29

Figure 2.4 Schematic working principle of the newly developed CO_2/O_2 co-transport membrane 30

Figure 2.5 Transport mechanism of high temperature CO_2/O_2 co-transport membrane .. 31

Figure 3.1 Synthesis steps for co-precipitation method 43

Figure 3.2 XRD patterns at different Mn doping amount in MDC 45

Figure 3.3 Microstructures of the MDC-NiO-MC membrane 46

Figure 3.4 The procedure of Archimedes porosity measurement 47

Figure 3.5 Schematic setup for Helium permeation and leak test 49

Figure 3.6 Experimental setup for Helium permeation and leak test 50

Figure 3.7 Helium permeation vs. average pressure 52

Figure 3.8 Conceptual schematic of four-probe measurement method 54

Figure 3.9 Arrhenius plots for different MDCs in air and hydrogen atmosphere 55

Figure 3.10 Schematic of the CO_2 permeation cell configurations 57

Figure 3.11 Flux measurement of membrane with different amount molten carbonate: (a) 0.25g molten carbonate; (b) 0.1g molten carbonate; (c) 0.05g molten carbonate 57

Figure 3.12 Flux comparison of the membrane with different molten carbonate amounts 58

Figure 3.13 Arrhenius plot for O_2 and CO_2 flux 58

Figure 4.1 Transport mechanisms in different membranes: (a)MOCC; (b)MECC; (c)MOECC; (d)MOEECC 62

Figure 5.1 Steps of model build-up process 79

Figure 5.2 Total conductivity comparison among different materials 89

Figure 5.3 Numerical and analytical results of MOCC membrane at different temperatures with a fixed permeate-side pCO_2=0.1 atm:(a) CO_2 flux; (b) electric potential in MC phase; (c) electric potential in SO (8YSZ) phase 93

Figure 5.4 Numerical and analytical results of MOCC membrane under different permeate-site pCO_2 at a fixed T=800°C: (a) CO_2 flux; (b) electric potential in MC phase; (c) electric potential in SO (8YSZ) phase 93

Figure 5.5 CO_2 flux($mol/cm^2/s$), comparison between YSZ/MC and GDC/MC membranes;(a) different operating temperature, (°C) with a fixed permeate-side pCO_2=0.1 atm; (b) different permeate-side CO_2 partial pressures, (atm) with a fixed T=800°C 94

Figure 5.6 Numerical and analytical results of MECC (Ag/MC) membrane at different temperatures with a fixed permeate-side pCO_2=0.1atm: (a) CO_2 and O_2 flux; (b) electric potential in metal (Ag) phase; (c) electric potential in MC phase 95

Figure 5.7 Numerical and analytical results of MECC membrane under different permeate-site pCO_2 at a fixed T=800°C: (a) CO_2 flux; (b) electric potential in metal phase; (c) electric potential in MC phase 96

Figure 5.8 Transmembrane concentration profiles of electron holes and oxygen vacancies in LSCF/MC membrane under different permeate-side pCO_2 and a fixed T=800°C: (a) electron holes; (b) oxygen vacancies 97

Figure 5.9 Comparison of transmembrane fluxes of LSCF/MC membrane under different permeate-side pCO_2 and a fixed T=800°C derived from numerical and analytical methods: (a) O_2 flux; (b) oxygen vacancy flux; (c) CO_2 flux 98

Figure 5.10 Comparison of transmembrane fluxes of LSCF/MC membrane derived from numerical and analytical methods vs different permeate-side pCO_2 and a fixed T=800°C: (a)CO_2 flux; (b) oxygen vacancy flux; (c) O_2 flux 99

Figure 5.11 Breakdown of numerical CO_2 and O_2 fluxes of membrane under different permeate-side pCO_2 and a fixed T=800°C: (a) CO_2 flux; (b) O_2 flux; (c) CO_2/O_2 ratio 100

Figure 5.12 Comparison of numerical CO_2 and O_2 fluxes of membrane with and without LNO phase at different temperatures and a fixed permeated side pCO_2=0.1 atm: (a) CO_2 flux; (b) O_2 flux; (c) CO_2/O_2 ratio 101

Figure 6.1 Schematic illustration of (a) membrane reactor; (b) co-fed fixed bed 107

Figure 6.2 Validation of the reactors: (a) CO_2 flux validation of the membrane; (b) validation of O_2 OCM for the fixed catalyst bed in C2 yield; (c) validation of O_2 OCM for the fixed catalyst bed in CH_4 conversion rate; (d) Validation of CO_2 OCM for the fixed catalyst bed 111

Figure 6.3 Mesh of the 2-D model of the tubular membrane reactor 115

Figure 6.4 2D axial symmetric gas species molar fraction profiles in the fixed-bed reactor under 1103K 116

Figure 6.5 Molar fractions of gas species in the co-fed fixed-bed reactor along the z axis under: (a) 973K; (b) 1023K; (c) 1103K 117

Figure 6.6 Reaction rates in the fixed-bed reactor along the z axis under:(a) 973K; (b) 1023K; (c) 1103K 118

Figure 6.7 2D axial symmetric gas species molar fraction profiles in the membrane reactor under 1103K 119

Figure 6.8 Molar fractions of gas species in the membrane reactor along the z-axis under: (a) 973K; (b) 1023K; (c) 1103K 120

Figure 6.9 Reaction rates in the membrane reactor along the z-axis under: (a)973K; (b)1023K; (c)1103K 120

Figure 6.10 Performance comparison between membrane and fixed-bed reactors: (a) C2 yield; (b) C2 selectivity; (c) CH_4 conversion rate 121

Figure 6.11 (a) CO_2 flux along the gas/membrane interface in the membrane reactor; (b) CH_4 molar fraction comparison between membrane and fixed-bed reactors 122

Figure 6.12 C2 yield as a function of reactor length 123

Figure 6.13 Coking selectivity as a function of operating temperature 124

Figure 6.14 C2 yield increase for membrane reactor and fixed-bed reactor considering the OCM by CO_2 125

Figure 7.1 Schematic of the membrane reactor for dry-oxy reforming 129

Figure 7.2 Validation of the DOMR kinetics for the membrane reactors with Zhang's data 132

Figure 7.3 Molar fractions profiles of (a) CH_4; (b) Gas species produced from the DMR and DOME reactions 133

Figure 7.4 2D axial symmetric gas species molar fraction profiles in the membrane reactor under 1023K for the dry reforming reaction 134

Figure 7.5 2D axial symmetric gas species molar fraction profiles in the membrane reactor under 1023K for the DOMR reactions 134

Figure 7.6 Reaction rates of the DOMR reactions under 1023K 135

LIST OF SYMBOLS

C	Molar concentration, $mol \cdot m^{-3}$
D	Diffusion coefficient, $cm^2 \cdot s^{-1}$
E_a	Activation energy, J/mol
F	Faraday's constant, 96485 C/mol
ΔH	Enthalpy, J/mol
J	Current, $A \cdot cm^{-2}$
J_i	Flux of species i, $mol \cdot cm^{-2} \cdot s^{-1}$
K	Equilibrium constant, $mol^9 \cdot cm^{-9} \cdot atm^{1/2}$
N	Molar flux, $mol \cdot cm^{-2} \cdot s^{-1}$
P	Partial pressure, atm
R	Ideal gas constant, 8.314 J K^{-1} mol^{-1}.
T	Temperature, K
V	Volume ratio
Z	Charge
ε	Volume fraction of molten carbonate
σ	Conductivity, $S \cdot m^{-1}$
Φ	Electric potential, V
μ	Chemical potentials, $J \cdot mol^{-1}$
δ	Oxygen vacancy fraction
τ	Tortuosity

LIST OF ABBREVIATIONS

ASU ..... Air Separation Unit

CCS ..... Carbon Capture and Storage

COTM ..... CO_2/O_2 co-Transport Membrane

DMR ..... Dry Methane Reforming

IGCC ..... Integrated Gasification Combined Cycle

MOCC ..... Mixed Oxide-ionic and Carbonate-ionic Conductor

MECC ..... Mixed Electronic and Carbonate-ionic Conductor

MOECC ..... MOEC/MC double-phase membrane

MOEECC ..... MOEC/Metal/MC triple-phase membrane

MC ..... Molten Carbonate

OCM ..... Oxidative Coupling of Methane

PSA ..... Pressure Swing Adsorption

SDC ..... Samarium doped CeO_2

SO ..... Solid Oxide

TMDC ..... Transition Metal Doped CeO_2

TSA ..... Temperature Swing Adsorption

WGS ..... Water Gas Shift

YSZ ..... Yttria-Stabilized Zirconia

CHAPTER 1

GENERAL INTRODUCTION: CO_2 CAPTURE AND SEPARATION TECHNOLOGIES OVERVIEW

1.1 INTRODUCTION

Carbon dioxide is a vital chemical gas found in the atmosphere. It can support the continuous life on the earth by participating in plant photosynthesis and keeping the atmosphere warm. However, when carbon dioxide is present in excess, it threatens our lives. Deforestation, agriculture, and fossil fuel use are the primary sources of carbon dioxide emission. With the frequent occurrence of various extreme climate phenomena worldwide, the threat of global climate change caused by high levels of CO_2 and other greenhouse gases in the atmosphere is increasing day by day. China, the United States, India, Russia, and Japan are the top five carbon emitters. The biggest source of carbon dioxide emissions for these countries is the electricity sector, especially coal fired power plants. It has become a global consensus to promote greenhouse gas emission reduction jointly. At the same time, with the population growth and economic growth, solving the energy shortage becomes more and more urgent. Therefore, coming up with the idea that captures CO_2 and efficiently converts CO_2 into sustainable fuels as a delay strategy to CO_2 emission is a win-win strategy. Based on this background, the concept of CCS (Carbon Capture and Storage) was proposed in 1977 and developed for over 40 years[1]. CCS is defined as a process consisting of the separation of CO_2 from industrial and

energy-related carbon sources, transport to a storage location and long-term isolation from the atmosphere. A typical CO_2 conversion cycle can be shown in Figure 1.1[2]. The CCS practice technically involves capturing carbon dioxide from power plants, industrial sites, and natural gas wells and transporting it through pipelines or ground transportation to a favorable geological site for permanent storage. It has been suggested that CO_2 could be captured from the coal-fired power plant and injected into suitable geological formations. Over the past decades, CCS technology has gained a lot of attention and development. Several carbon capture systems are associated with different combustion processes, and some advanced carbon separation technologies have been developed.

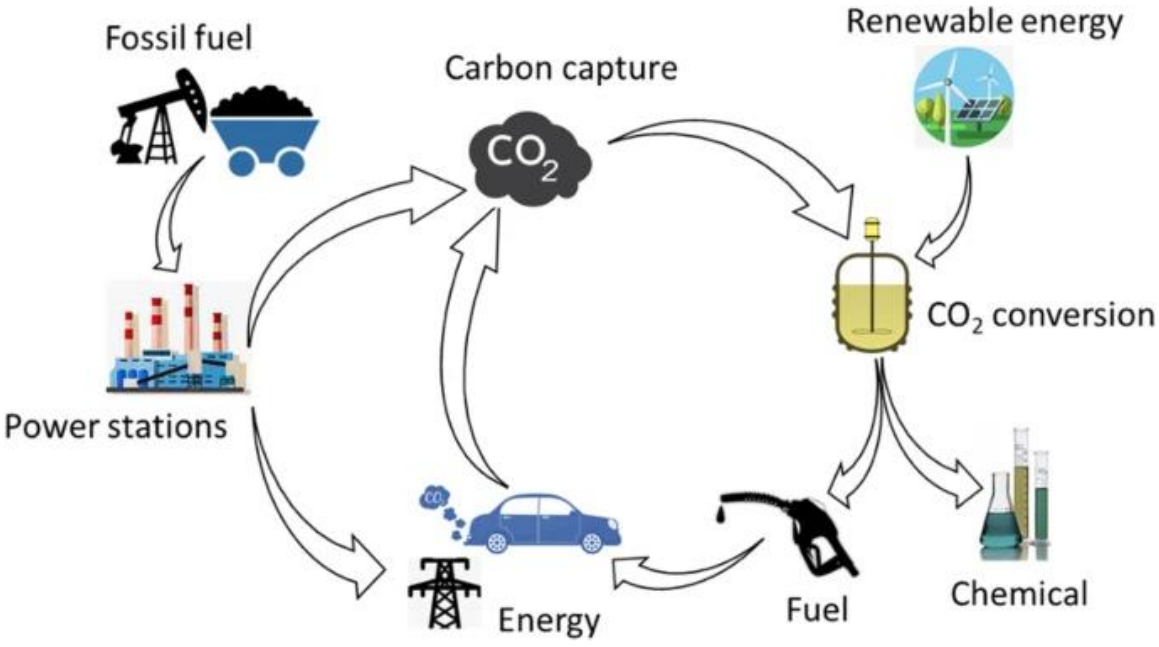

Figure 1.1 Carbon capture and conversion cycle [2]

1.2 CO_2 CAPTURE SYSTEMS

There are three main carbon capture systems available in the market: post-combustion systems, pre-combustion systems, and oxy-fuel systems.

1.2.1 Post-combustion capture systems

Post-combustion capture process captures carbon dioxide from a flue gas generated after the fuel has been fully burned with air. The process of post-combustion capture is shown in Figure 1.2. The mixture of carbon dioxide, nitrogen, sulfur dioxide, and oxygen are treated to remove the oxides of nitrogen and sulfur first and then contact a liquid solvent for removing CO_2. Generally, post-combustion capture systems include absorption in solvents, adsorption by solid sorbents, cryogenic distillation, and membrane separation. The post-combustion capture method is relatively mature in technical applications and can generally meet the needs of conventional fossil fuel power plants. The key advantages of post-combustion capture technology are its wide application area and simple system principle. It could be built or retrofit with existing industrial plants and power stations without significant modifications to the original design. The post-combustion capture technology also has high operational flexibility and lower technology risk than other existing technologies. What is more, renewable energy could be integrated with the post-combustion capture technologies and capture carbon dioxide from significant stationary sources of CO_2 such as natural gas-fired power stations. However, the post-combustion capture technology is not widely used in practice, mainly because of the challenges of separating the relatively low concentration of carbon dioxide from the large volumes of N_2 in the flue gases. Also, the typically 4% CO_2 contained in the flue gas from natural gas fired power plants reduces the driving force for CO_2 separation, requiring more energy input. In addition, the investment and operating costs of carbon capture equipment are high, which makes CO_2 capture more expensive.

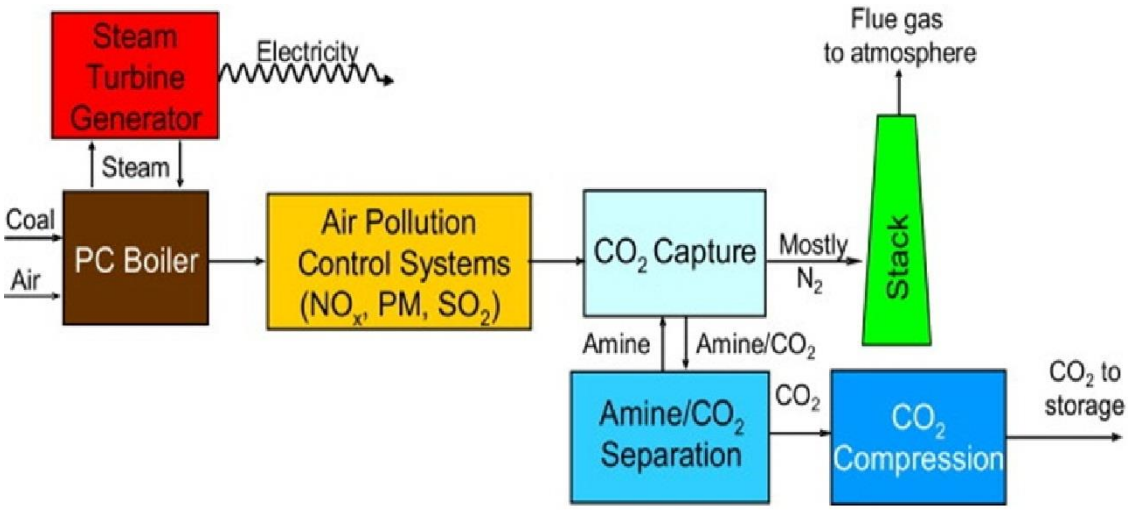

Figure 1.2 Post-combustion CO_2 capture process[3]

1.2.2 Pre-combustion capture systems

Pre-combustion capture refers to capturing CO_2 generated as an undesired co-product of an intermediate reaction of a conversion process. In short, it is the separation of CO_2 before the burning of fossil fuels. Typically, in the pre-combustion capture systems, fuel is converted by oxygen or steam to get a mixture of H_2, and CO. CO is then reacted with steam in a catalytic reactor to produce CO_2 and more H_2. The CO_2 produced is then separated from H_2, usually by physical or chemical absorption. Finally, a hydrogen-rich fuel could be obtained and used in many applications such as boilers, refining, gas turbines, engines, and fuel cells[4]. An example of a representative pre-combustion capture technology is the integrated gasification combined cycle (IGCC), which converts coal to syngas. In an IGCC power plant, CO_2 must be separated from hydrogen using physical solvents or porous polymeric membranes. For the pre-combustion capture systems, a key benefit is the high concentration of CO_2 in the output stream, which makes pre-combustion CO_2 capture more efficient. It can be applied to

high CO_2 emitting industries such as chemicals (gas and coal-based) and iron and steel making. Compared with post-combustion carbon capture technology, pre-combustion carbon capture is more efficient since water-gas-shift (WGS) reaction is usually used to shift syngas to generate higher concentration of CO_2 from CO.

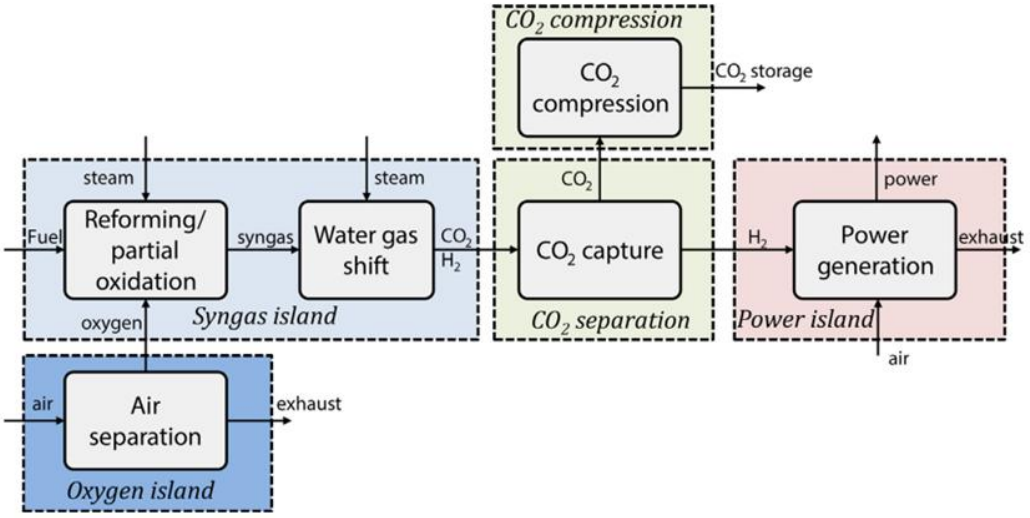

Figure 1.3 Schematic of pre-combustion capture process for power generation [5]

1.2.3 Oxy-fuel combustion systems

Oxy-fuel combustion is currently considered one of the major technologies for CO_2 capture. It includes three main components: the air separation unit (ASU) that provides O_2 for combustion, the furnace and heat exchangers where combustion and heat exchange occur, and the CO_2 capture and compression unit. Pure O_2 is used for fuel combustion in oxy-fuel combustion, thereby producing a CO_2-enriched flue gas ready for sequestration once water is condensed from the flue gas and other impurities are removed. Compared with other carbon capture systems, NO_x formation in oxy-firing is significantly lower due to the use of N_2-free pure O_2 as well as re-cycling of flue gas. Furthermore, the flue gas volume from oxy-firing is significantly lower than any other

system since oxygen is used for the combustion process instead of air. This, in turn, results in a need for much smaller flue gas emissions control equipment, leading to cost savings. Oxy-power plants incorporate mature technologies at an industrial scale but have not been deployed at a scale suitable for the electric power industry due to the high energy costs associated with oxygen production, requirement for exotic materials to withstand the high O_2 environment. Therefore, one next step in improving the oxy-fuel combustion is a step-change technology for oxygen production. It will bring the cost of oxy-fuel combustion down significantly.

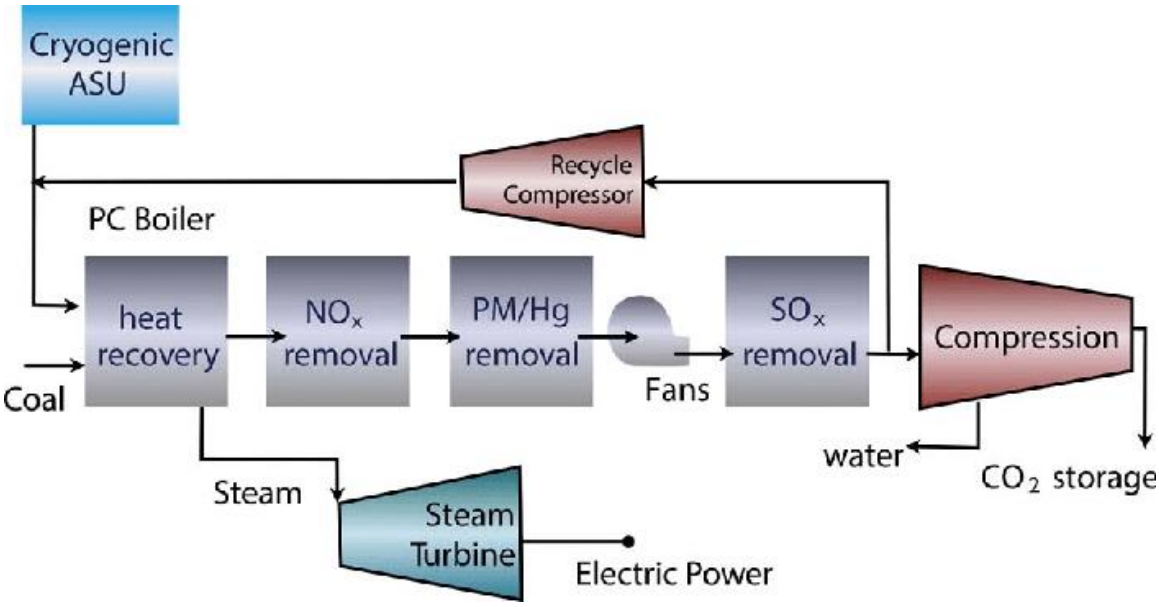

Figure 1.4 Typical process flow diagram of an oxy-combustion system[6]

Pre-combustion and oxyfuel power plants have better performance in some environmental impact categories since they require less coal and result in less emissions and wastes production. The pre-combustion systems have been proven to have the least environmental impact because the flue gas can be fully purified by removing the heavy-metal and benzene. Similarly, oxy-fuel combustion systems also show less environmental

impact since most of the particles are removed in the electrostatic precipitator, flue gas desulphurization and CO_2 compression and purification units. Post-combustion capture can be easily adapted to the existing plant so it has the simplest implement but the gas stream is much diluted in CO_2, making it costly to capture[7]. Overall, all these three technologies can achieve the goal of reducing CO_2 emissions and thus reducing the impacts of global warming.

1.3 CO_2 CAPTURE TECHNOLOGIES

Both pre-combustion and post-combustion involve the separation of CO_2 from a gas mixture of different compositions.

1.3.1 Chemical absorption

Chemical absorption involves CO_2 react with a chemical solvent to form a weakly bonded intermediate compound which may be regenerated with the application of heat, producing the original solvent and a pure CO_2 stream. The typical plant for post-combustion CO_2 capture by chemical absorption is shown in Figure 1.5. Before entering the absorber column at the bottom, the flue gas is cooled first. Then CO_2 is absorbed by a chemical solvent in aqueous solution in counter-flow manner when the flue gas rises in the column. To increase the contact area between gas and liquid phase, the column is filled with random or structured packing. At the top of the absorber, there is a washing section contacting the gas with cold water to help reduce the slip of solvent to the environment. To overcome the additional pressure losses in the flue gas path, an induced draft is required. The treated CO_2-free flue gas is released to the atmosphere from the top of the absorber. The absorbed CO_2 is stripped from the rich solution in a separate column.

The CO_2-rich solution is gathered at the bottom of the absorber and pumped to the desorber and passing a preheated heat exchanger to a required temperature. In the desorber, the CO_2-rich solution releases the captured CO_2. A counter-flow of vapor generated in the reboiler consisting mainly of steam and CO_2 deliver the partial pressure difference and heat for the CO_2 separation. The CO_2-rich gas is cooled, and part of the water vapor is condensed at the top of the desorber. The remaining gas can be compressed and then ready for transportation to a storage site. At the bottom of the reboiler, the CO_2-lean solution is gathered and returned to the absorber, passing the heat exchanger and cool down to the desired absorber temperature. The process cycle is closed by disperse the lean solution at the top of the absorber column.

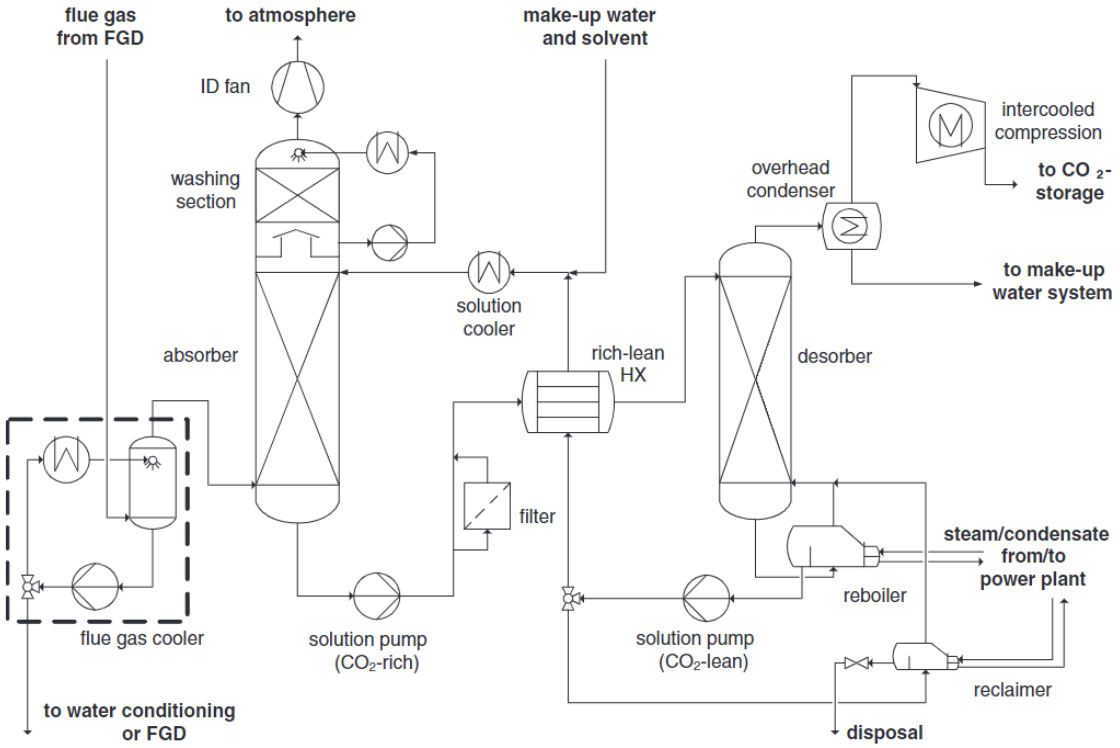

Figure 1.5 Process flow diagram for CO_2 capture from flue gas by chemical absorption[8]

The requirements for CO_2 capture by chemical absorption including high inherent CO_2 capacity per weight of solvent, high absorption rate, low cost, non-corrosive behavior, no degradation under the operating conditions of the absorber and desorber, low vapor pressure, low viscosity, non-toxic and non-hazardous. The maximum amount of CO_2 can be absorbed is determined by the inherent CO_2 capacity of the solvent. The less solution needed to absorb the more CO_2 is more beneficial for the reboiler heat requirement and the solution pumps power demand.[9] The most commonly used materials and conditions in CO_2 absorption process is shown in Table 1.1 [10]

Table 1.1 Materials and conditions in CO_2 absorption [10]

Absorbent	Absorption temp (^oC)	Absorption pressure(atm)	Desorption temp (^oC)	Desorption pressure(atm)	Cost ($/ton CO_2)
MEA	50	2.24	120	1	13.9
MEA (with Fe)	55	1	120	1	None reported
PSR	50	2.24	110	1	None reported
K_2CO_3	45	1	55	0.15	None reported

Chemical absorption technology has the advantage of suitable for retrofitting of the existing power plants and it has been commercialized for many years. However, it also shows some disadvantages such as low CO_2 loading capacity, high equipment

corrosion rate and amine degradation and high energy consumption etc. The possible approaches to solve these drawbacks focus on the improvement of absorbents and operations.[11]

1.3.2 Membrane-based CO_2 separation

Both pre-combustion and post-combustion CCS involve the separation of CO_2 form a gas mixture, composed of CO_2 and H_2 in the first step and CO_2 diluted in air and other combustion gases, such as sulfur dioxide and nitrogen oxides in post-combustion flue gas. Membrane-based CO_2 separation process in recent years appears to be a competitive substitution for conventional chemical absorption technology. The schematic of a membrane separation process is shown in Figure 1.6.[12]

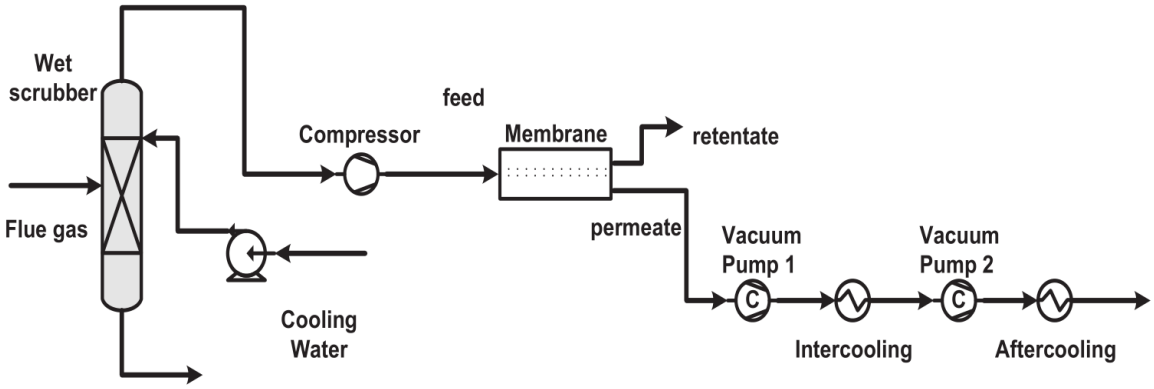

Figure 1.6 Schematic of the membrane separation technology for CO_2 capture [12]

When using the membrane separation technology for CO_2 capture, the flue gas is usually cooled down to the operational temperature of the membrane by a wet scrubber before entering the membrane module. A portion of CO_2 permeate through the membrane in the membrane module and at the permeated side, a higher CO_2 concentration is gained with retentate gas left in the flue gas.

The membrane materials play an important role in separating CO_2 from flue gas. Two major properties should be taken into consideration, which are permeability and selectivity. Permeability affects the separation efficiency, and the selectivity determines the CO_2 purity in the permeate gas. Membranes being investigated including polymer membranes, mixed matrix membranes, carbon molecular sieve membranes and inorganic membranes. Each membrane material has its own separation property, thermal and chemical stability and mechanical strength, thus has its own advantages and challenges related to performance, cost and lifetime. Polymer membranes have the advantages of good separation performance, good mechanical stability and low cost. Commercial polymeric gas separation membranes are mostly made from cellulose acetate (UOP, GMS, NATCO), polysulfone (Air Products), and polyimides (Praxair), polyphenylene oxide (Parker-Hanni-fin), and polydimethylsiloxane (GKSS, MTR). Microporous organic polymers have large surface area and attracted many research interests. The first reported polyimide-based thermally rearranged polymers is prepared by Park et al with an average pore size of 0.4-0.9nm[13]. This membrane has flexible structures and excellent gas separation performance under high-pressure[14, 15] and high temperature condition[16]. Another type of microporous polymer materials of PIMS (polymers of intrinsic microporosity) has the advantages of slow physical aging, high gas permeability and high selectivity. Budd et al reported a high surface area of 600-900 m^2/g and a 22-24% high fractional free volume of PIMS[17]. To improve separation performance of common polymer membranes, rigid permeable or impermeable particles are dispersed in a continuous polymeric phase to form mixed matrix membranes[18]. Mixed matrix membrane with microporous fillers could improve selectivity and might get an increased

permeability as well, while adding nonporous nanoparticles can improve gas permeability[19].

For high temperature CO_2 capture and conversion, a ceramic CO_2 transport membrane consists of a porous solid phase scaffold infiltrated with a molten carbonate phase has been studied. The porous solid oxide phase conduct ions and electrons and work as placeholder for the molten carbonate phase. The molten carbonate phase acts as the carbonate ionic conductor and gas sealant. Based on the charge carriers of the solid oxide phase, the high temperature CO_2 transport membrane can be divided into three categories: (1) MOCC (mixed oxide-ionic and carbonate-ionic conductor membrane), (2) MECC (mixed electronic and carbonate-ionic conductor membrane), (3) MEOCC (mixed electronic, oxide-ionic and carbonate-ionic conductor membrane). The mechanisms of the membranes are shown in Figure 1.7[20]. Zhang et al developed a mixed-conducting, triple phase membrane for high temperature and high selective CO_2/O_2 capture and in situ conversion of methane into syngas via dry-oxy methane reforming. The membrane composed of a porous NiO-SDC matrix filled with molten carbonate. The membrane achieved a flux density of CO_2 and O_2 of 1.17mL min^{-1} cm^{-2} and 0.52 mL min^{-1} cm^{-2}, respectively at 850^{o}C with Ar as the sweep gas and a CH_4 conversion rate of 84.1% with CH_4-Ar as the sweep gas for the dry-oxy methane reforming[21].

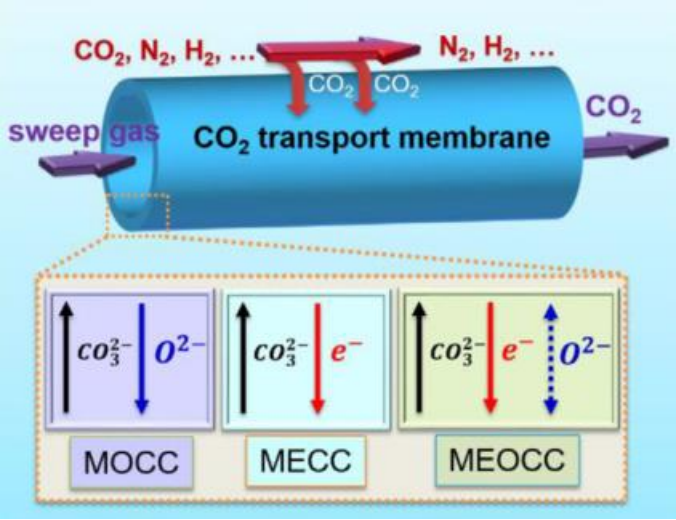

Figure 1.7 Schematic of high temperature CO_2 transport membranes [20]

1.3.3 Adsorption

Adsorption is a heterogeneous process that can be used to capture CO_2 from flue gases generated by fossil fuel power plants. It can be performed on naturally occurring substances such as coal or some more complex human-made sorbents such as activated carbon, molecular sieves and zeolites. Two methods that are commonly used for adsorption are pressure swing adsorption (PSA) and temperature swing adsorption (TSA). The driving force for either case is temperature, CO_2 partial pressures, surface forces and pore size or sorbent available surface area. PSA is always preferred since it requires lower energy and has higher regeneration rate.

Figure 1.8 shows an example of a single chamber adsorption system. Flue gases are cool down to the desirable temperature first and then enter the adsorption chamber. To get the maximum CO_2 adsorption, the chamber is pressurized by flue gas with compressors. The rest of the flue gas component are allowed to exit. To liberate the CO_2

from the sorbent, a vacuum can should be applied. Then, carbon oxide can be sent by a separate outlet for sequestration.

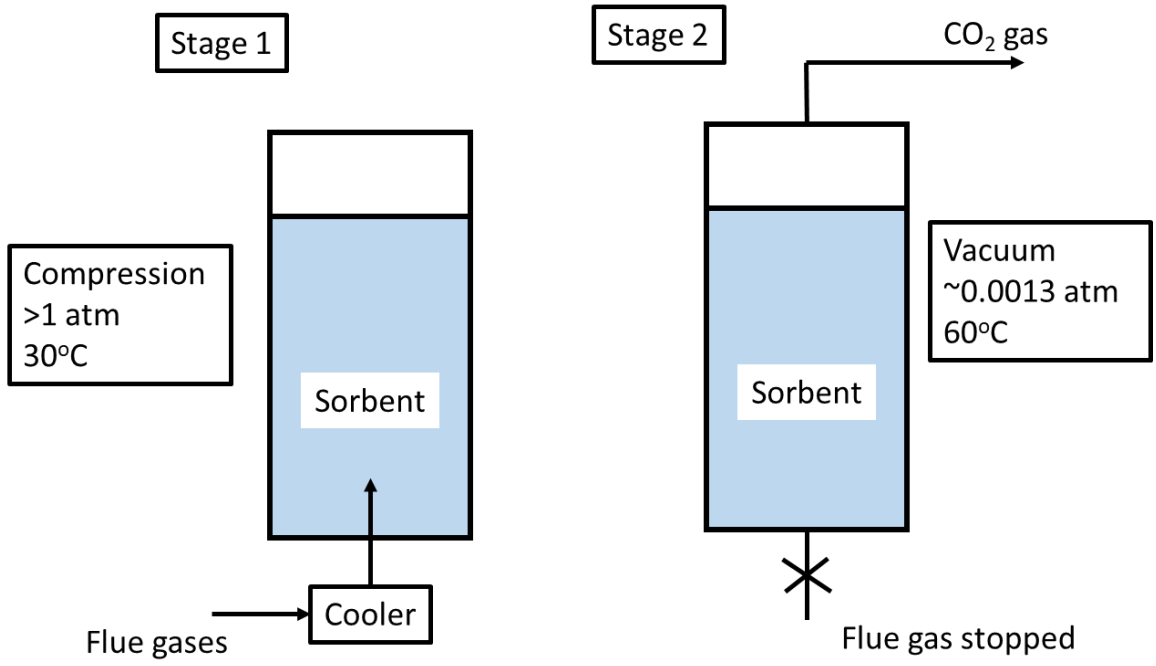

Figure 1.8 Single chamber adsorption system [22]

Figure 1.9 shows an example of typical pressure swing adsorber. In this adsorber, two chambers pass the pressure back and forth in a continuous cycle. Pressure is applied to one of the chambers and flue gases are sent into this chamber. Then the pressure is transferred to the other chamber and introduce a new volume of waste gas. When this chamber is pressurized, the first chamber is depressurized then CO_2 is collected. The waste gases are sequentially injected into the two chambers and the cycle continues in a switching mode. The flow of the CO_2 and the flow of the rest of the flue gases are controlled by the connecting lines and valves[10].

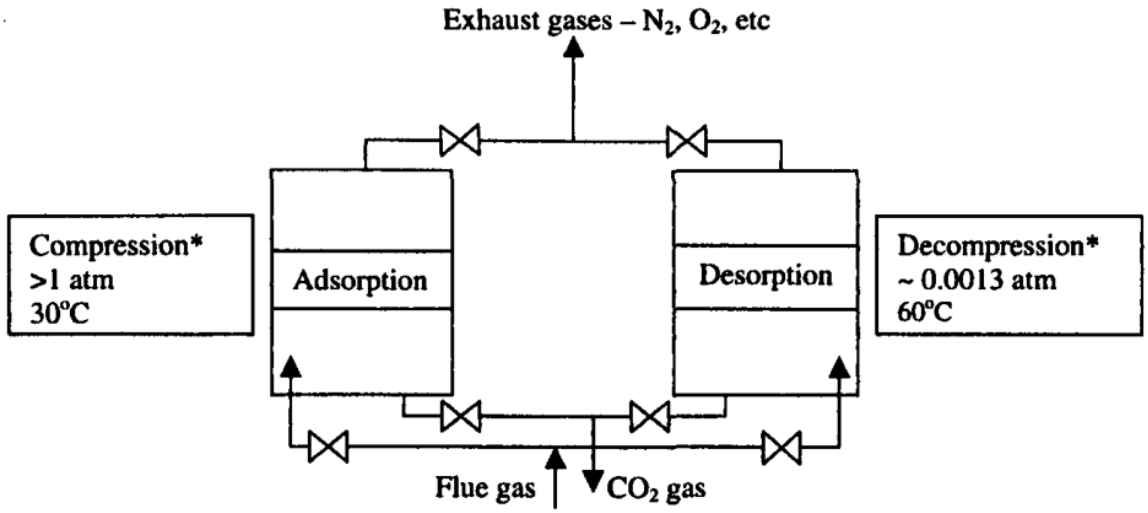

Figure 1.9 Two-chamber pressure adsorption system [10]

1.4 METHANE CONVERT PROCESS

Nowadays, with the development of the natural gas industry, the production of natural gas is increasing day by day, the potential and availability of this non-renewable energy have been widely concerned. Methane, the main component of natural gas, not only can work as fuel to produce heat and electricity but also can be converted to syngas and other valuable chemicals.

1.4.1 Oxidative coupling of methane

Oxidative coupling of methane (OCM) is a process that converts natural gas into value-added chemicals such as ethane and ethylene, it has been investigated as a promising way to obtain higher hydrocarbons from natural gas. The first attempt of directly converting methane into ethylene and other hydrocarbons was done by Ito and Lunsford[23], Keller and Bhasin[24] during the 1980s. Those studies reported that methane could be converted to ethylene and other hydrocarbons like ethane successfully but with a low conversion rate and poor yields over metal oxide catalysts. Many studies

since then targeted at effects of catalyst compositions, modifications, and reaction conditions toward achieving high conversion and selectivity. There have been many efforts to improve the C2 yield by developing novel catalysts, such as Li/MgO[25], La_2O_3/CaO[26], and Mn/Na_2WO_4/SiO_2[27]. The kinetics of OCM on La_2O_3/CaO catalyst involves 8 species. The kinetic model of a set of 10-step OCM reactions was reported by Stansch et al[26]. The kinetic model included thermal cracking, steam reforming, and water gas shift reactions. The kinetic model considered the following set of stoichiometric equations:

$$CH_4 + 2O_2 \rightarrow CO_2 + 2H_2O \quad (1\text{-}1)$$

$$2CH_4 + 0.5O_2 \rightarrow C_2H_6 + H_2O \quad (1\text{-}2)$$

$$CH_4 + O_2 \rightarrow CO + H_2O + H_2 \quad (1\text{-}3)$$

$$CO + 0.5O_2 \rightarrow CO_2 \quad (1\text{-}4)$$

$$C_2H_6 + 0.5O_2 \rightarrow C_2H_4 + H_2O \quad (1\text{-}5)$$

$$C_2H_4 + 2O_2 \rightarrow 2CO + 2H_2O \quad (1\text{-}6)$$

$$C_2H_6 \rightarrow C_2H_4 + H_2 \quad (1\text{-}7)$$

$$C_2H_4 + 2H_2O \rightarrow 2CO + 4H_2 \quad (1\text{-}8)$$

$$CO + H_2O \rightarrow CO_2 + H_2 \quad (1\text{-}9)$$

$$CO_2 + H_2 \rightarrow CO + H_2O \quad (1\text{-}10)$$

Typically, the OCM reactions involves methyl radicals (CH_3*) formation via hydrogen abstraction from the methane by the active surface oxygen species available on the oxide catalyst surface. The simplified reaction network of the oxidative coupling of methane at oxides is shown in Figure 1.10.

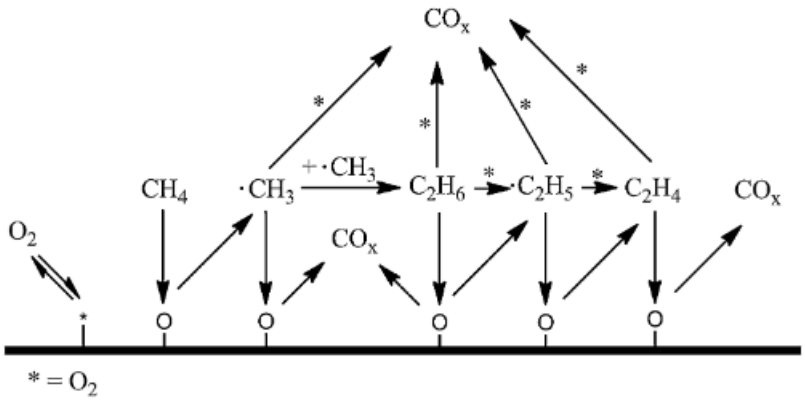

Figure 1.10 Simplified reaction network of the oxidative coupling of methane at oxides[28]

In 1982, Union Carbide first proposed the reaction on MnO_x/Al_2O_3 catalyst at 800^{o}C. It can achieve 14% methane conversion and 5% C2 selectivity, thus a new way of direct conversion and utilization of methane could be opening. Narui et al. carried out the reaction on PdO/Al_2O_3 (PdO load 36%) catalyst at 740^{o}C, and the selectivity of C2 was 7.17% at 11% methane conversion[29]. Studies on Li/MgO catalytic system show that on pure MgO, only 1% C2 yield was obtained at 720^{o}C. The yield of C2 was 14% on 7% Li/MgO catalyst. It is believed that the substitution of Li^+ to Mg^{2+} in MgO leads to the formation of a new active site, which promotes the reaction[30]. Warren et al found that introducing Cl^- into the system not only promote the reaction well but also inhibit the generation of CO_2 and improve the ratio of C_2H_4/C_2H_6 [31]. After screening hundreds of catalysts by more than 40 labs worldwide, most of the alkali, alkaline earth, transition, and rare earth metals are used in the OCM process.

At present, the catalysts with good performance are SrO/La_2O_3 and $Mn/Na_2WO_4/SiO_2$. In 1998, Lunsford et al. obtained a 20% methane conversion rate and 80% C2 selectivity in $Mn/Na_2WO_4/SiO_2$ system. [32] A comparative study of $Mn/Na_2WO_4/SiO_2$ system with fixed bed reactor and electrochemical oxygen supply

reactor shows that electrochemical oxygen supply can improve the selectivity of reaction and the yield of C2 hydrocarbons, and 86% C2 selectivity and 4% C2 yield could be reached under certain reaction conditions[33]. In general, decreasing CH_4/O_2 ratio can improve methane conversion, but the reaction's selectivity could also be decreased.[34] To improve the C2 selectivity, it is necessary to separate the dilute ethylene to recycle the methane, which inevitably increases the cost of separation. To improve the economic viability of the process, many strategies are used in the OCM reactions, for example, membrane reaction separation systems, electrocatalytic reaction separation systems, and distributed oxygen feed with different reactor design.

1.4.2 Dry methane reforming

Dry methane reforming (DMR) is the process that utilizes two leading greenhouse gases, carbon dioxide (CO_2) and methane (CH_4), to produce a mixture of carbon monoxide (CO) and hydrogen (H_2) syngas, which is a critical precursor to produce other valuable chemicals and liquid fuels. The concept of dry methane reforming was proposed as early as 1888.[35] In addition to its potential role in managing greenhouse gas, dry methane reforming also attract attention as a response to repeated oil crisis owing to its higher CO selectivity and low H_2/CO ratio, which are suitable for the synthesis of long chain hydrocarbons or oxygenate chemicals such as acetic acid, dimenthyl ether and oxo-alcohols[36]. A variety of catalysts for dry methane reforming including noble and non-noble metals have been studied. Noble metals represented by Ir, Pt, Pd, etc. has a higher resistance to the coke formation but they are economically unavailable[37]. To reduce the cost of catalyst, cheaper metals such as Ni, Co were used as a promoter to decorate the noble metal and help to provide the additional active sites and improve their resistance to

coke formation[38]. Some studies also focus on the support influence as well as the methods of preparation and activation to enhance the catalytic performance[39].

In the thermodynamics perspective, dry methane reforming is an extremely endothermic reaction.

$$CH_4 + H_2O \rightarrow CO + 3H_2, \Delta H^0_{298K} = 206kJ \cdot mol^{-1} \quad (1\text{-}11)$$

Both CH_4 and CO_2 have very strong and stable chemical bonds with high dissociation energy: 435 kJ/mol for (CH_3-H) and 526 kJ/mol for (CO-O). To make the reaction occur and produce syngas, high temperature is required. For the long-term utilization, renewable energy would have to be used to supply the required heat for the dry methane reforming reaction. The equilibrium for the production of synthesis gas is generally influenced by the reverse water gas shift reaction:

$$CO_2 + H_2 \rightarrow CO + H_2O, \Delta H^0_{298K} = 41kJ \cdot mol^{-1} \quad (1\text{-}12)$$

This results in the product H_2/CO ratio below 1 and the conversion rate of CO_2 is higher than CH_4.

For both OCM and DMR reactions, carbon deposition is a non-negligible problem that can lead to catalyst deactivation. For DMR, the carbon is primarily formed via three reactions:CH_4 decomposition, Boudouard reaction, reduction of carbon monoxide by hydrogen produced by previous reactions.

$$CH_4 \rightarrow C + 2H_2, \Delta H^0_{298K} = 75kJ \cdot mol^{-1} \quad (1\text{-}13)$$

$$2CO \rightarrow C + CO_2, \Delta H^0_{298K} = -172kJ \cdot mol^{-1} \quad (1\text{-}14)$$

$$CO + H_2 \rightarrow C + H_2O, \Delta H^0_{298K} = -131kJ \cdot mol^{-1} \quad (1\text{-}15)$$

The fashion of carbon deposition on the catalyst surface is shown in Figure 1.11.

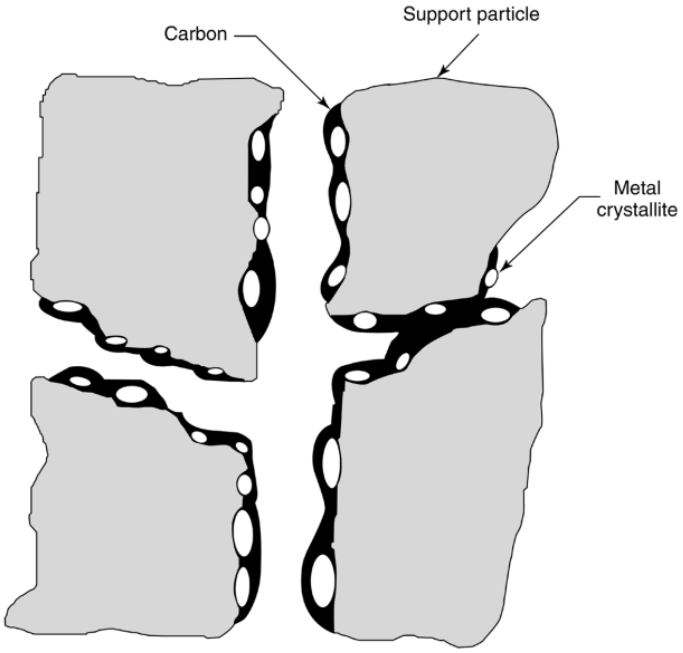

Figure 1.11 Pore plugging in a supported metal catalyst owing to carbon deposition[40]

Wang et al. found that carbon formed by CH_4 decomposition when temperature is higher than 557^oC and formed by the Boudouard reaction below 700^oC. They suggested that at the feed ratio of CO_2/CH_4=1:1, the optimum temperature range is 870-1040^oC when taking the conversion and carbon formation into consideration [41]. Several other studies focused on the effect of temperature, CO_2/CH_4 ratios, pressures also concluded that to obtain higher conversion rate of DMR reactions, the temperature above 850^oC and low pressures is required[42-44].

Carbon formed at different temperature and support present different shapes and has different impact on the catalyst. Arona et al listed different types of carbon species deposited during dry methane reforming process, as shown in Table 1.2[45]

Table 1.2 Details of different carbon species formed on the catalyst surface

Carbon structure	Designation	Temperature range (°C)
Adsorbed, atomic carbon (surface carbide)	C_α	200-400
Polymers, amorphous films	C_β	250-500
Ni carbide (bulk)	C_γ	150-250
Vermicular filaments or whiskers	C_v	300-1000
Graphite (crystalline) platelet films	C_c	500-550

1.5 METHANE CONVERT REACTOR DESIGN

1.5.1 Fixed-bed reactor

Since the OCM reaction was proposed and concerned, most research works on OCM are based on the fixed-bed reactors since the fixed-bed reactors have simple structure and it is easy to assemble and operate. The scheme of fixed-bed reactor for OCM reaction is shown in Figure 1.12. In the fixed-bed reactors, all gas composition is co-fed at the inlet of the reactor. The catalyst is filled inside the reactor. The fixed-bed reactor is an ideal candidate for industrial production because of its simple structure. However, due to the key challenge of heat management and temperature control problem, the C2 products (ethylene and ethane) yields cannot achieve over 25%, which limits the application in industry. Apparently, the high axial and radial temperature gradients

occurring in fixed-bed reactors not only limit conversions but also cause a drop of C2 selectivity and yield. Moreover, the effect of oxygen concentration can also make the C2 products oxidized into undesirable products such as carbon dioxide and carbon monoxide since the oxygen distribution cannot be controlled in the fixed-bed reactor.

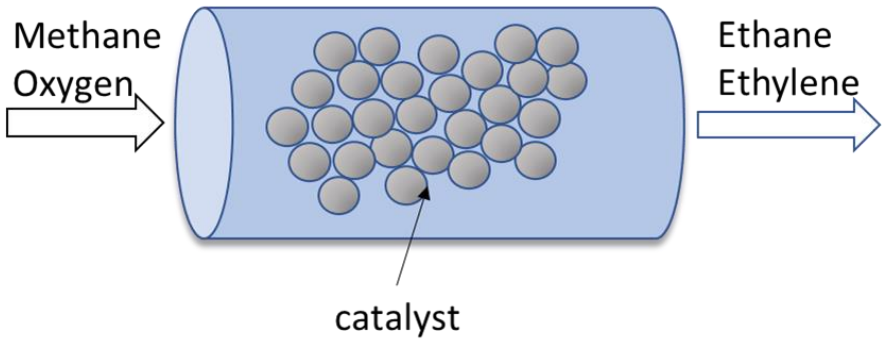

Figure 1.12 Schematic of fixed-bed reactors[46]

1.5.2 Membrane reactor

To overcome the limitation of low C2 yield and minimizing the economic constraints, the OCM studies have also been focused on the application of the membrane reactors. In contrast to the fixed-bed reactor, the components of the membrane reactor enter the reactor along the selective permeation membrane. By controlling the driving force such as partial pressure, the distribution of components in the reactor can be well controlled, so that the reaction can be carried out fully, and the problem of excessive oxidation of products can be avoided. Many different types of inorganic membranes including inert porous membranes, packed bed membranes, catalytic membranes, solid-oxide membranes, and dense membranes are reported in literatures. Schematic of catalytic mixed conducting ceramic membrane reactors for various reactions are shown in Figure 1.13[47].

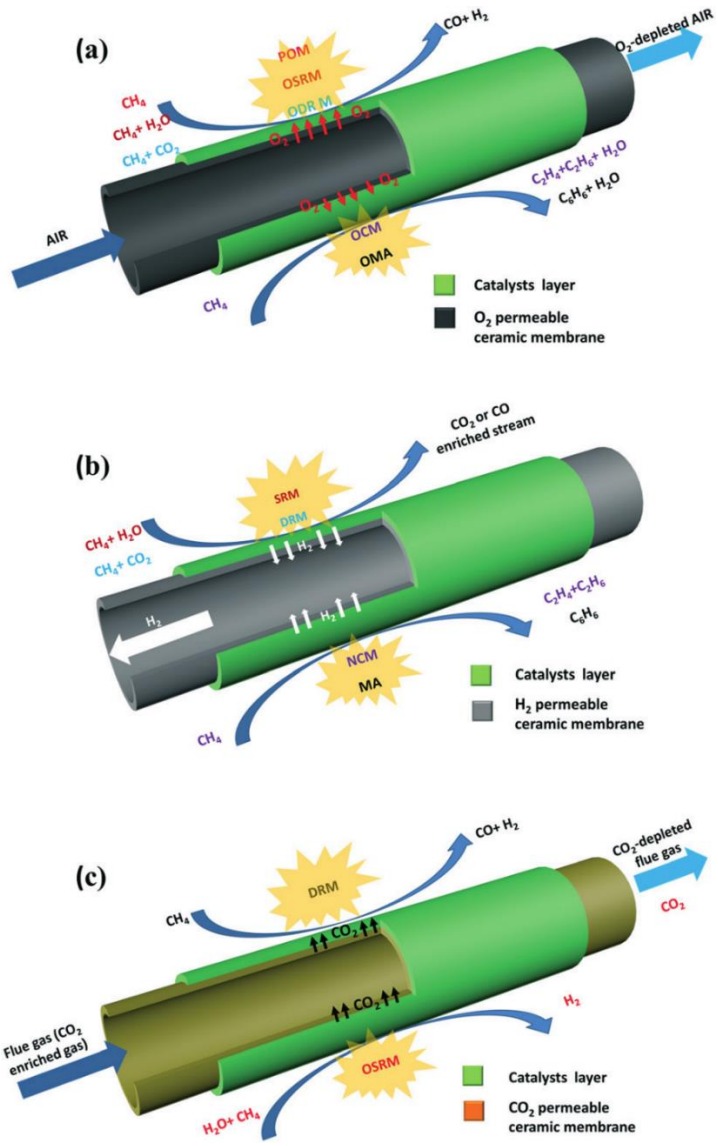

Figure 1.13 Schematic of catalytic mixed conducting ceramic membrane reactors for various reactions[47]

The most appropriate candidate materials for membrane reactor found so far are the perovskite oxides. The performance of membrane reactors can be improved by (1) developing new membrane materials which can be stable at high temperature under reducing atmosphere during a long-term operation with less loss of gas permeability; (2) membrane materials surface modifications to work as a catalyst or improve the gas permeation; (3) designing new membrane reactor configurations[48-54]. Some studies

have obtained remarkable results in the surface modification of the membrane. The partial oxidation of methane performance in membrane reactor was studied by Yaremchenko et al. They found that the methane conversion rate rose from 5.2% at 850^{o}C to 16.1% at 950^{o}C. In this case, the perovskite oxide $(SrFe)_{0.7}(SrAl_2)_{0.3}O_2$ itself served as a catalyst[55]. An increased oxygen flux and methane conversion due to the Pt coating on $La_{0.6}Sr_{0.4}Co_{0.2}Fe_{0.8}O_{3-\delta}$ hollow fiber membrane was reported by Tan et al. At 950^{o}C, a maximum C2 yield of 15.3% and 43.8% selectivity was obtained[56]. By comparing the performance of modified $Ba_{0.5}Sr_{0.5}Co_{0.8}Fe_{0.2}O_{3-\delta}$ disk membrane surface with three different catalysts (Pt/MgO, Sr/La_2O_3, LaSr/CaO) for OCM, it was found that LaSr/CaO reached the highest yield between 900and 1000^{o}C and achieved 18% C2 yield with 34% CH_4 concentration[57]. Some other studies also focused on developing the configuration of membrane reactor, a two-stage membrane reactor was proposed by Chen et al. The schematic diagram of the two-stage membrane reactor is shown in Fig 1.14. In this case, methane travels through the membrane consisting of $Ba_{0.5}Sr_{0.5}Co_{0.8}Fe_{0.2}O_{3-\delta}$ (97.5 mol%) and Co_3O_4 (2.5 mol%) first, where the deep oxidation occurs. The heat released by the deep oxidation is supplied to the catalyst bed where endothermic reforming reactions take place. This device was considered as conducive to the energy consumption and achieved both the methane conversion and CO selectivity exceed 95%. [58]

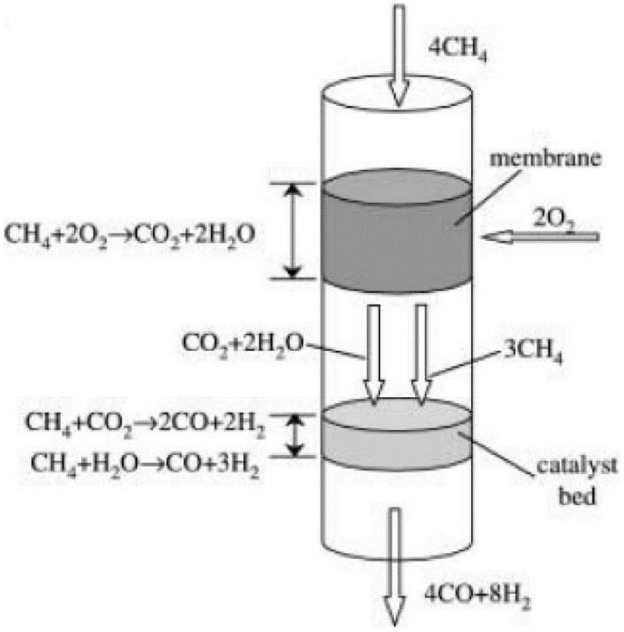

Figure 1.14 Schematic diagram of two-stage membrane reactor for syngas production[59]

In conclusion, the problem of greenhouse effect and energy crisis cannot be ignored. The development of carbon capture and conversion technology is crucial to the development of environment.

CHAPTER 2

FUNDAMENTAL OF HIGH TEMPERATURE MULTIPHASE CO_2 CAPTURE AND CONVERSION MEMBRANES AND REACTORS

2.1 WORKING PRINCIPLE OF HIGH-TEMPERATURE CO_2 CAPTURE AND CONVERSION MEMBRANES

2.1.1 Working principle of classical high-temperature CO_2 capture and conversion membranes

The previously reported high-temperature dual-phase membranes for CO_2 separation can be classified into 4 different types, which are mixed oxygen-vacancy and carbonate-ion conducting (MOCC), mixed electron and carbonate-ion conducting (MECC), mixed oxygen vacancy, and electron-hole conducting/molten carbonate double phase membrane (MOECC), mixed oxygen vacancy and electron-hole conducting/metal/molten carbonate triple-phase membrane (MOEECC).

In MOCC membranes, the most commonly used materials in the solid oxide phase are SDC and YSZ, which are known as typical oxide-ion conductors. In MOCC membranes, gaseous CO_2 reactors with oxygen anions form carbonate ions (2-1), then the carbonate ions travel through the molten carbonate phase and release CO_2 at the permeated side following the reverse reaction. The working principle of the MOCC membranes can be illustrated in Figure 2.1.

$$CO_2 + O^{2-} = CO_3^{2-} \quad (2\text{-}1)$$

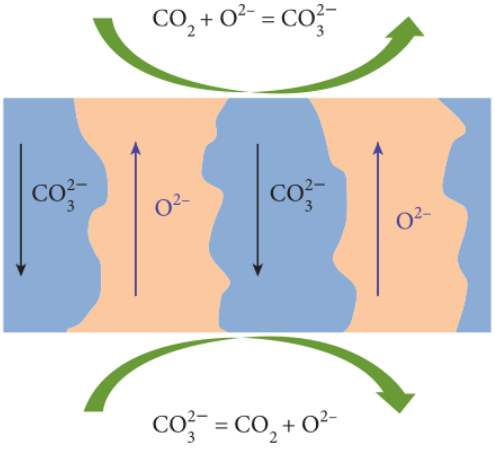

Figure 2.1 Transport principle of MOCC membranes[20]

In MECC membranes, the ideal candidate for the metal phase should have relatively high electrical conductivity and chemical inertness to molten carbonate. In MECC membranes, CO_2 reacts with oxygen molecular in the presence of electrons on electron-conducting porous support following reaction at the feed side (2-2), then the carbonate ion transport through the membrane via molten carbonate phase and the reverse reaction (2-3) occurs at the permeate side. The working principle can be illustrated in Fig 2.2.

$$CO_2 + 1/2\, O_2 + 2e^- = CO_3^{2-} \quad (2\text{-}2)$$

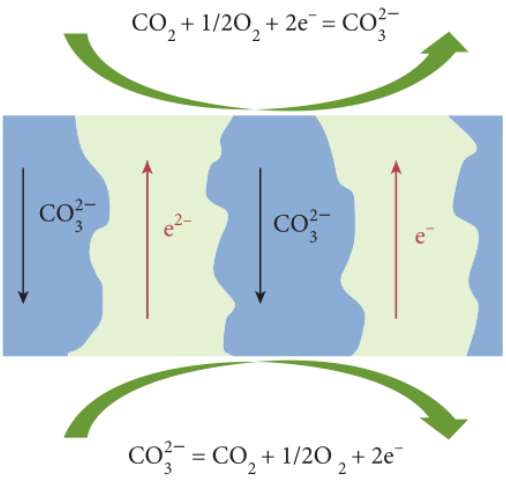

Figure 2.2 Transport principle of MECC membranes[20]

In MOECC membranes, a mixed oxygen-vacancy and electron-conducting (MOEC) solid oxide phase is mixed with molten carbonate to form the membrane. Both MOCC and MECC transport mechanisms take place in MOECC. At the feed side, oxygen ions are formed by gaseous oxygen with the presence of electrons. Carbon dioxide reacts with oxygen in the presence of electron to form carbonate ion (2-3, 2-5). In parallel, carbon dioxide reacts with oxygen ions, forming carbonate-ion (2-4). The carbonate ion then transports through the membrane and form carbon dioxide and oxygen by reverse reactions.

$$CO_2 + 1/2\,O_2 + 2e^- = CO_3^{2-} \quad (2\text{-}3)$$

$$CO_2 + O^{2-} = CO_3^{2-} \quad (2\text{-}4)$$

$$1/2\,O_2 + 2e^- = O^{2-} \quad (2\text{-}5)$$

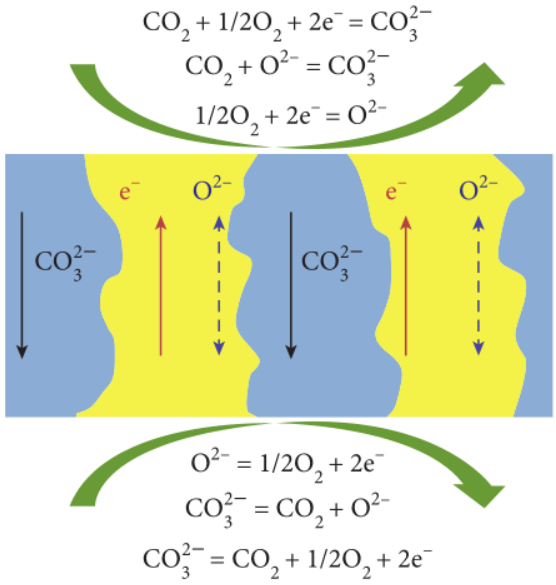

Figure 2.3 Transport principle of MOECC membranes[20]

2.2 NEWLY DEVELOPED CO_2/O_2 CO-TRANSPORT MEMBRANES WITH ENHANCED ELECTRON CONDUCTION

The current reported CO_2/O_2 co-transport membranes have a performance-limiting factor that the multi-phase boundary density for the O_2-transport pathway is very low, which results in a low O_2 to CO_2 flux ratio. To increase the O_2 to CO_2 flux ratio, one strategy is to expand the O_2-transport pathway. The approach to achieve this aim is to introduce electronic conduction into the CeO_2 phase, which makes the multi-phase boundary active for the pure CO_2-transport also active for O_2-transport. The schematic and working principle of the membrane with the addition of the electronic conduction pathway is shown as Figure 2.4.

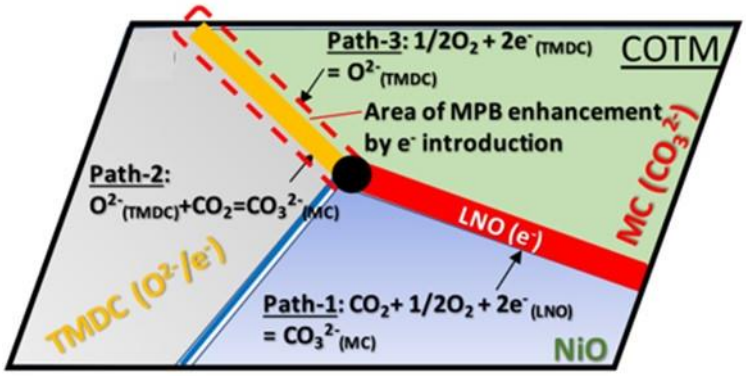

Figure 2.4 Schematic working principle of the newly developed CO_2/O_2 co-transport membrane

The newly developed CO_2/O_2 co-transport membranes are triple phase membranes, consisting of a porous matrix solid oxide phase made of transition metal doped CeO_2 (TMDC), eutectic Li_2CO_3-Na_2CO_3 molten carbonate phase (MC), and $LiNiO_2$ (LNO)formed in-situ between MC and NiO at high temperatures. Here the TMDC works as a mixed electron and oxygen ion conductor, molten carbonate is a pure carbonate ion conductor, LNO is a pure electron conductor.

The transport mechanism of the new electron enhanced COTM is shown in Figure 2.5.

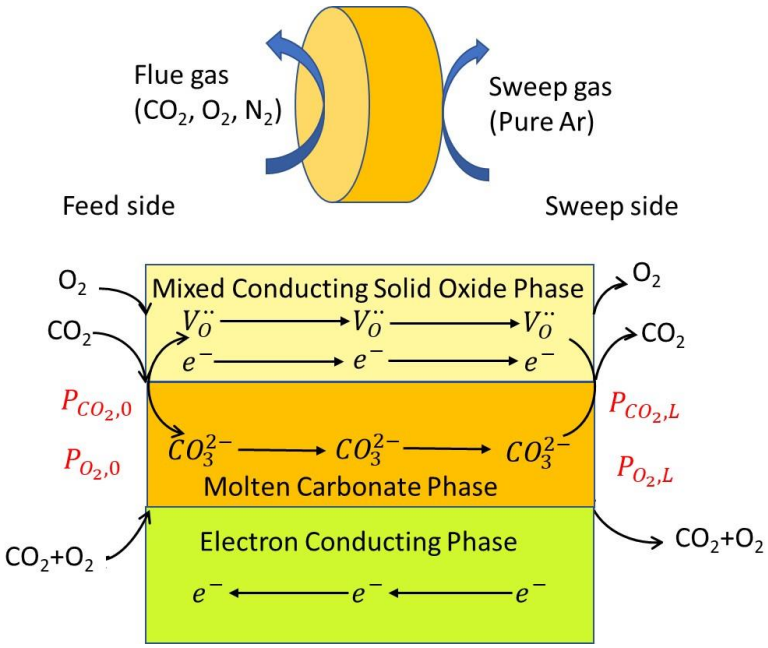

Figure 2.5 Transport mechanism of high temperature CO_2/O_2 co-transport membrane

For CO_2 transport, the difference in partial pressures of CO_2 at the feed and permeate boundaries creates a concentration gradient of carbonate ions in MC phase. At the feed side of the membrane, gaseous CO_2 reacts with oxygen ions(O^{2-}) to form carbonate ions.

$$O^{2-}{}_{(SO)} + CO_2 = {CO_3}^{2-}{}_{(MC)} \tag{2-6}$$

Also, with the electron-conducting phase, there is another reaction taking place. CO_2 and O_2 are combined with electron to form carbonate ions.

$$CO_2 + \frac{1}{2}O_2 + 2e^-{}_{(LNO)} = {CO_3}^{2-}{}_{(MC)} \tag{2-7}$$

$$\frac{1}{2}O_2 + 2e^-{}_{(LNO)} = O^{2-}{}_{(SO)} \tag{2-8}$$

Carbonate ions transport through the MC phase from feed side to permeate side with the driving force of pressure gradient. When carbonate ions and oxygen ions arrive at permeated side, CO_2 and O_2 are reformed by reverse reaction. The driving forces of the

transport are the partial pressure and gradient of CO_2 and O_2 across the membrane. The overall reaction can be described by:

$$\frac{1}{2}O_2(feed) + CO_2(feed) = \frac{1}{2}O_2(sweep) + CO_2(sweep) \quad (2\text{-}9)$$

2.3 THEORETICAL TRANSPORT FLUX MODEL FOR CO_2 SEPARATION MEMBRANES

2.3.1 Transport flux for MOCC membranes

A model to describe the flux of CO_2 through a dual-phase membrane consisting of solid oxide and molten carbonate phases was developed by Wade et al.[60]. For the transport thermodynamics of the molten carbonate phase, a multi-component force balance is used to describe the properties:

$$C_i\nabla(\mu_i + \mathrm{Zfi}\emptyset) = RT\sum_j \frac{C_iC_j}{C_TD_{ij}}(V_j - V_i) \quad (2\text{-}10)$$

Where C_i is the concentration of species i and it is also the driving force of the transport system balanced by the interactions with other species j in the system.

The flux of species i, J_i, is defined as:

$$J_i = C_iV_i \quad (2\text{-}11)$$

Rearrange (2-10)

$$C_i\nabla(\mu_i + ZFi\emptyset) = \frac{RT}{C_T}\sum_j \frac{1}{D_{ij}}(C_iJ_j - C_jJ_i) \quad (2\text{-}12)$$

Where C_T is the total concentration of all species and $C_T=3C_C$,

Under steady state conditions, the individual flux of each alkali metal cations in the molten carbonate phase J_M=0, the concentration of the carbonate ion is uniform, so the chemical potential of CO_3^{2-} can be assumed as a constant, which means $\nabla\mu_C = 0$

Eventually, the following expression for carbonate flux can be obtained:

$$J_C = -\varepsilon \frac{Z_C C_C D_{CM} F}{RT} \nabla \emptyset^{MC} \tag{2-13}$$

$$D_{CM} = 3\left(\frac{x_{Li}}{D_{CLi}} + \frac{x_{Na}}{D_{CNa}} + \frac{x_K}{D_{CK}}\right)^{-1} \tag{2-14}$$

For the solid oxide phase, it can be either a pure ionic conductor or a mixed ionic-electronic conductor. The motion of the mobile charge carriers in a solid oxide vacancies and electrons can be obtained by dilute solution model:

$$J_i = -(1-\varepsilon)\left(D_i \nabla C_i + \frac{Z_i F D_i C_i}{RT} \nabla \emptyset^{SO}\right) \tag{2-15}$$

Where the (1-ε) is the correct factor for the fractional volume of the solid oxide phase.

The reaction occurred on the surface of solid oxide phase and molten carbonate phase converting CO_2 to CO_3^{2-} and coupling the transport properties of the solid oxide phase and molten carbonate phase.

$$CO_{2(g)} + O^X_{O(SO)} = CO^{2-}_{3(MC)} + V^{\cdot\cdot}_{O(SO)} \tag{2-16}$$

The flux of all the species in the membrane must be known to solve for the flux of carbon dioxide. The concentration and electrical potential profiles are determined by solving the partial differential equation. To solve the partial differential equation, the reaction on the surface is assumed to be at a pseudo-steady state:

$$\mu_{CO_2} + \mu_{O_O^x} = \mu_V + Z_V F \emptyset_{SO} + \mu_C + Z_C F \emptyset_{MC} \quad (2\text{-}17)$$

The chemical potential of CO_2 is related to the CO_2 partial pressure:

$$\mu_{CO_2} = \mu^o_{CO_2} + RT \ln \frac{P_{CO_2}}{P^o} \quad (2\text{-}18)$$

The chemical potential of defect charge carriers in the solid oxide phase, vacancies and electrons are related to their concentrations:

$$\mu_i = \mu_i^o + RT \ln \frac{C_i}{C^o} \quad (2\text{-}19)$$

Then the following equations can be obtained:

$$RT \left(\ln \frac{P_{CO_2}}{P^o} \frac{C^o}{C_v} \right) - F(Z_v \emptyset_{SO} + Z_C \emptyset_{MC}) = \beta \quad (2\text{-}20)$$

$$\beta = \mu_v^o - \mu^o_{CO_2} + \mu_c - \mu_{O_o^x} \quad (2\text{-}21)$$

Where β is considered as a constant over the bulk of the material.

The boundary conditions of the partial differential equations are the requirement of net zero current and the zero potential along the coupled CO_2 surface reaction at both boundaries[61].

2.3.2 Transport flux for MECC membranes

If the metal-carbonate membrane is a homogenous mixed conductor, the partial flux density J_i of the charged particle can be written as:

$$J_i = -\frac{D_i C_i}{RT} \nabla \eta_i = -\frac{\sigma_i}{(z_i F)^2} \nabla \eta_i = -\frac{\sigma_i}{(z_i F)^2} (\nabla \mu_i + z_i F \nabla \emptyset) \quad (2\text{-}22)$$

Where D_i is the self-diffusivity, C_i is the concentration, σ_i is the conductivity and z_i is the charge of species i, η_i is the electrochemical potentials of species i, μ_i is the

chemical potentials of species i, Φ is the static potential. In this case, the charged particle i can be CO_3^{2-} or e^-.

If we consider CO_3^{2-} as species 1, e^- as species 2, since there is no external current exists in the membrane,

$$z_1 J_1 + z_2 J_2 = 0 \tag{2-23}$$

The Equation (2-23) can be simplified as:

$$J_1 = -\frac{\sigma_1 \sigma_2}{z_1^2 F^2}\left(\frac{\nabla \mu_1 - z_1/z_2 \, \nabla \mu_2}{\sigma_1 + \sigma_2}\right) \tag{2-24}$$

At the feed-surface, the CO_2 transport electrochemical reaction is:

$$CO_2 + 1/2\, O_2 + 2e^- = {CO_3}^{2-} \tag{2-25}$$

That means at equilibrium,

$$\nabla \mu_{CO_2} + \frac{1}{2}\nabla \mu_{O_2} = \nabla \mu_1 - 2\nabla \mu_2 \tag{2-26}$$

The chemical potential gradient can be expressed as:

$$\nabla \mu_{CO_2} = \nabla \mu_1 = \frac{RT}{C_1}\left(\frac{\partial \ln \alpha_1}{\partial \ln C_1}\right)\nabla C_1 \tag{2-27}$$

$$\nabla \mu_{O_2} = \nabla \mu_2 = \frac{RT}{C_2}\left(\frac{\partial \ln \alpha_2}{\partial \ln C_2}\right)\nabla C_2 \tag{2-28}$$

Concentration C_i can be calculated by ideal gas law:

$$C_1 = \frac{2}{3}\left(\frac{P_t}{RT}\right) \tag{2-29}$$

$$C_2 = \frac{1}{3}\left(\frac{P_t}{RT}\right) \tag{2-30}$$

Where

$$P_t = P_{CO_2} + P_{O_2} = P_1 + P_2 \tag{2-31}$$

$$\nabla C_1 = \frac{2}{3}\left(\frac{1}{RT}\right)\left(\frac{dP_t}{dL}\right) \tag{2-32}$$

The flux of carbonate ion can be written as:

$$J_{CO_3^{2-}} = J_{CO_2} = -\frac{3}{8F^2}\left(\frac{\sigma_{CO_3^{2-}}\sigma_{e^-}}{\sigma_{CO_3^{2-}} + \sigma_{e^-}}\right)\left(\nabla \ln P_{CO_2} + \frac{1}{2}\nabla \ln P_{O_2}\right) \tag{2-33}$$

At steady-state, the flux density of CO_2 can be obtained by integrating for one-dimensional system for L and P:

$$J_{CO_2} = -\frac{3}{8F^2L}\int_{P'_{CO_2}P'_{O_2}}^{P''_{CO_2}P''_{O_2}}\left(\frac{\sigma_{CO_3^{2-}}\sigma_{e^-}}{\sigma_{CO_3^{2-}} + \sigma_{e^-}}\right)\left(d\ln P_{CO_2} + \frac{1}{2}d\ln P_{CO_2}\right) \tag{2-34}$$

Where P''_{CO_2} and P''_{O_2} represent the CO_2 and O_2 partial pressure at the permeate side, while P'_{CO_2} and P'_{O_2} represent the CO_2 and O_2 partial pressure at the feed side. Since the conductivity of metal phase is much larger than the molten carbonate phase, Equation (2-35) can be simplified into:

$$J_{CO_2} = -\frac{3}{8F^2L}\int_{P'_{CO_2}P'_{O_2}}^{P''_{CO_2}P''_{O_2}}\sigma_{CO_3^{2-}}\left(d\ln P_{CO_2} + \frac{1}{2}d\ln P_{CO_2}\right) \tag{2-35}$$

If the microstructural and volumetric effects are taken into consideration, Jco_2 can be changed to:

$$J_{CO_2} = -\frac{\varepsilon}{\tau}\frac{3}{8F^2L}\varphi\int_{P'_{CO_2}P'_{O_2}}^{P''_{CO_2}P''_{O_2}}\sigma_{CO_3^{2-}}\left(d\ln P_{CO_2} + \frac{1}{2}d\ln P_{CO_2}\right) \tag{2-36}$$

Where ε is the porosity of the porous metal matrix, τ is the tortuosity of the porous matrix, and φ is the volumetric fraction of the carbonate phase[62, 63].

2.3.3 Transport flux for MOEC membranes

The solid oxide phase in the MOCC membrane is a pure oxygen ion conductor, while in MOEC the solid oxide phase is a mixed electron and oxygen ion conductor. Considering the electron conducting in the solid oxide phase, the flux of electron is connected to the flux of oxygen by:

$$J_n = -4J_{O_2} \tag{2-37}$$

To establish the concentration of electrons and oxygen vacancies at both boundaries, the mass action law should be used:

$$C_n = K(T)^{1/2} C_v^{-1/2} P_{O_2}^{-1/4} \tag{2-38}$$

In this model, the electron current and electron concentration are both driven by the oxygen partial pressure. The oxygen inside the bulk of the lattice is assumed to be very small. The gas phase diffusive flux of oxygen relative to the membrane surface at the feed side can be approximated as:

$$J_{O_2} = -\frac{D_{O_2,CO_2}}{\delta_{conc}} (C_S(0) - C_S^{Feed}) \tag{2-39}$$

Where $D_{O2,CO2}$ is the binary gas phase diffusion coefficient, δ_{conc} is an assumed concentration boundary layer thickness, C_S (0) is the oxygen concentration at the membrane surface, C_S^{Feed} is the oxygen concentration within the bulk of the feed system.

The vacancy and electron concentrations can be coupled by electroneutrality:

$$\sum Z_i C_i = Z_V C_V + Z_n C_n + Z_D C_D = 0 \tag{2-40}$$

If we assume C_v as a constant and using oxygen partial pressure to approximate the value,

$$\frac{d\emptyset^{SO}}{dx} = \frac{1}{Z_V}\left(\frac{\varepsilon Z_C D_C C_C}{(1-\varepsilon)Z_V D_V C_V - \varepsilon Z_C D_C C_C}\right)\ln\left(\frac{P_{CO_2}(0)}{P_{CO_2}(L)}\right) \tag{2-41}$$

At the permeate surface,

$$\nabla \cdot J_n = \frac{d^2 C_n}{dx^2} + \omega \frac{dC_n}{dx} = 0 \tag{2-42}$$

$$\omega = \frac{nZF}{RT}\frac{d\emptyset^{SO}}{dx} \tag{2-43}$$

Solving for concentration of electron, at x=0 and x=L boundaries[60],

$$C_n(x) = 2K(T)^{\frac{1}{3}} P_{O_2}^{-\frac{1}{6}}(x) \tag{2-45}$$

The final CO_2 flux density for the MOEC membranes is:

$$J_{CO_2} = -\frac{\varepsilon/\tau_{MC}\, C_C D_C \left(\frac{1}{2}\sigma_n \nabla\mu_{O_2} + (\sigma_V + \sigma_n)\nabla\mu_{CO_2}\right)}{\left(RT(\sigma_V + \sigma_n) + \frac{\varepsilon/\tau_{MC}}{(1-\varepsilon)/\tau_{SO}} 2Z_n Z_C F^2 D_C C_C\right)} \tag{2-46}$$

CHAPTER 3

SYNTHESIS AND CHARACTERIZATION OF HIGH-TEMPERATURE CO_2 TRANSPORT MEMBRANES

3.1 SYNTHESIS OF POROUS MATRIX AND MEMBRANES

Porous ceramics, also known as microporous ceramics, foam ceramics, is a type of functional ceramic material. The primary materials are corundum sand, silicon carbide, and other inorganics, and formed through high-temperature sintering process. After formation, porous ceramic materials contain open aperture, high porosity and tortuosity. Porous ceramics can be generally divided into three categories according to pore size: microporous ceramics (pore size less than 2 nm), mesoporous ceramics (pore size of 2-50 nm), and Microporous ceramics (pore size more than 50 nm). The pore structure and preparation method can be divided into honeycomb ceramics and foam ceramics. The latter has three basic types: closed, open, and half-open structures. Porous ceramics have strong chemical stability, low density, high heat resistance, large specific surface area, and strong resistance to thermal impact[64].

Porous ceramics development began in the 1870s, was only used as a bacterial filter material in the early time, It has low density, low thermal conductivity, high porosity, high strength, good corrosion resistance and good thermal shock resistance. Its excellent performance has opened up a broad prospect for its application. It has been widely used in many engineering fields such as environmental protection, energy-saving,

chemical industry, petroleum, refining, food, biomedicine, etc., attracting close attention of the global material science community.

The properties of porous ceramics are closely related to the composition factors and the shape, size, and distribution of pores. From the perspective of preparation, structure, and properties, the formation of pores is the crucial step in the preparation process of porous ceramics, which is also the focus of porous ceramics research.

At the same time, the distribution of pores in porous ceramic materials could reduce the thermal conductivity of the material, which makes the porous ceramic materials excellent heat reservoir and heat insulation performance. Therefore, porous ceramic materials can be used as thermal insulation. At present, porous ceramic materials are widely used in gas and liquid filtration, purification, separation, chemical catalytic carrier, sound absorption, shock absorption, thermal insulation materials, biological materials, unique wall materials, and sensor materials.

The traditional preparation method of porous ceramics features using a pore-forming agent. The process is to add a pore-forming agent in ceramic slurry and make the pore-forming agent and ceramic slurry as evenly as possible, through different methods, and then remove the pore-forming agent in the body during the high-temperature sintering process, leaving holes behind, thus obtaining porous preform. The advantage of this process lies in that the amount of pore-forming agent can be arbitrarily adjusted to control the porosity of porous ceramics to achieve the purpose such as tailoring the thermal conductivity. The preparation process of porous ceramics is simple and easy to scale up for production. However, it is difficult to disperse the pore-forming agent evenly when mixing because of the inconsistency between the ceramic ingredients and the

particle size of the pore-forming agent, which leads to the uneven distribution of the internal pores of the porous insulation material. A criticality of this process is the type, nature, and dosage of the pore-forming agent[65, 66].

Porosity is the most crucial factor affecting microstructural properties for porous ceramic materials. There are many approaches to increase the porosity of ceramics materials. Based on the relatively mature preparation methods of porous ceramics, more attention is paid to control the size and shape of pores by unique ways. The pore formation and growth model are established accordingly [67, 68].

One prospective way to increase the porosity of ceramics is to select a granular composition for initial molding[69, 70]. Any packing of fine compositions could create cavities. The closer the particle shape is to a spherical shape, the more dispersed the liquid binder is, which is more conducive to the formation of pores and can reduce the pressure required for molding and achieve the required sintering strength. This method could achieve porosity up to 40% with a uniform structure, moderate strength, and thermal resistance. An increase in porosity could be achieved by adding high porosity granules. By increasing the inner porosity or size of granules, a higher porosity could be achieved by additionally 10%-15%. The porous ceramics containing chamotte grains and various oxides could be used as filters, porous membranes for metal refining, gas purification, catalyst carriers, fuel elements, and other purposes.

Another accessible method is to introduce additives that could be removed subsequently. The one used most extensively introduces burning-out additives, which could be represented by any combustible material, including wood and wood-processing products, coals, cooking products, etc[71]. The ceramic components are mixed with the

burning-out additives and then molded by compression, plastic molding, or slip casting. The intermediate articles should be fired in an oxidizing medium until completely burning out the additives. The porosity depends on the burning-out additives' type, content, and grain size. With this method, the porosity could be achieved up to 60% - 65%[72].

The properties of porous ceramics depend on the type of initial material, porosity, and structure of articles. The characteristics of porous ceramic's structure include porosity, permeability, pore size and pore size distribution, and specific surface area, among which the most critical parameters are pore size and porosity. Pore size could vary over a wide range from a fraction of a nanometer to a few millimeters. The role of structure in porous ceramics for different destinations is not identical. Functional pore space in permeable filtering products is created only by intercommunicating channel-shaped pores. In catalyst carriers, isolated open pores can also have an active role. In heat-insulating products, all pores act as barriers to heat propagation. Porosity is also an important feature that always affects the physical properties of materials such as permeability, conductivity, diffusion coefficient. Better knowledge and control of the porous ceramic's structure is required to obtain the desired materials performance[73].

Co-precipitation method refers to adding a mineralizer (e.g. basic solution) to a solution containing two or more cations. At a sufficiently high pH, all cations are precipitated out, forming a uniform product (usually metal hydroxides). It is a common method to prepare the ultrafine powder containing one or more metal oxides. The main advantage of the co-precipitation method is that nano-sized powders with uniform chemical composition can be obtained directly solution precursors [74].

This research work used co-precipitation method to synthesize the Mn-doped CeO_2 and NiO composite powders. Mn-doped CeO_2 (MDC) is expected to exhibit mixed oxide-ion and electron conductivity and NiO is expected to react with MC to form electron conducting $LiNiO_2$. The solution precursors are $Ni(NO_3)_2 \cdot 6H_2O$(Alfa Aesar, 99%), $Mn(NO_3)_2 \cdot 6H_2O$ (Alfa Aesar, 99.5%), and $Ce(NO_3)_3 \cdot 6H_2O$(Alfa Aesar, 99.5%). The stoichiometric amounts of these precursors were first dissolved into deionized (DI) water. After that, the $(NH_4)_2CO_3$(Fisher Scientific, Altanta, 95%) solution was slowly added into the above nitrate solution. The volume ratio of NiO and SDC was controlled at 50:50. The precipitant was washed by DI water for three times and followed by filtration, drying, and calcination at 650°C for 8 h. The final MDC-NiO powders were then obtained. The overall synthesis steps are summarized in Figure 3.1 schematically.

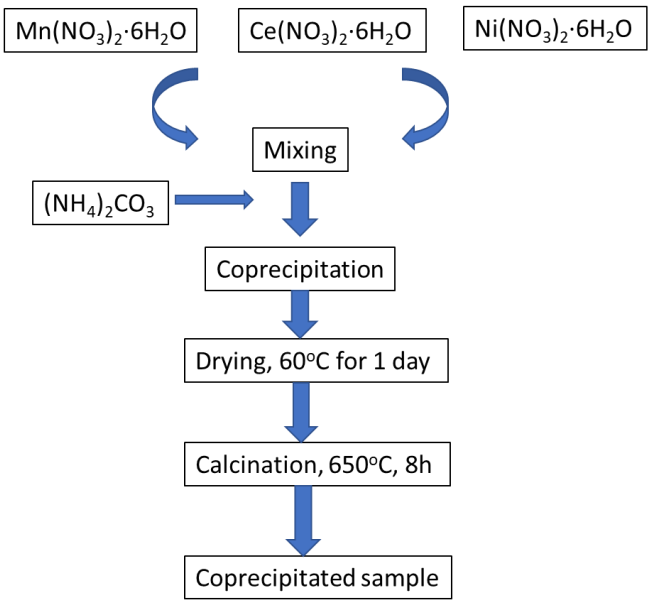

Figure 3.1 Synthesis steps for co-precipitation method

3.2 CHARACTERIZATION TECHNIQUES FOR POROUS MATRIX AND MEMBRANES

The traditional CO_2/O_2 oxidative conversion membranes have a performance-limiting factor, i.e. the multi-phase boundary for the oxygen pathway is too low, which results in low oxygen to carbon dioxide ratio. i.e., J_{O2}/J_{CO2}. To increase the ratio, pure CO_2 pathway should be shut down and converted to CO_2/O_2 co-transport pathway. To do so, the oxygen transport pathway should be expanded from 1D to 2D. The way to achieve this is to introduce an electron-conducting phase into the CeO_2 phase. In this case, we propose to study transition metal doped CeO_2 as a replacement for SDC. The transition metal used in this research work is Mn. There are several critical studies that need to be conducted, including determination of the upper limit of dopant, electrical conductivity of MDCs under pertinent temperatures and atmospheres, microstructural characterization of porous MDC-NiO matrix, J_{O2}/J_{CO2} measurement of the down-selected MDC-NiO-MC membrane.

3.2.1 XRD

The phase composition of the fabricated porous matrices and membranes were examined by X-ray diffraction (XRD) by X-ray diffractometer (Rigaku, Japan) equipped with graphite-monochromatized CuKa radiation (λ=1.5418 Å) using a scanning rate of 5^o min^{-1} in the 2θ range from 10 to 80^o.

To determine the upper limit of Mn doping, solid-state method was used to prepare samples with different Mn dopants. The solid-state method is the most widely used method in which a mixture of solid reactants is mixed and heated to high temperatures to produce a new solid composition. Here 2%, 4%, 6%, 8%, 10%, 12%

(mol%) MDC were prepared. MnO_2 and CeO_2 are mixed stoichiometrically and then heated up to 1350^oC for 10h. The phase composition was then analyzed by XRD to determine the maximum Mn doping. The XRD patterns are shown in Figure 3.2. It is evident that the maximum Mn doping content is 6 mol%, above which, MnO as an impurity appears.

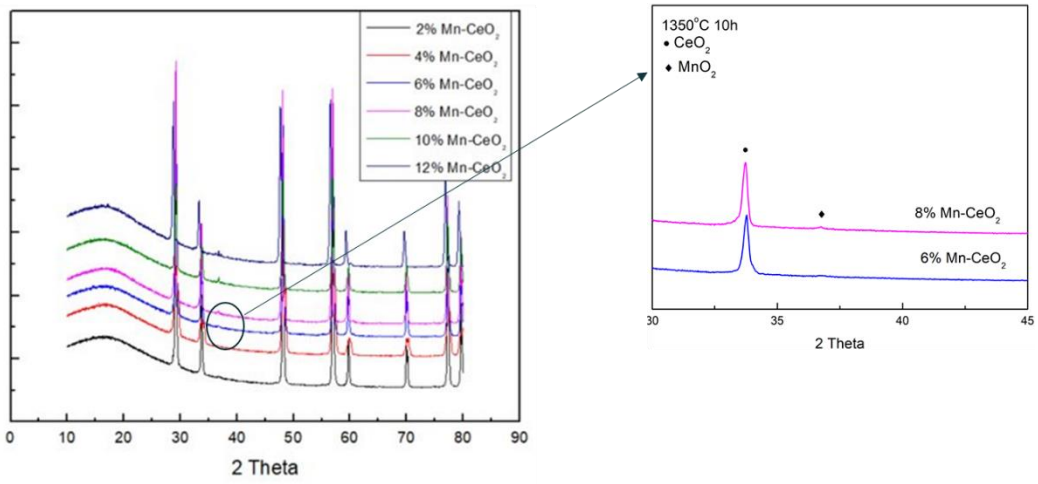

Figure 3.2 XRD patterns at different Mn doping amount in MDC

3.2.2 SEM

The microstructures of obtained porous oxide and metal matrices were examined by a field emission scanning electron microscopy (FESEM, Zeiss Ultra) equipped with an energy-dispersive X-ray spectroscopy (EDS) analyzer. For non-conductive samples, a thin layer of Au was coated on the surface by a gold sputtering coater. The microstructure of the surface and cross-section of the porous matrix is shown in Figure 3.3 (a) and (b), respectively and the cross-sectional views of the feed-gas side and sweep-gas side after MC infiltration and testing are shown in Figure 3.3 (c) and (d), respectively. From these microstructural observations, it is concluded that a porous MDC-NiO matrix and a dense MDC-NiO-MC membrane can be formed.

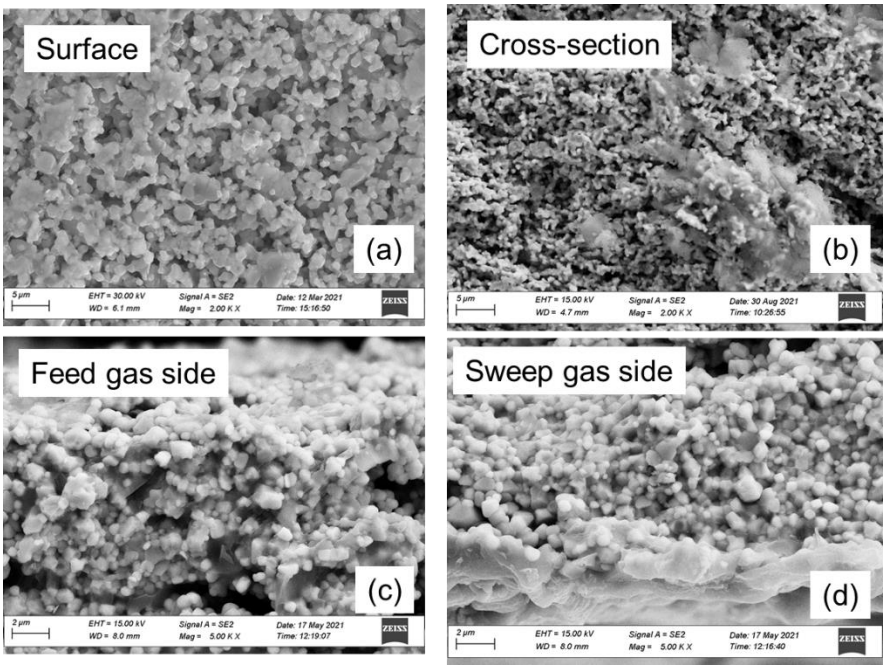

Figure 3.3 Microstructures of the MDC-NiO-MC membrane

3.2.3 Porosity measurement of the porous MDC-NiO matrix

The apparent density of a material is defined as the ratio of the mass of the material to the volume occupied by solid material and by all the pores. When there are no pores, the ratio of the mass of the material to the actual volume of the material is its theoretical density. Pores are divided into interconnected pores (connected to the surface) and closed pores (not connected to the surface). Ceramic materials prepared from powder sintering usually contain both types of pores. Apparent density is usually measured by Archimedes' method. Porosity can also be derived from apparent density.

In this research work, the porosity was measured by fluid saturation, based on Archimedes' principle. The basic procedure is to saturate the pores with a gas or a liquid. The measurement steps is illustrated in Figure 3.4. The open porosity can be deduced from measuring the volume of gas required to saturate the porous material. To accurately measure the pore volume, the sample needs to be first degassed by vacuum before

saturating the sample with fluid (water). The difference between dry and wet weight provides the information of pore volume. The advantage of the fluid saturation method is its simplicity, while the disadvantage of this method is the low accuracy due to the difficulty to saturate closed pores.

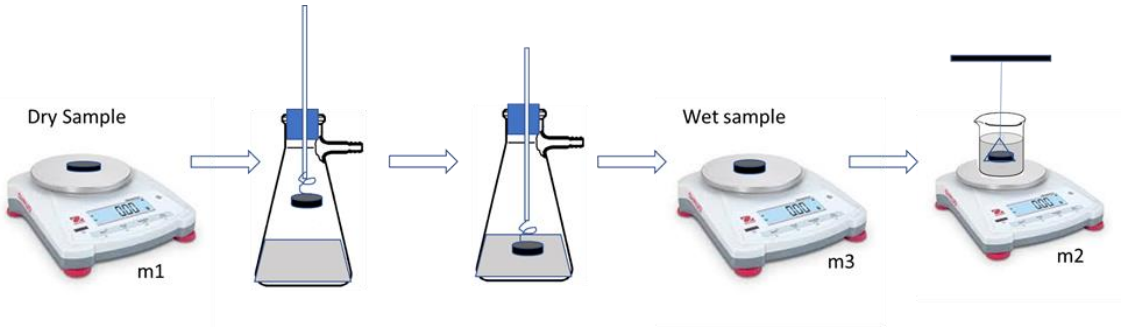

Figure 3.4 The procedure of Archimedes porosity measurement

To measure the porosity of a porous ceramic sample, the dry sample is first weighed in air and the weight is denoted as m_1. After that, the dry sample is suspended in a cone flask and evacuated the flask for 5 minutes. Then the sample is dropped into the deionized water for 5 minutes to allow water to fully go into the pores. Then, the sample is pulled out and tapped off the surface water from the top-bottom surface gently, followed by measuring the weight, m_3. Lastly, weigh the wet sample in DI water and record the weight, m_2.

The following equations are used to calculate porosity:

Total volume (V_t) of the sample including solid and pores:

$$V_t = \frac{m_2}{\rho_{H_2O}} \tag{3-1}$$

The pore volume is:

$$V_p = \frac{m_3 - m_1}{\rho_{H_2O}} \tag{3-2}$$

Porosity:

$$\varepsilon = \frac{m_3 - m_1}{m_2} \tag{3-3}$$

Using this method, the average weight of the porous matrix is m_1= 0.495g, m_3=0.558g, m2=0.525g, so the calculated average porosity of this porous matrix is 12%.

3.2.4 Nonsteady-state helium permeation test

To obtain more details on the microstructure, nonsteady-state helium permeation was performed on the porous matrix. The permeation flux and transmembrane differential pressure are measured to indirectly obtain microstructural information (see below theoretical basis). A schematic setup for the test is shown in Figure 3.5. Figure 3.6 shows the actual device built for the measurement.

Before starting the experiment, it is recommended that the user wears safety glasses and gloves for safety reasons since the device is under pressure. For a typical run, first, set the pressure to approximately 30 psi. Then, seal the membrane in the sample chamber using silicone paste. After that, close valve 9 and open valves 5 and 6 fully, turn valve 7 towards valve 8, turn on valve 8 fully and open valve 1. Set mass flow controller to 50 sccm. Check for leakage of the gas at all connections, which can be done by applying a snoop solution to points of connection. If there are no bubbles forming, that means there is no significant leakage. Read the pressure difference using the pressure differential sensor (ΔP, unit in psi). If ΔP<10psi, change the flow rate of the mass flow controller from 50sccm to 100/150/200sccm until the sensor is shown above 10 psi. Close valves 5 and 6, turn on valve 9, and wait until the system stabilizes. Read the pressure on the mass flow controller (P_{amb}). Close valve 9, turn on valves 5 and 6, and wait for the system to stabilize. After that, measure the flow rate of helium in the system three times with the bubble flow meter. Read ΔP and P_h and pressure on mass flow controller (P_{mf}).

Close valve 8 by turning ~10 times until ΔP decreases by ~ 1 psi. Record ΔP, P_h, P_{mf}, and flow rate. Close valve 8 slightly again until ΔP decreases by ~ another 1 psi and record ΔP, P_h, P_{mf}, and flow rate again. Repeat until ΔP<2 psi. When the operation is done, set the mass flow controller to 0 and turn the helium cylinder off, close off valves 5 and 6, turn on vales 9 and 8 to release the pressure.

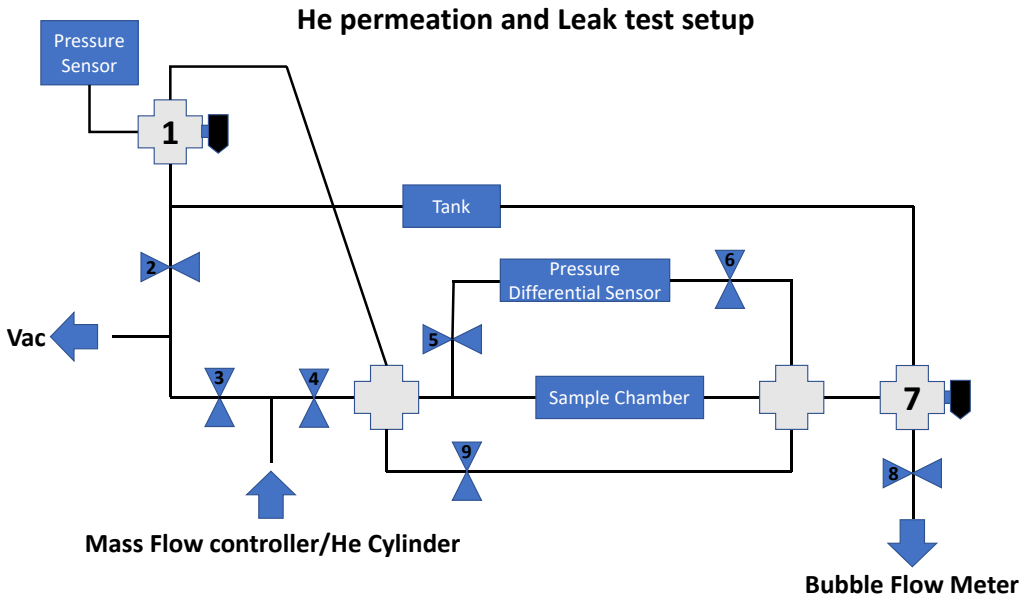

Figure 3.5 Schematic setup for Helium permeation and leak test

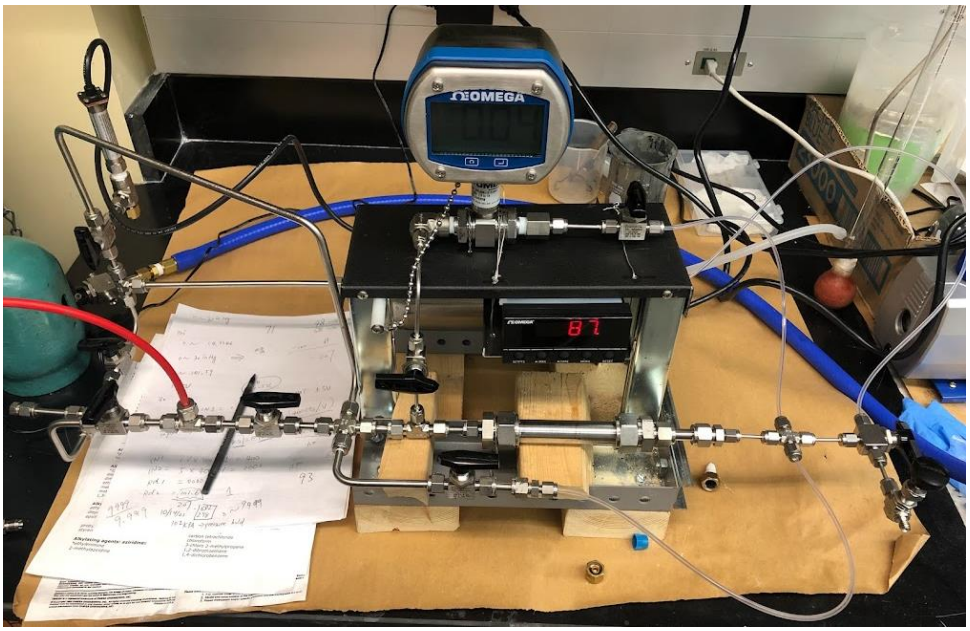

Figure 3.6 Experimental setup for Helium permeation and leak test

After the operation, the helium permeance is obtained and then graphed as a function of average pressure and fitted to the following equation to obtain α and β:

$$\left(\frac{F}{L}\right) = \alpha + \beta * P_{avg} \tag{3-4}$$

Where F/L=permeance (usual units of moles/m^2·Pa·s)

L=membrane thickness, cm

α=Knudsen flow parameter

β=viscous flow parameter

P_{avg}=average pressure across the membrane

Here the permeance through the membrane is defined as:

$$\left(\frac{F}{L}\right) = \left(\frac{Q}{S \cdot (P_h - P_l)}\right) \tag{3-5}$$

Q=molar flow rate of permeating species

S=area of the membrane that is exposed to the permeating gas, close to the area of sampling sealing tube

P_h=upstream pressure

P_l=downstream pressure

Here Q can be calculated from bubble flow rate reading (unit: sccm, cc/min) and converted to mol/s.

The average pressure P_{avg} is calculated by

$$P_{avg} = \frac{P_h + P_l}{2} = \frac{P_h + P_l - \Delta P}{2} = P_h - \frac{\Delta P}{2} = P_{mf} - P_{amb} - \frac{\Delta P}{2} \quad (3\text{-}6)$$

$$P_h - P_l = \Delta P \quad (3\text{-}7)$$

Plot (F/L) against P_{avg}, and extract α from the intercept of the fitted equation and β from the slope, the average pore radius r of the pores in the matrix is calculated by:

$$r = 8.4818\mu \sqrt{\frac{RT}{M_w}} \left(\frac{\beta}{\alpha}\right) \quad (3\text{-}8)$$

Where r=average pore radius

R=gas constant with matching units

T=temperature

Mw=molecular weight

μ= viscosity of permeating gas

The plot of permeance against P_{avg} for MDC-NiO porous matrix is shown in Figure 3.7, from which the average pore radius diameter is calculated to be 137.39 nm and the tortuosity is 6.9.

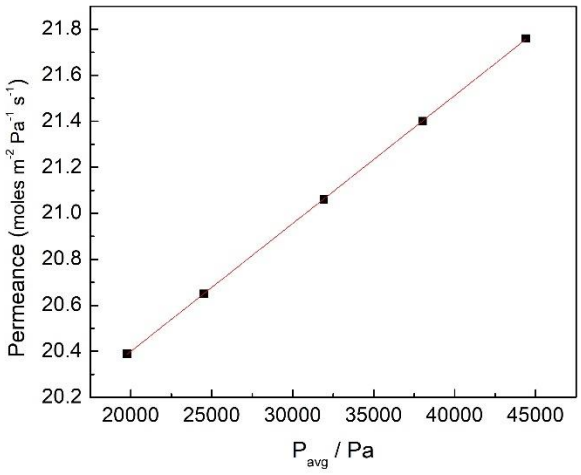

Figure 3.7 Helium permeation vs. average pressure

3.2.5 Conductivity measurement

Conductivity is a parameter used to describe the ease with which charge flows in a substance. The value of conductivity is equal to the current density multiplied by the strength of the electric field in the medium. The standard unit of electrical conductivity is Siemens/meter. When a 1A current passes through a cross-section of an object with a voltage of 1V, the conductivity of the object is 1S. The conductivity of the material is equal to the reciprocal of the resistivity:

$$\sigma = \frac{1}{\rho} = \frac{1}{R} \times \frac{l}{A} \tag{3-9}$$

Where R is resistance, l is the length of the sample and A is the cross-section area of the sample.

The conductivity of different materials varies greatly. For electronic conductors, silver is the best, followed by copper. For ionic conductors, the conductivity is often determined by the concentration of active ions in electrolytes. The conductivity of most metals is much higher than the ionically conducting electrolytes. Therefore, it is more

convenient to introduce the concept of conductivity in order to compare with other conductors more intuitively.

According to the ampere formula, the resistance of a conductor is calculated by measuring the current passing through the conductor and the corresponding voltage drop. The geometric size of the sample is measured and conductivity can be calculated by equation (3-9). This method is known as the direct current method, which includes the two-probe method and four-probe method. This kind of method is mainly aimed at testing pure electronic conductive materials. When measuring the mixed conductor, that is, when the conductor contains both electron and ion carriers, the charge transfer impedance will affect the measurement due to the irreversible ionic conductivity. Therefore, the direct current method often chooses the ion blocking electrode to make the measurement of electron conductivity more accurate.

Four-probe method is a widely used standard method, which has the advantages of convenient operation, high accuracy, and no strict requirements on sample shape[75]. The four-probe method test setup is shown in Figure 3.8; it is an improvement on the two-probe method. By adding two probes between the current probes, the influence of contact resistance is eliminated to a large extent. In the four-probe method, the measuring circuit and the current circuit are in parallel. Resistance in the loop does not affect the results. Therefore, regardless of the resistance of the sample, as long as the size of the test sample is large enough, the measurement result is accurate enough. In addition, in order to further eliminate the contact resistance and injection effect of the voltage probe itself, the four-probe method also uses the compensation method to measure the voltage, so that the current does not have to pass through the voltage probe and the measured resistance is

more accurate. The most commonly used four-probe test device is the liner four-probe test device, where four probes are arranged in a straight line at equal spacing. Therefore, the calculation of resistivity of the sample can be simplified into equation (3-9)

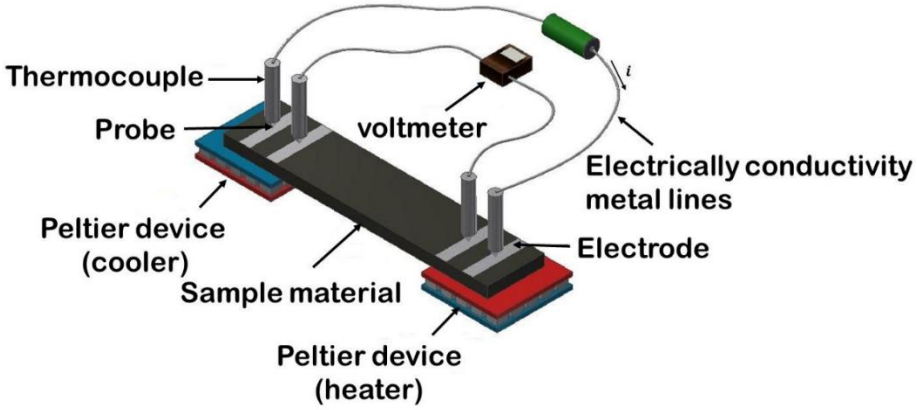

Figure 3.8 Conceptual schematic of four-probe measurement method[76]

In this research work, the conductivity of MDC bar samples in dimension of 25mm×3.0mm×5.0mm with different doping amounts was measured using a standard four-probe method in air and hydrogen atmosphere from 550 to 850^{o}C with the E-I module in the Corr-Ware software within a Solartron 1287/1260 electrochemical workstation system.

After the conductivity of the materials is collected, an Arrhenius plot can be obtained by plot of ln(σT) against 1000/T. Arrhenius plots can be used to analyze the effect of temperature on the rates of chemical reactions. For a single rate-limited thermally activated process, an Arrhenius plot gives a straight line, from which the activation energy and the pre-exponential factor can be determined. Arrhenius plot of MDCs under air and under reducing atmosphere is shown in Figure 3.9.

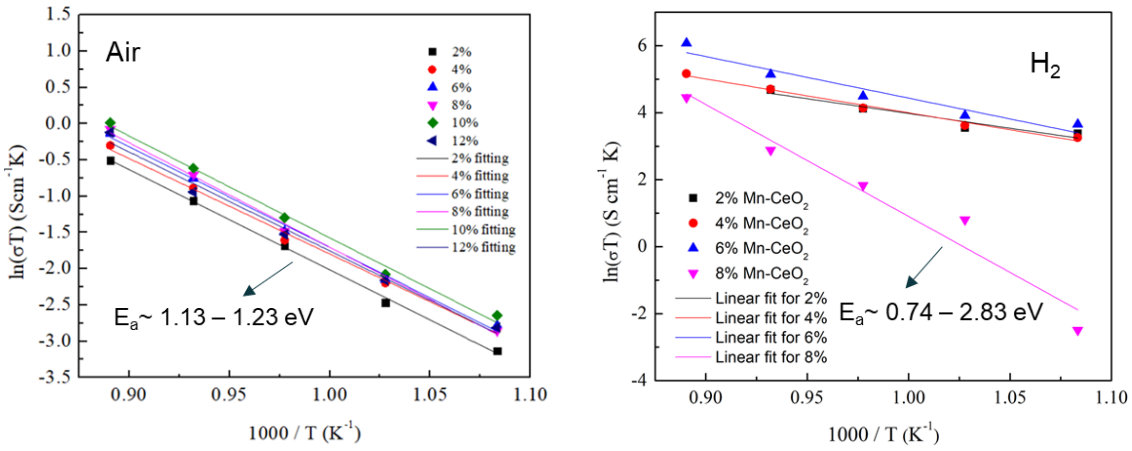

Figure 3.9 Arrhenius plots for different MDCs in air and hydrogen atmosphere

From the plots, it is obvious that the activation energy of different MDC under the air is almost the same, while 6% Mn-CeO_2 shows significant increases in H_2 atmosphere.

3.2.6 CO_2/O_2 flux measurement

After the MDC and NiO mixture was prepared by co-precipitation method, the powders were then mixed with carbon black and PVB in ethanol in the volume ratio of 4:6. The dried powder mixtures were pressed into pellets and sintering at 1300^{o}C for 10 h in air to remove the pore former and achieve the desired mechanical strength. Finally, a membrane with an area of 0.916cm^2, thickness of 0.81mm is obtained. The porous NiO-MDC membrane was then sealed on the alumina tube by a commercial silver paste as the sealant (Shanghai Research Institute of Synthetic Resins). The eutectic MC powder mixture (52 mol% Li_2CO_3 and 48 mol% Na_2CO_3) was gently placed on the top surface of the membrane. Upon heating to > 500^{o}C, the MC melts and generally flows into the pores of the membrane and in-situ reacts with NiO to form $LiNiO_2$.

The flux densities of CO_2/O_2 permeation of the membrane were measured by a homemade permeation system as shown in Figure 3.10. The upper side of the membrane is connected with the feed gas (100 sccm flow of the mixture containing 75% N_2, 15%

CO_2, and 10% O_2), while the lower side of the membrane is connected with the sweep gas (50 sccm flow of Ar for CO_2-O_2 permeation testing or Ar-CH_4 mixture for methane conversion testing). The N_2 in feed gas was also used as a tracer gas for leakage correction. The concentrations of CO_2, O_2, and N_2 in the sweep side were analyzed by an online gas chromatographer (Agilent micro-GC 490). Commercial mass flow controllers (Smart-Trak, 50 Series) were employed to control the gas flow rates and were specifically calibrated for each gas before use. The temperature studied for the CO_2-O_2 permeation testing was held at 850°C for the stability test. The final CO_2 and O_2 flux densities (J_{CO2} and J_{O2}) were calculated by:

$$J_{CO_2} = \frac{C_{CO_2}}{(1 - C_{CO_2} - C_{O_2} - C_{N_2})} \times \frac{Q}{A} \tag{3-10}$$

$$J_{O_2} = \frac{C_{O_2}}{(1 - C_{CO_2} - C_{O_2} - C_{N_2})} \times \frac{Q}{A} \tag{3-11}$$

Where C_{CO2}, C_{O2}, and C_{N2} are the concentration of CO_2, O_2, and N_2, respectively; Q is the flow rate of the sweep gas; A is the effective area of the membrane.

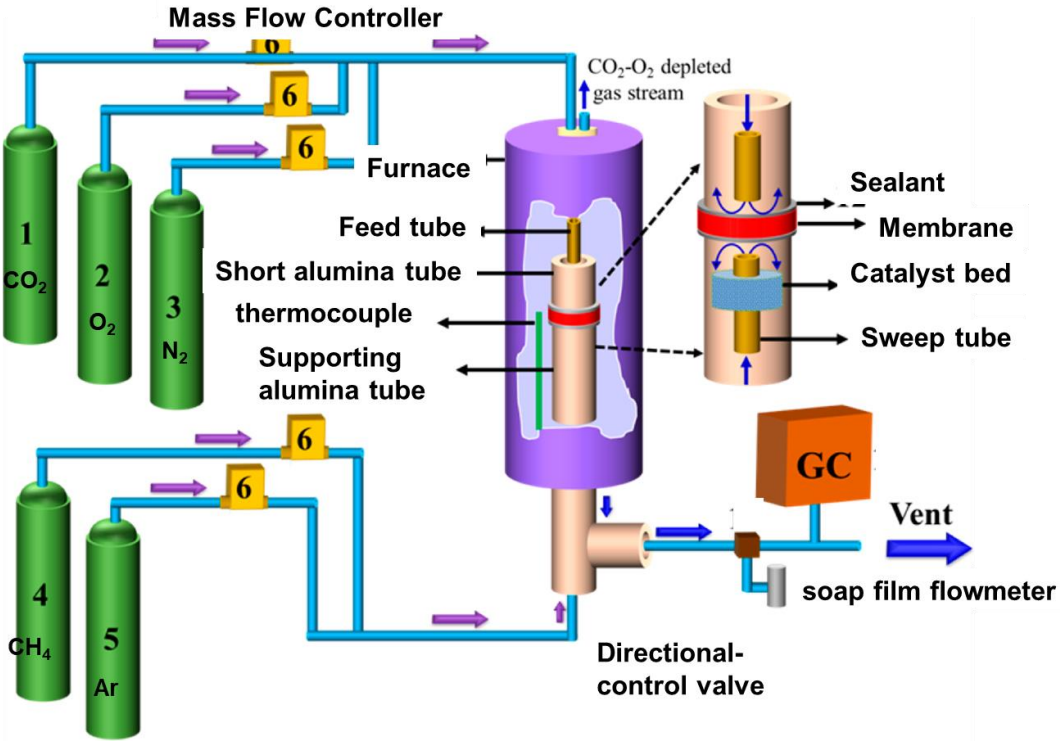

Figure 3.10 Schematic of the CO_2 permeation cell configurations

To determine the most appropriate amount of MC loading, membranes with different amounts of MC were tested. The fluxes of O_2, N_2, and CO_2 are shown in Figure 3.11. A further comparison between the fluxes of the membrane among different amounts of molten carbonate loading is shown in Figure 3.12.

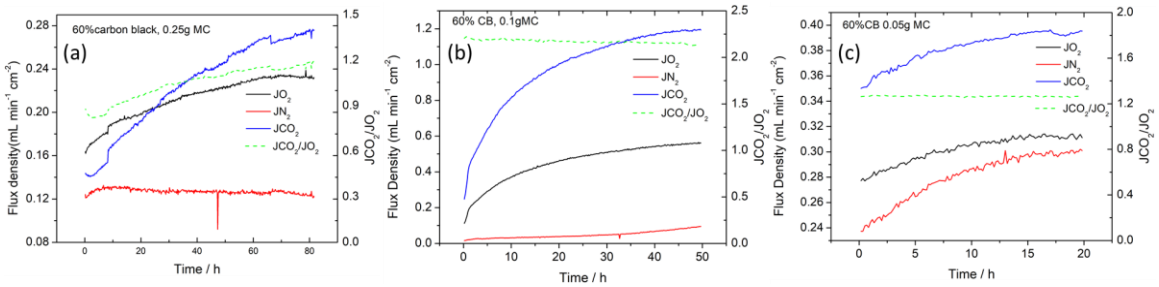

Figure 3.11 Flux measurement of membrane with different amount molten carbonate: (a) 0.25g molten carbonate; (b) 0.1g molten carbonate; (c) 0.05g molten carbonate

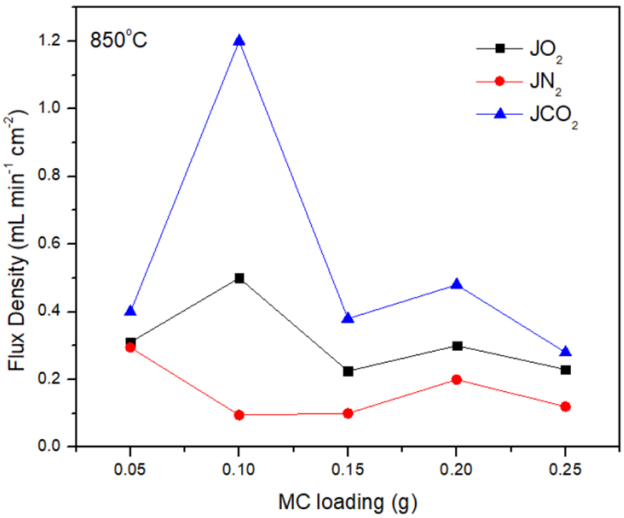

Figure 3.12 Flux comparison of the membrane with different molten carbonate amounts

It is obvious that among different MC loading, 0.1g shows the best performance for a matrix containing 16% porosity. The Arrhenius plot for the 0.1g MC loaded membrane at 650 to 850°C is shown in Figure 3.13. The activation energy of O_2 and CO_2 are similar, which are 46.5 and 52.93 kJ/mol, respectively.

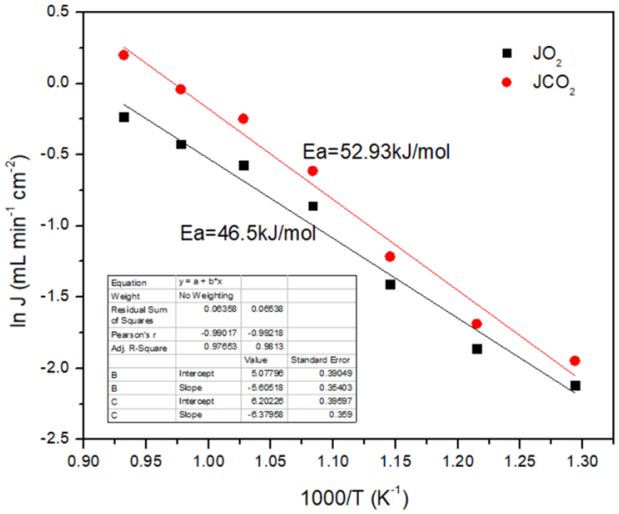

Figure 3.13 Arrhenius plot for O_2 and CO_2 flux

3.2.7 Verification of the three transport paths

To verify the activation of the three paths of the triple-phase membrane, different feed gas compositions as shown in Table 3.1 were applied to the system and the

corresponding fluxes were measured. The results of CO_2 and O_2 flux are shown in Table 3.2. When using the flue gas as the feed gas, all three paths are activated. When O_2 inflow is stopped, none of the three paths is activated since O_2 or O^{2-} are required in all these three transport paths, as such both CO_2 and O_2 fluxes are decreased dramatically. When CO_2 inflow is stopped, the oxygen transport pathway is still activated, so only the flux of O_2 remains the same.

Table 3.1 Feed gas compositions to verify the activation of three paths

	O_2	N_2	CO_2	Active path
Flue gas	10 sccm	75 sccm	15 sccm	$CO_2 + 1/2\,O_2 + 2e^-{}_{(LNO)} = CO_3^{2-}{}_{(MC)}$ $O^{2-}{}_{(MDC)} + CO_2 = CO_3^{2-}{}_{(MC)}$ $1/2\,O_2 + 2e^-{}_{(MDC)} = O^{2-}{}_{(MDC)}$
Stop O_2	0 sccm	85 sccm	15 sccm	$O^{2-}{}_{(MDC)} + CO_2 = CO_3^{2-}{}_{(MC)}$
Stop CO_2	10 sccm	90 sccm	0 sccm	$1/2\,O_2 + 2e^-{}_{(MDC)} = O^{2-}{}_{(MDC)}$

Table 3.2 Flux density results for the verification of three transport paths

	J_{O2}(mL min^{-1} cm^{-2})	J_{CO2}(mL min^{-1} cm^{-2})	J_{CO2}/J_{O2}
Flue gas	0.56068	1.19203	2.12
Stop O_2	0.016353	0.157122	9.61
Stop CO_2	0.53232	0.037758	0.07

3.3 CONCLUSION

In conclusion, the 6% Mn-doped CeO_2 is t upper limit of dopant amount and it was selected as the desired materials for the further high-temperature CO_2/O_2 co-

transport membrane. The MDC-NiO mixture powder was synthesis by co-precipitation method successfully and then used to sintering to porous matrix. The eutectic molten carbonate was used to seal the pores and in-situ react with the NiO to form LNO. The 0.1g loading amount shows the best performance among different molten carbonate doping amount.

CHAPTER 4

ANALYTICAL SOLUTIONS OF FLUX DENSITY IN HIGH TEMPERATURE CO_2 CAPTURE MEMBRANE[1]

There are two basic types of high-temperature dual-phase membranes previously defined for CO_2 separation [77-79]: mixed oxygen-vacancy and carbonate-ion conducting (denoted as MOCC) and mixed electron and carbonate-ion conducting (denoted as MECC); Figure 4.1a and 4.1b schematically illustrate their individual chemistry. In MOCC membranes, the surface reaction of CO_2 with lattice oxygen O_o^x and MC at the triple phase (gas/oxide/MC) boundaries takes place to results in a gradient of chemical potentials and thus transport of oxygen vacancies ($V_o^{\cdot\cdot}$) and carbonate ions (CO_3^{2-}) in separate phase across the membrane. Similarly, in MECC membranes, the surface reduction of CO_2 and O_2 by electrons (e^-) enables the transport of CO_2 via MC phase under a gradient of chemical potentials of CO_2 and O_2.

---

[1] Xin Li, Kevin Huang, and Xinfang Jin, 2020. Journal of The Electrochemical Society. 167: 165412. Reprinted here with permission of the publisher.12/07/2020

Two additional membranes derived from MOCC and MECC are also shown in Figure 4.1c and 4.1d. In Figure4.1c, a mixed oxygen-vacancy and electron (or electron hole) conducting (MOEC) solid oxide (SO) phase is mixed with the MC phase to form a membrane (denoted as MOECC); therefore, CO_2 transport is carried by both MOCC and MECC chemistries. In Figure 4.1d, a third pure electron conducting (LNO) phase is introduced into the MOECC membrane, which becomes a triple-phase membrane (denoted as MOEECC). While the CO_2 transport chemistry remains the same to MOECC, the additional electron/hole transporting phase offers more reaction pathways to produce CO_3^{2-} for CO_2 transport. In the following mathematical models to solve CO_2 flux, we consider the above surface reaction equilibria at multiphase interfaces in CO_2 transport.

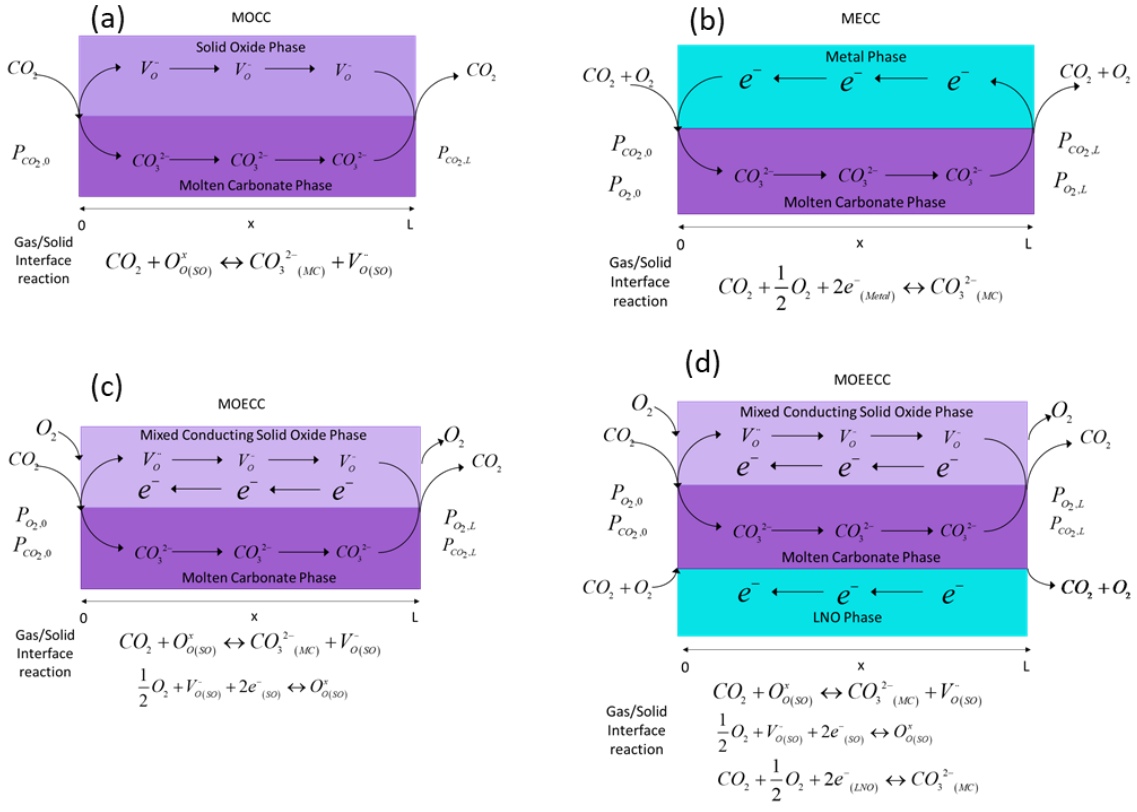

Figure 4.1 Transport mechanisms in different membranes: (a)MOCC; (b)MECC; (c)MOECC; (d)MOEECC

Considering a 1D computational domain across the thickness direction of each membrane, to get the analytical solution for second-order partial differential equations, a basic idea is to integrate the second-order Ohm's law twice and then implement the boundary conditions to solve for the unknown parameters.

4.1 DERIVATION OF MOCC ANALYTICAL SOLUTION

In an MOCC membrane, oxygen vacancies are transporting in the solid oxide phase and carbonate ions are transporting in the molten carbonate phase. And they are coupled by surface reactions, as shown in Figure 4.1a. Only CO_2 is permeating through the membrane.

Governing equation and boundary conditions in the solid oxide phase:

$$\nabla \cdot J_V = -\frac{(1-\varepsilon)}{\tau_{SO}}\left(\frac{{Z_V}^2 F^2 D_V C_V}{RT}\nabla^2\phi_{SO}\right) = -\frac{(1-\varepsilon)}{\tau_{SO}}\sigma_V\nabla^2\phi_{SO} = 0 \tag{4-1}$$

$$\phi_{SO} = \frac{RT\left(ln\frac{P_{CO_2,0}}{P^0}\frac{C^0}{C_V}\right) - \beta}{FZ_V} \tag{4-2}$$

$$J_V + J_C = 0 \tag{4-3}$$

Second governing equation and boundary conditions in molten carbonate phase:

$$\nabla \cdot J_C = -\frac{\varepsilon}{\tau_{MC}}\left(\frac{{Z_C}^2 F^2 D_C C_C}{RT}\nabla^2\phi_{MC}\right) = -\frac{\varepsilon}{\tau_{MC}}\sigma_C\nabla^2\phi_{MC} = 0 \tag{4-4}$$

$$\phi_{MC}(x=0) = 0 \tag{4-5}$$

$$\phi_{MC} = \frac{RT\left(ln\frac{P_{CO_2,L}}{P^0}\frac{C^0}{C_V}\right) - \beta}{FZ_C} - \frac{Z_V\phi_{SO}}{Z_C} \tag{4-6}$$

Parameters:

$$\sigma_C = \frac{{Z_C}^2 F^2 D_C C_C}{RT} \tag{4-7}$$

$$\sigma_V = \frac{{Z_V}^2 F^2 D_V C_V}{RT} \tag{4-8}$$

Integration of equation (4-1) and (4-4) with respect to x twice yields,

$$\phi_{SO} = -\frac{C_1}{(1-\varepsilon)/\tau_{SO}\sigma_V} x - \frac{C_2}{(1-\varepsilon)/\tau_{SO}\sigma_V} \tag{4-9}$$

$$\phi_{MC} = -\frac{C_3}{\varepsilon/\tau_{MC}\sigma_C} x - \frac{C_4}{\varepsilon/\tau_{MC}\sigma_C} \tag{4-10}$$

Substitution of eq (4-5) into (4-10) results in C4=0, thus Eq. (4-10) becomes,

$$\phi_{MC} = -\frac{C_3}{\varepsilon/\tau_{MC}\sigma_C} x \tag{4-11}$$

From Eq. (4-3),

$$C_1 = -C_3 \tag{4-12}$$

Substitution of Eq. (4-12) into Eq. (4-11) yields,

$$\phi_{MC} = \frac{C_1}{\varepsilon/\tau_{MC}\sigma_C} x \tag{4-13}$$

According to Eq. (4-2) and Eq. (4-9),

$$C_2 = -\frac{(1-\varepsilon)/\tau_{SO}\sigma_V}{FZ_V}\left[RT\left(ln\frac{P_{CO_2,0}}{P^0}\frac{C^0}{C_V}\right) - \beta\right] \tag{4-14}$$

According to Eq. (4-6), Eq. (4-9), and Eq. (4-14) become,

$$C_1 = \frac{RT\left(ln\frac{P_{CO_2,L}}{P_{CO_2,0}}\right)}{FZ_C\left(\frac{L}{\varepsilon/\tau_{MC}\sigma_C} - \frac{Z_V}{Z_C}\frac{L}{(1-\varepsilon)/\tau_{SO}\sigma_V}\right)} \tag{4-15}$$

The complete solutions are:

$$\emptyset_{MC} = \frac{x}{L}\frac{1}{FZ_C\left(1-\frac{Z_V}{Z_C}\frac{\varepsilon/\tau_{MC}\sigma_C}{(1-\varepsilon)/\tau_{SO}\sigma_V}\right)}RT(\ln\frac{P_{CO_2,L}}{P_{CO_2,0}}) \tag{4-16}$$

$$\emptyset_{SO} = -\frac{x}{L}\frac{1}{FZ_C\left(\frac{(1-\varepsilon)/\tau_{SO}\sigma_V}{\varepsilon/\tau_{MC}\sigma_C}-\frac{Z_V}{Z_C}\right)}RT\left(\ln\frac{P_{CO_2,L}}{P_{CO_2,0}}\right) + \frac{1}{FZ_V}\left[RT\left(\ln\frac{P_{CO_2,0}}{P^0}\frac{C^0}{C_V}\right)-\beta\right] \tag{4-17}$$

$$N_C = \frac{RT}{LZ_CF^2}\frac{\varepsilon/\tau_{MC}\sigma_C\,(1-\varepsilon)/\tau_{SO}\sigma_V}{(\varepsilon/\tau_{MC}\sigma_C Z_V-(1-\varepsilon)/\tau_{SO}\sigma_V Z_C)}(\ln\frac{P_{CO_2,L}}{P_{CO_2,0}}) \tag{4-18}$$

$$N_V = -\frac{RT}{LZ_VF^2}\frac{\varepsilon/\tau_{MC}\,\sigma_C\,(1-\varepsilon)/\tau_{SO}\sigma_V}{(\varepsilon/\tau_{MC}\,\sigma_C Z_V-(1-\varepsilon)/\tau_{SO}\sigma_V Z_C)}(\ln\frac{P_{CO_2,L}}{P_{CO_2,0}}) \tag{4-19}$$

4.2 DERIVATION OF MECC ANALYTICAL SOLUTION

In an MECC membrane, electrons are transporting in the metal phase and carbonate ions are transporting in the molten carbonate phase. And they are coupled by surface reactions, as shown in Figure 4.1b. Both CO_2 and O_2 are permeating through the membrane.

First governing equation and boundary conditions in the metal phase:

$$\nabla\cdot J_e = -\frac{(1-\varepsilon)}{\tau_m}\sigma_e\nabla^2\phi_e = 0 \tag{4-20}$$

$$\phi_e = \frac{\alpha}{2Z_eF}-\frac{RT}{2Z_eF}ln\frac{P_{CO_2}}{P^0}\left(\frac{P_{O_2}}{P^0}\right)^{0.5} \tag{4-21}$$

$$J_e + J_C = 0 \tag{4-22}$$

Second equation and boundary conditions in the molten carbonate phase:

$$\nabla J_C = -\frac{\varepsilon}{\tau_{MC}}\sigma_C\nabla^2\phi_{MC} = 0 \tag{4-23}$$

$$\phi_{MC}(x=0) = 0 \tag{4-24}$$

$$\phi_{MC} = -\frac{\alpha}{Z_C F} + \frac{RT}{Z_C F} ln \frac{P_{CO_2}}{P^0} \left(\frac{P_{O_2}}{P^0}\right)^{0.5} + \frac{2Z_e}{Z_C} \phi_e \tag{4-25}$$

Parameters:

$$\sigma_C = \frac{{Z_C}^2 F^2 D_C C_C}{RT} \tag{4-26}$$

$$\sigma_e = \frac{{Z_e}^2 F^2 D_e C_e}{RT} \tag{4-27}$$

Integration of equation (4-20) and (4-22) with respect to x twice yields

$$\phi_e = -\frac{C_1}{(1-\varepsilon)/\tau_m \sigma_e} x - \frac{C_2}{(1-\varepsilon)/\tau_m \sigma_e} \tag{4-28}$$

$$\phi_{MC} = -\frac{C_3}{\varepsilon/\tau_{MC} \sigma_C} x - \frac{C_4}{\varepsilon/\tau_{MC} \sigma_C} \tag{4-29}$$

Substitution of eq (4-22) into (4-27) results in C4=0, then

$$\phi_{MC} = -\frac{C_3}{\varepsilon/\tau_{MC} \sigma_C} x \tag{4-30}$$

From Eq. (4-20), Eq. (4-26) and (4-28),

$$C_1 = -C_3 \tag{4-31}$$

So, Eq. (4-28) becomes,

$$\phi_{MC} = \frac{C_1}{\varepsilon/\tau_{MC} \sigma_C} x \tag{4-32}$$

According to Eq. (4-19) and (4-26),

$$C_2 = -\frac{(1-\varepsilon)/\tau_m \sigma_e}{2Z_e F} \left(\alpha - RT\ ln \frac{P_{CO_2,0}}{P^0} \left(\frac{P_{O_2,0}}{P^0}\right)^{0.5}\right) \tag{4-33}$$

According to Eq. (4-23), Eq. (4-30) and (4-31),

$$C_1 = \frac{RT}{Z_C F L} \frac{ln \frac{P_{CO_2,L}}{P_{CO_2,0}} \left(\frac{P_{O_2,L}}{P_{O_2,0}}\right)^{0.5}}{\left(\frac{1}{\varepsilon/\tau_{MC}\sigma_C} + \frac{2Z_e}{Z_C}\frac{1}{(1-\varepsilon)/\tau_m\sigma_e}\right)} \tag{4-34}$$

The complete solutions are:

$$\emptyset_{MC} = \frac{x}{L}\frac{1}{FZ_C\left(1 + \frac{2Z_e}{Z_C}\frac{\varepsilon/\tau_{MC}\sigma_C}{(1-\varepsilon)/\tau_m\sigma_e}\right)} RT(\ln\frac{P_{CO_2,L}}{P_{CO_2,0}})(\frac{P_{O_2,L}}{P_{O_2,0}})^{0.5} \tag{4-35}$$

$$\emptyset_{e,m} = -\frac{x}{L}\frac{\frac{RT}{Z_c F}\ln\frac{P_{CO_2,L}}{P_{CO_2,0}}\left(\frac{P_{O_2,L}}{P_{O_2,0}}\right)^{0.5}}{FZ_C\left(\frac{(1-\varepsilon)/\tau_m\sigma_e}{\varepsilon/\tau_{MC}\sigma_C} + 2\frac{Z_e}{Z_C}\right)} + \frac{\alpha}{2Z_e F} - \frac{RT}{2Z_e F}\ln\frac{P_{CO_2,0}}{P^0}(\frac{P_{O_2,0}}{P^0})^{0.5} \tag{4-36}$$

$$N_C = -\frac{1}{Z_C L}\frac{\varepsilon/\tau_{MC}\,\sigma_C\,(1-\varepsilon)/\tau_m\sigma_e}{(Z_C\,(1-\varepsilon)/\tau_m\sigma_e + 2\,Z_e\varepsilon/\tau_{MC}\sigma_C)}\frac{RT}{F^2}\ln\frac{P_{CO_2,L}}{P_{CO_2,0}}(\frac{P_{O_2,L}}{P_{O_2,0}})^{0.5} \tag{4-37}$$

$$N_e = \frac{1}{Z_e L}\frac{\varepsilon/\tau_{MC}\,\sigma_C(1-\varepsilon)/\tau_m\sigma_e}{(Z_C\,(1-\varepsilon)/\tau_m\sigma_e + 2\,Z_e\varepsilon/\tau_{MC}\sigma_C)}\frac{RT}{F^2}\ln\frac{P_{CO_2,L}}{P_{CO_2,0}}(\frac{P_{O_2,L}}{P_{O_2,0}})^{0.5} \tag{4-38}$$

4.3 DERIVATION OF MOECC ANALYTICAL SOLUTION

In an MOECC membrane, both oxygen vacancies and electrons are transporting in the solid oxide phase and carbonate ions are transporting in the molten carbonate phase. All three charge carriers are coupled by surface reactions, as shown in Figure 4.1c. Both CO_2 and O_2 are permeating through the membrane. In the following derivation, $\varepsilon_{SO} = 1 - \varepsilon$,$\varepsilon_{MC} = \varepsilon$ and n is the same as e to represent electron. For the current associated with oxygen vacancy and electron in solid oxide phase and carbonate ion in molten carbonate phase,

$$J_V = -\frac{\varepsilon_{SO}}{\tau_{SO}}\left(z_V F D_V \nabla C_V + \frac{{z_V}^2 F^2 D_V C_V}{RT}\nabla\phi_{SO}\right) \tag{4-39}$$

$$J_e = -\frac{\varepsilon_{SO}}{\tau_{SO}}\frac{\sigma_e}{z_e F}(\nabla\mu_e + z_e F\nabla\phi_{SO}) \tag{4-40}$$

(4-41)

$$J_C = -\frac{\varepsilon_{MC}}{\tau_{MC}} \frac{{Z_C}^2 F^2 D_C C_C}{RT} \nabla \phi_{MC}$$

According to the interfacial reactions,

$$\nabla \mu_e = -\frac{1}{4} \nabla \mu_{O_2} - \frac{1}{2} \nabla \mu_V \tag{4-42}$$

$$\nabla \mu_{CO_2} + \frac{1}{2} \nabla \mu_{O_2} - Z_C F \nabla \phi_{MC} + 2 \nabla \mu_e + 2 Z_e F \nabla \phi_{SO} = 0 \tag{4-43}$$

Plug equation (4-38) into equation (4-39), and rearrange the equation:

$$-\frac{1}{2Z_e} \nabla \mu_{CO_2} + \frac{Z_C}{2Z_e} F \nabla \phi_{MC} = F \nabla \phi_{SO} + \frac{1}{Z_v} \nabla \mu_V \tag{4-44}$$

According to current conservation, add (4-35), (4-36) and (4-37) together, then plug (4-40) into the new equation, and rearrange the equation. After a few steps of derivation, we get,

$$-\frac{\varepsilon_{SO}}{\tau_{SO}} \frac{A}{F} \left((\sigma_V + \sigma_e) \left(-\frac{1}{2Z_e} \nabla \mu_{CO_2} + \frac{Z_C}{2Z_e} F \nabla \phi_{MC} \right) - \frac{1}{4} \frac{\sigma_e}{z_e} \nabla \mu_{O_2} \right) - A \frac{\varepsilon_{MC}}{\tau_{MC}} \frac{{Z_C}^2 F^2 D_C C_C}{RT} \nabla \phi_{MC} = 0 \tag{4-45}$$

Solve for $\nabla \phi_{MC}$ in Eq. (4-41),

$$\frac{\frac{\varepsilon_{SO}}{\tau_{SO}} \frac{1}{F} \frac{(\sigma_V + \sigma_e)}{2Z_e} \nabla \mu_{CO_2} + \frac{\varepsilon_{SO}}{\tau_{SO}} \frac{1}{4F} \frac{\sigma_e}{z_e} \nabla \mu_{O_2}}{\left[\frac{\varepsilon_{SO}}{\tau_{SO}} \frac{1}{F} \frac{Z_C}{2Z_e} (\sigma_V + \sigma_e) F + \frac{\varepsilon_{MC}}{\tau_{MC}} \frac{{Z_C}^2 F^2 D_C C_C}{RT} \right]} = \nabla \phi_{MC} \tag{4-46}$$

Plug Eq. (4-42) back to Eq. (4-37),

$$J_C = -\frac{\varepsilon_{MC}}{\tau_{MC}}\frac{{Z_C}^2F^2D_CC_C}{RT}\frac{\frac{\varepsilon_{SO}}{\tau_{SO}}\frac{1}{F}\frac{(\sigma_V+\sigma_e)}{2Z_e}\nabla\mu_{CO_2}+\frac{\varepsilon_{SO}}{\tau_{SO}}\frac{1}{4F}\frac{\sigma_e}{z_e}\nabla\mu_{O_2}}{\left[\frac{\varepsilon_{SO}}{\tau_{SO}}\frac{1}{F}\frac{Z_C}{2Z_e}(\sigma_V+\sigma_e)F+\frac{\varepsilon_{MC}}{\tau_{MC}}\frac{{Z_C}^2F^2D_CC_C}{RT}\right]} \tag{4-47}$$

Use $\sigma_C = \frac{{Z_C}^2F^2D_CC_C}{RT}$ to Substitute D_cC_c, we get,

$$J_C = -\frac{\varepsilon_{MC}}{\tau_{MC}}\frac{\sigma_C}{F}\frac{\frac{\varepsilon_{SO}}{\tau_{SO}}\frac{(\sigma_V+\sigma_e)}{2Z_e}\nabla\mu_{CO_2}+\frac{\varepsilon_{SO}}{\tau_{SO}}\frac{1}{4}\frac{\sigma_e}{z_e}\nabla\mu_{O_2}}{\left[\frac{\varepsilon_{SO}}{\tau_{SO}}\frac{Z_C}{2Z_e}(\sigma_V+\sigma_e)+\frac{\varepsilon_{MC}}{\tau_{MC}}\sigma_C\right]} \tag{4-48}$$

The flux of CO_2 should be $J_c/Z_c/F$, therefore, after some derivations,

$$N_C = -\frac{\varepsilon_{MC}}{\tau_{MC}}\frac{\sigma_C}{8F^2}\frac{2(\sigma_V+\sigma_e)\nabla\mu_{CO_2}+\sigma_e\nabla\mu_{O_2}}{\left[\frac{\varepsilon_{MC}}{\tau_{MC}}\frac{\tau_{SO}}{\varepsilon_{SO}}\sigma_C+(\sigma_V+\sigma_e)\right]} \tag{4-49}$$

The CO_2 flux is then obtained by integrating through the thickness of the membrane:

$$N_C = -\frac{\varepsilon_{MC}}{\tau_{MC}}\frac{\sigma_C}{8F^2}\int_{x_1}^{x_2}\frac{2(\sigma_V+\sigma_e)\nabla\mu_{CO_2}+\sigma_e\nabla\mu_{O_2}}{\left[\frac{\varepsilon_{MC}}{\tau_{MC}}\frac{\tau_{SO}}{\varepsilon_{SO}}\sigma_C+(\sigma_V+\sigma_e)\right]}dx \tag{4-50}$$

Assume that $\sigma_V << \sigma_e$,

$$N_C \approx -\frac{\varepsilon_{MC}}{\tau_{MC}}\frac{\sigma_C}{8F^2}\int_{x_1}^{x_2}\frac{2\nabla\mu_{CO_2}+\nabla\mu_{O_2}}{\left[\frac{\varepsilon_{MC}}{\tau_{MC}}\frac{\tau_{SO}}{\varepsilon_{SO}}\frac{\sigma_C}{\sigma_e}+1\right]}dx \tag{4-51}$$

Assume the integration could be done separately in the numerator and denominator without introducing large errors,

$$N_C \approx -\frac{\varepsilon_{MC}}{\tau_{MC}}\frac{\sigma_C}{8F^2}\frac{\left(2\Delta\mu_{CO_2}+\Delta\mu_{O_2}\right)}{L}\frac{1}{\int_{x_1}^{x_2}\left[\frac{\varepsilon_{MC}}{\tau_{MC}}\frac{\tau_{SO}}{\varepsilon_{SO}}\frac{\sigma_C}{\sigma_e}+1\right]dx} \tag{4-52}$$

Based on Eq. (4-46) and its simplified version Eq. (4-47), since the conductivities of electron and oxygen vacancy are functions of x coordinate, the integral could not be calculated analytically like Zhang did in her paper. Therefore, numerical solution is needed to get the accurate CO_2 flux.

4.4 DERIVATION OF MDC/LNO/MC MEMBRANE ANALYTICAL SOLUTION

For an MDC/LNO/MC membrane, oxygen vacancies, electrons and carbonate ions are transporting in MDC, LNO, and MC phases, respectively. Each phase is a single charge conducting material and are coupled at the surface. Both CO_2 and O_2 are permeating through the membrane.

First governing equation and boundary conditions in the solid oxide phase:

$$\nabla J_V = -\frac{(1-\varepsilon)}{\tau_{SO}}\sigma_V \nabla^2 \phi_{SO} = 0 \tag{4-53}$$

$$\phi_{SO} = \frac{RT\left(ln\frac{P_{CO_2,0}}{P^0}\frac{C^0}{C_V}\right) - \beta}{FZ_V} \tag{4-54}$$

$$J_V + J_C + J_{n,LNO} = 0 \tag{4-55}$$

Second equation and boundary conditions in the molten carbonate phase:

$$\nabla J_C = -\frac{\varepsilon}{\tau_{MC}}\sigma_C \nabla^2 \phi_{MC} = 0 \tag{4-56}$$

$$\phi_{MC}(x=0) = 0 \tag{4-57}$$

$$\phi_{MC} = \frac{RT\left(ln\frac{P_{CO_2,L}}{P^0}\frac{C^0}{C_V}\right) - \beta}{FZ_C} - \frac{Z_V \phi_{SO}}{Z_C} \tag{4-58}$$

Third governing equation and boundary conditions in the LNO phase:

$$\nabla J_{n,LNO} = -V_{LNO}\left(\sigma_{e,LNO}\nabla^2 \phi_{LNO}\right) = 0 \tag{4-59}$$

$$\phi_{LNO,0} = \frac{\chi}{2Z_eF} - \frac{RT}{2Z_eF} ln \frac{P_{CO_{2,0}}}{P^0} \left(\frac{P_{O_2,0}}{P^0}\right)^{0.5} \tag{4-60}$$

$$\phi_{LNO,L} = \frac{\chi}{2Z_eF} - \frac{RT}{2Z_eF} ln \frac{P_{CO_2,L}}{P^0} \left(\frac{P_{O_2,L}}{P^0}\right)^{0.5} + \frac{Z_C}{2Z_e} \phi_{MC,L} \tag{4-61}$$

Parameters:

$$\mu_{V,SO}{}^0 - \mu_{CO_2}{}^0 + \mu_C{}^0 - \mu_{O_O^x} = RT\, ln \frac{P_{CO_2}}{P^0} \frac{C^0}{C_V} - F(Z_C\phi_{MC} + Z_V\phi_{SO}) = \beta \tag{4-62}$$

$$RT\, ln \frac{P_{CO_2}}{P^0} \left(\frac{P_{O_2}}{P^0}\right)^{0.5} - F(Z_C\phi_{MC} - 2Z_e\phi_{LNO}) = \mu_C{}^0 - \mu_{CO_2}{}^0 - \frac{1}{2}\mu_{O_2}{}^0 - 2\mu_{e,LNO}{}^0 = \chi \tag{4-63}$$

$$\sigma_C = \frac{Z_C{}^2 F^2 D_C C_C}{RT} \tag{4-64}$$

$$\sigma_V = \frac{Z_V{}^2 F^2 D_V C_V}{RT} \tag{4-65}$$

Integration of equation (4-53), (4-54) and (4-55) with respect to x twice yield

$$\phi_{SO} = -\frac{C_1}{(1-\varepsilon)/\tau_{SO}\sigma_V} x - \frac{C_2}{(1-\varepsilon)/\tau_{SO}\sigma_V} \tag{4-66}$$

$$\phi_{MC} = -\frac{C_3}{\varepsilon/\tau_{MC}\sigma_C} x - \frac{C_4}{\varepsilon/\tau_{MC}\sigma_C} \tag{4-67}$$

$$\phi_{LNO} = -\frac{C_5}{V_{LNO}\sigma_{e,LNO}} x - \frac{C_6}{V_{LNO}\sigma_{e,LNO}} \tag{4-68}$$

Substitution of eq (4-57) into (4-67) results in C_4=0, then

$$\phi_{MC} = -\frac{C_3}{\varepsilon/\tau_{MC}\sigma_C} x \tag{4-69}$$

From Eq. (4-55), (4-66), (4-68) and (4-69),

$$C_3 = -C_1 - C_5 \tag{4-70}$$

Then, Eq. (4-69) becomes,

$$\phi_{MC} = \frac{C_1 + C_5}{\varepsilon/\tau_{MC}\sigma_C} x \tag{4-71}$$

According to Eq. (4-54) and (4-66),

$$C_2 = -\frac{(1-\varepsilon)/\tau_{SO}\sigma_V}{FZ_V}\left[RT\left(ln\frac{P_{CO_2,0}}{P^0}\frac{C^0}{C_V}\right) - \beta\right] \tag{4-72}$$

According to Eq. (4-58), (4-72), (4-71),

$$\frac{\varepsilon/\tau_{MC}\sigma_C RT\left(ln\frac{P_{CO_2,L}}{P_{CO_2,0}}\right)}{LFZ_C} - C_1\left(1 - \frac{Z_V}{Z_C}\frac{\varepsilon/\tau_{MC}\sigma_C}{(1-\varepsilon)/\tau_{SO}\sigma_V}\right) = C_5 \tag{4-73}$$

Substitution of Eq. (4-61) into Eq. (4-59) yields

$$C_6 = -V_{LNO}\sigma_{e,LNO}\left[\frac{\chi}{2Z_eF} - \frac{RT}{2Z_eF}ln\frac{P_{CO_2,0}}{P^0}\left(\frac{P_{O_2,0}}{P^0}\right)^{0.5}\right] \tag{4-74}$$

Substitution of Eq. (4-74), (4-73), (4-71) and (4-61) into Eq. (4-59) yields

$$C_1 = \frac{\frac{RT}{2Z_eF}ln\left(\frac{P_{O_2,L}}{P_{O_2,0}}\right)^{0.5} - \frac{\varepsilon/\tau_{MC}\sigma_C}{V_{LNO}\sigma_{e,LNO}}\frac{RT}{FZ_C}\left(ln\frac{P_{CO_2,L}}{P_{CO_2,0}}\right)}{L\left\{\frac{Z_V}{2Z_e}\frac{1}{(1-\varepsilon)/\tau_{SO}\sigma_V} - \frac{1}{V_{LNO}\sigma_{e,LNO}}\left(1 - \frac{Z_V}{Z_C}\frac{\varepsilon/\tau_{MC}\sigma_C}{(1-\varepsilon)/\tau_{SO}\sigma_V}\right)\right\}} \tag{4-75}$$

The complete solutions are:

$$\emptyset_{SO} = -\frac{C_1}{(1-\varepsilon)/\tau_{SO}\sigma_V} x - \frac{C_2}{(1-\varepsilon)/\tau_{SO}\sigma_V} \tag{4-76}$$

$$\emptyset_{LNO} = -\frac{C_5}{V_{LNO}\sigma_{e,LNO}} x - \frac{C_6}{V_{LNO}\sigma_{e,LNO}} \tag{4-77}$$

$$\emptyset_{MC} = -\frac{C_3}{\varepsilon/\tau_{MC}\sigma_C} x \tag{4-78}$$

$$J_v = C_1 = \frac{\frac{RT}{2Z_eF} ln\left(\frac{P_{O_2,L}}{P_{O_2,0}}\right)^{0.5} - \frac{\varepsilon/\tau_{MC}\sigma_C}{V_{LNO}\sigma_{e,LNO}} \frac{RT}{FZ_C}\left(ln\frac{P_{CO_2,L}}{P_{CO_2,0}}\right)}{L\left\{\frac{Z_V}{2Z_e}\frac{1}{(1-\varepsilon)/\tau_{SO}\sigma_V} - \frac{1}{V_{LNO}\sigma_{e,LNO}}\left(1 - \frac{Z_V}{Z_C}\frac{\varepsilon/\tau_{MC}\sigma_C}{(1-\varepsilon)/\tau_{SO}\sigma_V}\right)\right\}} \quad (4\text{-}79)$$

$$J_C = C_3 = -J_V - J_{n,LNO} \quad (4\text{-}80)$$

$$J_{n,LNO} = C_5 = \frac{\varepsilon/\tau_{MC}\sigma_C RT\left(ln\frac{P_{CO_2,L}}{P_{CO_2,0}}\right)}{LFZ_C} - J_v\left(1 - \frac{Z_V}{Z_C}\frac{\varepsilon/\tau_{MC}\sigma_C}{(1-\varepsilon)/\tau_{SO}\sigma_V}\right) \quad (4\text{-}81)$$

4.5 CONCLUSION

For MOCC and MECC membranes, the analytical solutions could be derived directly by integrating the second-order Ohm's law twice and then implementing the boundary conditions to solve for the unknown parameters. We compared them with the published analytical solutions in the open literature in Chapter 5. However, we noticed that the analytical solution of CO_2 flux derived for a LSCF/MC (or MOECC) membrane is questionable since the concentrations (thus conductivity) of oxygen vacancy and electron nonlinearly vary across the thickness. Treating them as constants in the derivation process is inadequate. Because of such nonlinear concentration profiles (nonlinear PDEs), we were unable to derive analytical solutions using either the direct integration method shown in the literature. In Chapter 5, we will show the results of numerical solution for MOECC membranes.

CHAPTER 5

MATHEMATICAL MODELING OF HIGH-TEMPERATURE MULTIPHASE SOLID/MOLTEN CARBONATE MEMBRANES FOR CO_2 CAPTURE[2]

High-temperature solid/molten-carbonate composite represent an emerging class of CO_2 transport membranes to capture CO_2 from flue gas with advantages in flux density and selectivity over conventional solvent/sorbent- and polymer-based counterparts. While significant technical progress in these membranes has been made in the past years, a deeper fundamental understanding of CO_2 transport mechanisms is still limited. Aimed to bridge this gap, we here report a theoretical study on flux performances of four types of solid/molten-carbonate CO_2 transport membranes by analytical and numerical modeling. We found that analytical and numerical results are virtually identical for solids with single charge carrier. However, for mixed conducting solids, numerical methods are preferred since analytical methods cannot solve the nonlinear local concentrations of charge carriers.

---

[2] Xin Li, Kevin Huang, and Xinfang Jin, 2020. Journal of The Electrochemical Society. 167: 165412. Reprinted here with permission of the publisher.12/07/2020

Application of numerical method to a new three-phase membrane containing a mixed conducting solid, a pure electron conducting solid and molten-carbonate reveals a 75% increase in CO_2 flux compared to the two-phase (mixed conducting solid and molten-carbonate) counterpart. The models presented here are expected to provide better fundamental insights and guidance for designing next-generation high-performance CO_2 transport membranes.

5.1 INTRODUCTION

Stabilization of the current atmospheric CO_2 concentration to mitigate global warming and climate change requires effective and efficient CO_2 capture technologies to remove CO_2 from flue gas emitted by coal-fired and gas-fired power plants. The recently emerged high-temperature solid/molten-carbonate (MC) membranes based on the MC chemistry are a promising carbon capture technology for this purpose. This new class of membranes has fundamental advantages in CO_2 flux density, selectivity, energy efficiency and cost over the conventional solvent-/sorbent-based and polymeric membranes counterparts. The high operating temperature of solid/MC membranes is another unique advantage since it allows direct catalytic conversions of the captured CO_2 to valuable products within the same membrane reactor, thus simplifying the system design and practical operation. Since the first proof-of-concept stainless-steel/MC membrane was reported for CO_2 capture in 2005 [63], the solid phase has been expanded to oxide-ion (*e.g.* Y_2O_3-doped ZrO_2 (YSZ) [80] and Sm(Gd)-doped CeO_2 (SDC or GDC)) [78, 81], electron (silver [62, 77, 82-85] and $LiNiO_2$ (LNO)) [86] and mixed oxide-ion/electron conductors ($La_{1-x}Sr_xFe_{1-y}Co_yO_{3-\delta}$ (LSCF)) [87, 88] with much improved CO_2 flux density and durability [89, 90]. More importantly, in the presence of proper catalysts, these membranes

have been successfully demonstrated in laboratory-scale catalytic reactors to convert the capture CO_2 into syngas through dry (or dry-oxy) reforming of methane [21, 91] and into ethylene via oxidative dehydrogenation of ethane [92, 93] with unprecedented conversion and selectivity performance.

While the development of multiphase CO_2 transport membranes has progressed significantly in recent years, a comprehensive understanding of the CO2 transport mechanisms within multiphases is still limited. The early theoretical works [61, 63, 94, 95] primarily focused on applying traditional Wagner's equation [96] to solve ionic and electronic transport problems in individual phase to reach an analytical solution. In this approach, to solve for flux, the chemical potential gradient of charge carriers is not rigorously related to the chemical potential difference of neutral species through the equilibria at gas/solid and gas/liquid interfaces. In addition, to arrive at an analytical solution, the method always assumes that the transport number of the charge carrier is uniform across the membrane, which is not the case for mixed conducting solids. Therefore, the solution derived from this analytical method is only suitable for dual-phase membranes containing either a pure ionic or electronic solid phase, such as YSZ/MC and Ag/MC. If the solid is a mixed ionic/electronic conductor, the derivation of analytical solutions requires extra caution.

In the open literature, there have been multiple studies using Wagner's theory to derive the analytical solutions for CO_2 flux through solid/MC transport membranes [61, 63, 94]. However, inaccurate statements/derivations have been noted in these early studies. For example, Wade et al. [94] derived CO_2 flux equation from Wagner theory and concluded that the additional electronic conductivity under low oxygen atmosphere would never be

great enough to overwhelm the CO_2 transport. This statement is only true for n-type mixed conductors. For p-type mixed conductors, such as $La_{0.6}Sr_{0.4}Co_{0.4}Fe_{0.6}O_{3-\delta}$ (LSCF), with a dominant electron hole conductivity, CO_2 transport mechanism, thus flux equation, would be different. Rui et al. [61] derived an analytical solution for mixed conducting LSCF/MC membranes. The predicted improvement in CO_2 flux was attributed to the high hole conductivity of LSCF. However, the arrived analytical solution was not mathematically rigorous. Given the fact that there exists a large concentration gradient in oxygen vacancies and holes across the membrane, the partial conductivity of each charge carrier should be a function of location across the membrane. Direct substitution of the equilibrium boundary conditions into the bulk transport equation is, therefore, inadequate since these equilibria only hold on the boundaries. The authors also mistakenly related the oxygen gas permeation flux to the half of the oxygen vacancy flux [61], which should be a quarter of the electron flux.

In this work, we first demonstrate the general analytical solutions for CO_2 flux of dual-phase solid/MC membranes by solving the partial differential equations (PDEs) along with the boundary conditions. These analytical solutions are then compared with those derived directly from Wagner theory. We also develop numerical CO_2 flux solutions and compare them with the existing or our derived analytical solutions to point out the issues with using analytical methods to solve CO_2 flux in complex multiphase systems. Finally, we apply our numerical models to simulate CO_2 flux in more complex multiphase solid/MC membranes and reveal fundamental insights into the factors that dictate the membrane performance.

5.2 TYPES OF MEMBRANES MODELED

Throughout this paper, Kröger–Vink notation is used to describe ionic and electronic defects involved in the gas/solid interfacial reactions and bulk ionic/electronic transport. Therefore, oxygen vacancies, instead of oxide-ions, as the ionic charge carrier, are considered the active ionic defect in the solid-oxide phase; the electronic charge carrier could be free electron or electron hole, depending on the material.

As discussed in Chapter 4, there are 4 types of membranes: mixed oxygen-vacancy and carbonate-ion conducting (denoted as MOCC); mixed electron and carbonate-ion conducting (denoted as MECC); a mixed oxygen-vacancy and electron (or electron hole) conducting (MOEC) solid oxide (SO) phase mixed with the MC phase to form a membrane (denoted as MOECC); a third pure electron conducting (LNO) phase introduced into the MOECC membrane, which becomes a triple-phase membrane (denoted as MOEECC). We consider the surface reaction equilibria at multiphase interfaces, charge diffusion and migration transport driven by concentration gradient and potential gradient. There is no external current applied across the membrane.

5.3 MATHEMATICAL MODELS

The numerical solution was solved using the finite element software COMSOL Multiphysics version 5.4. This software was used to create one-dimensional models for the membrane in the thickness direction in Chapter 5 and two-dimensional models for the tubular membrane reactors in Chapter 6. For one-dimensional models, four different types of high temperature CO_2/O_2 co-transport membranes were studied. The electrical potential and concentration profile of each phase and the resulted flux of each species were

simulated. After validating the modeling results with experimental data, the MOEECC membrane was used to create a plug-flow membrane reactor for oxidative coupling of methane reaction. The reactor's performance was studied and compared with a an identical fixed-bed reactor with the same reactor bed and operating conditions. The steps of the model build-up process are shown in Figure 5.1.

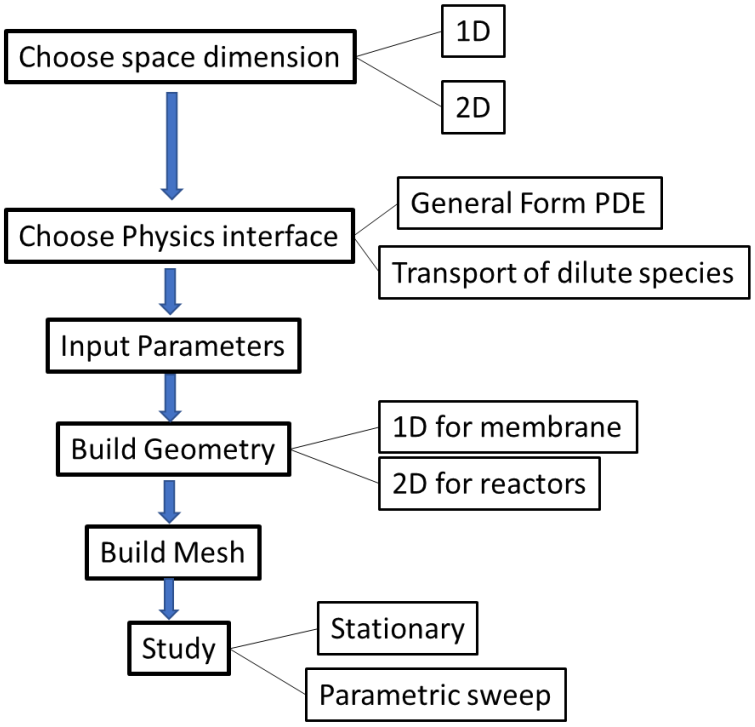

Figure 5.1 Steps of model build-up process

In a new COMSOL Multiphysics model, one should firstly select a component with appropriate dimensions, which should be either 1D (Chapter 5) or 2D (Chapter 6). Next, physics modules should be added to solve certain dependent variables, such as electric potential, concentration of charged species, species diffusion and convection in the gas phase. For the first two, we used 'General Form PDE' and 'Global ODE and DAEs' in COMSOL; for the last one, we used' transport of dilute species. Lastly, we added a stationary study or a parametric sweep as necessary in the model.

The next step was to specify the settings in the physics modules. For both 1-D and 2-D models, governing equations and boundary conditions should be implemented. Under "Physics" toolbar, "Add Physics/General form PDE" should be selected. In this case, thickness position x is the independent variables, the electrical potentials in MC phase(Φ_{MC}) and SO phase(Φ_{SO}) are the dependent variables. The governing equations and boundary conditions used in the 1D model was obtained from Wade's work. The derivation of analytical solution is shown in Chapter 4. In this model, the boundary conditions are specified along the boundaries of the domain, which include an essential boundary condition and a "Dirichlet boundary conditions.

To simulate the bulk CO_2 transport in each membrane, we assume that the chemical potential in the plane perpendicular to the thickness direction is uniform. All the models become, therefore, one-dimensional. The gas/solid/MC interface reactions are assumed to be fast compared to the bulk transport of charge carriers to ensure local equilibria. The mobility of each charge carrier is only a function of temperature, whereas the concentration varies with gas composition and temperature. The governing equations and boundary conditions for the above four types of membranes are given in Table 5.1. There are four types of phases considered: solid oxide (SO), molten carbonate (MC), mixed oxide-ion and electron conducting phase (MOEC), and metal. In the model, the membrane is exposed to the feed gas at x=0 and to the permeate (sweep) gas at x=L. The meaning of each variable is given in the Nomenclature section at the end of this paper. The focus of this work is to demonstrate the numerical and analytical methodologies with materials properties from the open literature. In the future work, we will validate the models by experimental data using optimization to extract materials/microstructural properties simultaneously.

In Table 5.1, the governing equations are either Ohm's law describing the migration of charge carriers or Nernst Planck equation explaining the diffusion and migration of charge carriers. The conductivity of a charge carrier is related to its diffusivity by Nernst-Einstein equation, see Table 5.3. The gas/solid/MC interface reaction is closely related to the charge carrier in each phase. Table 5.2 lists all the possible surface reactions involved in the four membranes. For MOCC membranes, reaction 1-1 occurs at both surfaces, whereas for MECC membranes, reaction 3-1 happens at both surfaces. For MOECC membranes, there will be two reactions occurring at the surfaces: 1) either reaction 2-1 or 2-2 depending on the type of the MOEC phase (n-type vs. p-type); 2) reaction 1-1. For MOEECC membranes, there are three reactions: 1) reaction 1-1; 2) reaction 2-1 or 2-2; 3) reaction 3-2. Combining reaction 2-1 and 1-1 leads to a similar reaction to 3-2 with the electron provided by MOEC phase, instead of LNO phase. To properly set up the boundary conditions for the equilibria of the reactions given in Table 5.2, lumped chemical potential needs to be defined for each reaction, which are listed in Table 5.3.

For MOCC and MECC membranes, the analytical solutions could be derived directly by integrating the second-order Ohm's law twice and then implementing the boundary conditions to solve for the unknown parameters. The final solutions to CO_2 flux equations are given in Table 5.4 with the derivation process provided in chapter 4. We compared them with the published analytical solutions in the open literature [61, 63, 94] and found general agreements for MOCC and MECC membranes. However, we noticed that all the pre-existing models in the open literature combined surface equilibria with charge conservation equations to solve for CO_2 flux, instead of solving PDEs as shown in this study. The problem for the surface equilibrium/charge conservation approach is that it

is only valid when the chemical potential distribution of the charge carrier is linear throughout the thickness. When there exists a nonlinearity in the concentration of charge carriers, this method needs to be carefully examined. For example, the analytical solution of CO_2 flux derived for a LSCF/MC (or MOECC) membrane [61] is questionable since the concentrations (thus conductivity) of oxygen vacancy and electron nonlinearly vary across the thickness. Treating them as constants in the derivation process is inadequate. Because of such nonlinear concentration profiles (nonlinear PDEs), we were unable to derive analytical solutions using either the direct integration method shown in the literature. In section 5.5.3, we will show the results of numerical solution for MOECC membranes.

Table 5.1 Governing equations and boundary conditions for different membranes

Membrane type		Oxygen vacancy conservation in SO phase	Molten carbonate ion conservation in MC phase	Electron/hole conservation in SO phase	Electron conservation in metal phase
MOCC	Governing Eq.	$\nabla \cdot J_V = -\frac{(1-\varepsilon)}{\tau_{SO}} \sigma_V \nabla^2 \phi_{SO} = 0$	$\nabla \cdot J_C = -\frac{\varepsilon}{\tau_{MC}} \sigma_C \nabla^2 \phi_{MC} = 0$	N/A	N/A
	B.C. X=0	$\phi_{SO} = \frac{RT\left(\ln \frac{P_{CO_2,0}}{P^0} \frac{C^0}{C_V}\right) - \beta}{FZ_V}$	$\phi_{MC}(x=0) = 0$		
	B.C. X=L	$J_V + J_C = 0$	$\phi_{MC} = \frac{RT\left(\ln \frac{P_{CO_2,L}}{P^0} \frac{C^0}{C_V}\right) - \beta}{FZ_C} - \frac{Z_V \phi_{SO}}{Z_C}$		
MECC	Governing Eq.	N/A	$\nabla J_C = -\frac{\varepsilon}{\tau_{MC}} \sigma_C \nabla^2 \phi_{MC} = 0$	N/A	$\nabla J_e = -\frac{(1-\varepsilon)}{\tau_m} \sigma_e \nabla^2 \phi_e = 0$
	B.C. X=0		$\phi_{MC}(x=0) = 0$		$\phi_e = \frac{\alpha}{2Z_e F} - \frac{RT}{2Z_e F} \ln \frac{P_{CO_2}}{P^0} \left(\frac{P_{O_2}}{P^0}\right)^{0.5}$
	B.C. X=L		$\phi_{MC} = -\frac{\alpha}{Z_C F} + \frac{RT}{Z_C F} \ln \frac{P_{CO_2,L}}{P^0} \left(\frac{P_{O_2,L}}{P^0}\right)^{0.5} + \frac{2Z_e}{Z_C} \phi_e$		$J_e + J_C = 0$
MOECC	Governing Eq.	$\nabla J_V = -\frac{(1-\varepsilon)}{\tau_{SO}} \left(Z_V F D_V \nabla^2 C_V + \frac{Z_V^2 F^2 D_V C_V}{RT} \nabla^2 \phi_{SO}\right) = 0$	$\nabla J_C = -\frac{\varepsilon}{\tau_{MC}} \sigma_C \nabla^2 \phi_{MC} = 0$	$\nabla J_n = -\frac{(1-\varepsilon)}{\tau_{SO}} \left(Z_n F D_n \nabla^2 C_n + \frac{Z_n^2 F^2 D_n C_n}{RT} \nabla^2 \phi_{SO}\right) = 0$	N/A
	B.C. X=0	$\phi_{SO,0} = \frac{RT\left(\ln \frac{P_{CO_2,0}}{P^0} \frac{C^0}{C_V}\right) - \beta}{FZ_V}$	$\phi_{MC}(x=0) = 0$	$C_n(0) = K_T^{1/2} C_V^{1/2} P_{O_2,0}^{1/2}$ $Z_V C_V + Z_n C_n + Z_D C_D = 0$	
	B.C. X=L	$J_V + J_n + J_C = 0$	$\phi_{MC,L} = \frac{RT\left(\ln \frac{P_{CO_2,L}}{P^0} \frac{C^0}{C_V}\right) - \beta}{FZ_C} - \frac{Z_V \phi_{SO,L}}{Z_C}$	$C_n(L) = K_T^{1/2} C_V^{1/2} P_{O_2,L}^{1/2}$ $Z_V C_V + Z_n C_n + Z_D C_D = 0$	
MOEECC	Governing Eq.	$\nabla J_V = -\frac{(1-\varepsilon)}{\tau_{SO}} \left(Z_V F D_V \nabla^2 C_V + \frac{Z_V^2 F^2 D_V C_V}{RT} \nabla^2 \phi_{SO}\right) = 0$	$\nabla J_C = -\frac{\varepsilon}{\tau_{MC}} \sigma_C \nabla^2 \phi_{MC} = 0$	$\nabla J_n = -\frac{(1-\varepsilon)}{\tau_{SO}} \left(Z_n F D_n \nabla^2 C_n + \frac{Z_n^2 F^2 D_n C_n}{RT} \nabla^2 \phi_{SO}\right) = 0$	$\nabla J_{e,LNO} = -V_{LNO}\left(\sigma_{e,LNO} \nabla^2 \phi_{LNO}\right) = 0$
	B.C. X=0	$\phi_{SO,0} = \frac{RT\left(\ln \frac{P_{CO_2,0}}{P^0} \frac{C^0}{C_V}\right) - \beta}{FZ_V}$	$\phi_{MC}(x=0) = 0$	$C_n(0) = K_T^{1/2} C_V^{1/2} P_{O_2,0}^{1/2}$ $Z_T C_T + Z_n C_n + Z_D C_D = 0$	$\phi_{LNO,0} = \frac{\chi}{2Z_e F} - \frac{RT}{2Z_e F} \ln \frac{P_{CO_2,0}}{P^0} \left(\frac{P_{O_2,0}}{P^0}\right)^{0.5}$
	B.C. X=L	$J_V + J_n + J_C + J_{n,L,NO} = 0$	$\phi_{MC,L} = \frac{RT\left(\ln \frac{P_{CO_2,L}}{P^0} \frac{C^0}{C_V}\right) - \beta}{FZ_C} - \frac{Z_V \phi_{SO,L}}{Z_C}$	$C_n(L) = K_T^{1/2} C_V^{1/2} P_{O_2,L}^{1/2}$ $Z_V C_V + Z_n C_n + Z_D C_D = 0$	$\phi_{LNO,L} = \frac{\chi}{2Z_e F} - \frac{RT}{2Z_e F} \ln \frac{P_{CO_2,L}}{P^0} \left(\frac{P_{O_2,L}}{P^0}\right)^{0.5} + \frac{Z_e}{2Z_e} \phi_{e,L}$

Table 5.2 Interfacial chemical reactions and equilibria

Reactions		Thermodynamic equilibrium
1-1	$CO_2 + O^x_{O(SO)} \leftrightarrow CO_3^{2-}{}_{(MC)} + V^{\cdot\cdot}_{O(SO)}$	$\mu_{CO_2} + RT\ln\frac{P_{CO_2}}{P^0} + \mu_{O_o^x} - \mu_C{}^0 - Z_C F\phi_{MC} - \mu_{V,SO}{}^0 - RT\ln\frac{C_V}{C^0} - Z_V F\phi_{SO} = 0$
2-1	$\frac{1}{2}O_2 + V^{\cdot\cdot}_{O(SO)} + 2e^-_{(SO)} \leftrightarrow O^x_{O(SO)}$	$\frac{1}{2}\mu_{O_2}{}^0 + \frac{1}{2}RT\ln\frac{P_{O_2}}{P^0} + \mu_V{}^0 + RT\ln\frac{C_V}{C^0} + Z_V F\phi_{SO} + 2\mu_{n,SO}{}^0 + 2RT\ln\frac{C_{n,SO}}{C^0} + 2Z_n F\phi_{SO} - \mu_{O_o^x} = 0$
2-2	$\frac{1}{2}O_2 + V^{\cdot\cdot}_{O(SO)} \leftrightarrow O^x_{O(SO)} + 2h^{\cdot}_{(SO)}$	$\frac{1}{2}\mu_{O_2}{}^0 + \frac{1}{2}RT\ln\frac{P_{O_2}}{P^0} + \mu_V{}^0 + RT\ln\frac{C_V}{C^0} + Z_V F\phi_{SO} - 2\mu_{h,SO}{}^0 - 2RT\ln\frac{C_{h,SO}}{C^0} - 2Z_h F\phi_{SO} - \mu_{O_o^x} = 0$
3-1	$CO_2 + \frac{1}{2}O_2 + 2e^-_{(metal)} \leftrightarrow CO_3^{2-}{}_{(MC)}$	$\mu_{CO_2} + \frac{1}{2}\mu_{O_2} - \mu_C{}^0 - Z_C F\phi_{MC} + 2\mu_{e,m}{}^0 + 2Z_e F\phi_{e,m} = 0$
3-2	$CO_2 + \frac{1}{2}O_2 + 2e^-_{(LNO)} \leftrightarrow CO_3^{2-}{}_{(MC)}$	$\mu_{CO_2} + \frac{1}{2}\mu_{O_2} - \mu_C{}^0 - Z_C F\phi_{MC} + 2\mu_{e,LNO}{}^0 + 2Z_e F\phi_{e,LNO} = 0$

Table 5.3 Parameter definitions

Parameters	Definition
Conductivity of carbonate ion	$\sigma_C = \frac{Z_C{}^2 F^2 D_C C_C}{RT}$
Conductivity of oxygen ion	$\sigma_V = \frac{Z_V{}^2 F^2 D_V C_V}{RT}$
Lumped chemical potential of reaction 1-1	$\beta = \mu_{V,SO}{}^0 - \mu_{CO_2}{}^0 + \mu_C{}^0 - \mu_{O_o^x}$
Lumped chemical potential of reaction 2-1	$\gamma = \mu_{O_o^x} - \frac{1}{2}\mu_{O_2}{}^0 - \mu_V{}^0 - 2\mu_{n,SO}{}^0$
Lumped chemical potential of reaction 2-2	$\xi = \mu_{O_o^x} - \frac{1}{2}\mu_{O_2}{}^0 - \mu_V{}^0 + 2\mu_{h,SO}{}^0$
Lumped chemical potential of reaction 3-1	$\alpha = \mu_C{}^0 - \mu_{CO_2}{}^0 - \frac{1}{2}\mu_{O_2}{}^0 - 2\mu_{e,m}{}^0$
Lumped chemical potential of reaction 3-2	$\chi = \mu_C{}^0 - \mu_{CO_2}{}^0 - \frac{1}{2}\mu_{O_2}{}^0 - 2\mu_{e,LNO}{}^0$

Table 5.4 Analytical solutions of carbonate-ion flux*

Case	Analytical Solution in this work	Analytical Solution from Literature	Ref
MOCC	$\phi_{MC}=\frac{x}{L}\frac{1}{FZ_C\left(1-\frac{Z_V}{Z_C}\frac{\varepsilon/\tau_{MC}\sigma_C}{(1-\varepsilon)/\tau_{SO}\sigma_V}\right)}RT\left(\ln\frac{P_{CO_2,L}}{P_{CO_2,0}}\right)$	Not Provided	[94]
	$\phi_{SO}=-\frac{x}{L}\frac{1}{FZ_C\left(\frac{(1-\varepsilon)/\tau_{SO}\sigma_V}{\varepsilon/\tau_{MC}\sigma_C}-\frac{Z_V}{Z_C}\right)}RT\left(\ln\frac{P_{CO_2,L}}{P_{CO_2,0}}\right)+\frac{1}{FZ_V}\left[RT\left(\ln\frac{P_{CO_2,0}}{P^0}\frac{C^0}{C_V}\right)-\beta\right]$		
	$N_C=\frac{J_C}{Z_CF}=\frac{1}{LZ_C}\frac{\varepsilon/\tau_{MC}Z_CD_CC_C(1-\varepsilon)/\tau_{SO}Z_VD_VC_V}{(\varepsilon/\tau_{MC}Z_CD_CC_C-(1-\varepsilon)/\tau_{SO}Z_VD_VC_V)}\left(\ln\frac{P_{CO_2,L}}{P_{CO_2,0}}\right)$ $N_C=\frac{RT}{LZ_CF^2}\frac{\varepsilon/\tau_{MC}\sigma_C(1-\varepsilon)/\tau_{SO}\sigma_V}{(\varepsilon/\tau_{MC}\sigma_CZ_V-(1-\varepsilon)/\tau_{SO}\sigma_VZ_C)}\left(\ln\frac{P_{CO_2,L}}{P_{CO_2,0}}\right)$	$N_C=\frac{1}{LZ_C}\frac{\varepsilon/\tau_{MC}Z_CD_CC_C(1-\varepsilon)/\tau_{SO}Z_VD_VC_V}{(\varepsilon/\tau_{MC}Z_CD_CC_C-(1-\varepsilon)/\tau_{SO}Z_VD_VC_V)}\left(\ln\frac{P_{CO_2,L}}{P_{CO_2,0}}\right)$ $N_C=\frac{1}{LZ_C}\frac{\varepsilon/\tau_{MC}\sigma_C(1-\varepsilon)/\tau_{SO}\sigma_V}{(\varepsilon/\tau_{MC}\sigma_CZ_V-(1-\varepsilon)/\tau_{SO}\sigma_VZ_C)}\frac{RT}{F^2}\left(\ln\frac{P_{CO_2,L}}{P_{CO_2,0}}\right)$	
	$N_V=\frac{J_V}{Z_VF}=-\frac{J_C}{Z_VF}=-\frac{1}{L}\frac{\varepsilon/\tau_{MC}Z_CD_CC_C(1-\varepsilon)/\tau_{SO}D_VC_V}{(\varepsilon/\tau_{MC}Z_CD_CC_C-(1-\varepsilon)/\tau_{SO}Z_VD_VC_V)}\left(\ln\frac{P_{CO_2,L}}{P_{CO_2,0}}\right)$ $N_V=-\frac{RT}{LZ_VF^2}\frac{\varepsilon/\tau_{MC}\sigma_C(1-\varepsilon)/\tau_{SO}\sigma_V}{(\varepsilon/\tau_{MC}\sigma_CZ_V-(1-\varepsilon)/\tau_{SO}\sigma_VZ_C)}\left(\ln\frac{P_{CO_2,L}}{P_{CO_2,0}}\right)$	Not Provided	
MECC	$\phi_{MC}=\frac{x}{L}\frac{1}{\left(1+\frac{2Z_e}{Z_C}\frac{\varepsilon/\tau_{MC}\sigma_C}{(1-\varepsilon)/\tau_m\sigma_e}\right)}\frac{RT}{Z_CF}\ln\frac{P_{CO_2,L}}{P_{CO_2,0}}\left(\frac{P_{O_2,L}}{P_{O_2,0}}\right)^{0.5}$	Not Provided	[63]
	$\phi_{e,m}=-\frac{x}{L}\frac{\frac{RT}{Z_CF}\ln\frac{P_{CO_2,L}}{P_{CO_2,0}}\left(\frac{P_{O_2,L}}{P_{O_2,0}}\right)^{0.5}}{\left(\frac{(1-\varepsilon)/\tau_m\sigma_e}{\varepsilon/\tau_{MC}\sigma_C}+\frac{2Z_e}{Z_C}\right)}+\frac{\alpha}{2Z_eF}-\frac{RT}{2Z_eF}\ln\frac{P_{CO_2,0}}{P^0}\left(\frac{P_{O_2,0}}{P^0}\right)^{0.5}$		
	$N_C=-\frac{1}{Z_CL}\frac{\varepsilon/\tau_{MC}\sigma_C(1-\varepsilon)/\tau_m\sigma_e}{(Z_C(1-\varepsilon)/\tau_m\sigma_e+2Z_e\varepsilon/\tau_{MC}\sigma_C)}\frac{RT}{F^2}\ln\frac{P_{CO_2,L}}{P_{CO_2,0}}\left(\frac{P_{O_2,L}}{P_{O_2,0}}\right)^{0.5}$	$N_C=-\frac{1}{4}\frac{\varepsilon/\tau_{MC}\sigma_C(1-\varepsilon)/\tau_m\sigma_e}{((1-\varepsilon)/\tau_m\sigma_e+\varepsilon/\tau_{MC}\sigma_C)F^2}\frac{RT}{L}\ln\frac{P_{CO_2,L}}{P_{CO_2,0}}\left(\frac{P_{O_2,L}}{P_{O_2,0}}\right)^{0.5}$	

	$N_e = \frac{1}{Z_e L}\frac{\varepsilon/\tau_{MC}\sigma_C(1-\varepsilon)/\tau_m\sigma_e}{\left(Z_C(1-\varepsilon)/\tau_m\sigma_e + 2Z_e\varepsilon/\tau_{MC}\sigma_C\right)}\frac{RT}{F^2}\ln\frac{P_{CO_2,L}}{P_{CO_2,0}}\left(\frac{P_{O_2,L}}{P_{O_2,0}}\right)^{0.5}$	Not Provided	
MOECC	Not available	$N_C = -\frac{\varepsilon/\tau_{MC}C_C D_C\left(+\frac{1}{2}\sigma_n\nabla\mu_{O_2} + (\sigma_V+\sigma_n)\nabla\mu_{CO_2}\right)}{\left(RT(\sigma_V+\sigma_n) + \frac{\varepsilon/\tau_{MC}}{(1-\varepsilon)/\tau_{SO}}2Z_nZ_CF^2D_CC_C\right)}$ with electron as the electronic charge $N_C = -\frac{\varepsilon/\tau_{MC}C_C D_C\left(+\frac{1}{2}\sigma_h\nabla\mu_{O_2} + (\sigma_V+\sigma_h)\nabla\mu_{CO_2}\right)}{\left(RT(\sigma_V+\sigma_h) - \frac{\varepsilon/\tau_{MC}}{(1-\varepsilon)/\tau_{SO}}2Z_hZ_CF^2D_CC_C\right)}$ with electron hole as the electronic charge	[61]
	Not available	$N_{O_2} = \frac{(1-\varepsilon)/\tau_{SO}\sigma_V}{2Z_V^2F^2}\left(\nabla\mu_{CO_2} + Z_VF\frac{-\frac{\varepsilon/\tau_{MC}}{(1-\varepsilon)/\tau_{SO}}Z_CFD_CC_C/RT\nabla\mu_{CO_2} + \left(\frac{1}{2Z_nF}(\sigma_V+\sigma_n) + \frac{\varepsilon/\tau_{MC}}{(1-\varepsilon)/\tau_{SO}}Z_CFD_CC_C/RT\right)\nabla\mu_{CO_2} + \frac{1}{4Z_nF}\sigma_n\nabla\mu_{O_2}}{\left((\sigma_V+\sigma_n) + \frac{\varepsilon/\tau_{MC}}{(1-\varepsilon)/\tau_{SO}}2Z_nZ_CF^2D_CC_C/RT\right)}\right)$ With electron as the electronic charge $N_{O_2} = \frac{(1-\varepsilon)/\tau_{SO}\sigma_V}{2Z_V^2F^2}\left(\nabla\mu_V + Z_VF\frac{\left(-\frac{\varepsilon/\tau_{MC}}{(1-\varepsilon)/\tau_{SO}}Z_CFD_CC_C/RT\right)(\nabla\mu_{CO_2}) + \left(-\frac{1}{2Z_hF}(\sigma_V+\sigma_h) + \frac{\varepsilon/\tau_{MC}}{(1-\varepsilon)/\tau_{SO}}Z_CFD_CC_C/RT\right)(\nabla\mu_V) - \frac{1}{4Z_hF}\sigma_h\nabla\mu_{O_2}}{(\sigma_V+\sigma_h) - \frac{\varepsilon/\tau_{MC}}{(1-\varepsilon)/\tau_{SO}}2Z_hZ_CF^2D_CC_C/RT}\right)$ With electron hole as the electronic charge	
***** MOECC (GDC/LNO/MC)** [17]	$\phi_{SO} = -\frac{C_1}{(1-\varepsilon)/\tau_{SO}\sigma_V}x - \frac{C_2}{(1-\varepsilon)/\tau_{SO}\sigma_V}$ $C_2 = -\frac{(1-\varepsilon)/\tau_{SO}\sigma_V}{FZ_V}\left[RT\left(\ln\frac{P_{CO_2,0}}{P^0}\frac{C^0}{C_V}\right) - \beta\right]$	Not available	-
	$\phi_{MC} = -\frac{C_3}{\varepsilon/\tau_{MC}\sigma_C}x$		
	$\phi_{LNO} = -\frac{C_5}{V_{LNO}\sigma_{e,LNO}}x - \frac{C_6}{V_{LNO}\sigma_{e,LNO}}$		

	$C_6 = -V_{LNO}\sigma_{e,LNO}\left[\frac{\chi}{2Z_eF} - \frac{RT}{2Z_eF}\ln\frac{P_{CO_2,0}}{P^0}\left(\frac{P_{O_2,0}}{P^0}\right)^{0.5}\right]$		
	$J_v = C_1 = \frac{\frac{RT}{2Z_eF}\ln\left(\frac{P_{O_2,L}}{P_{O_2,0}}\right)^{0.5} - \frac{\varepsilon/\tau_{MC}\sigma_C}{V_{LNO}\sigma_{e,LNO}}\frac{RT}{FZ_C}\left(\ln\frac{P_{CO_2,L}}{P_{CO_2,0}}\right)}{L\left\{\frac{Z_V}{2Z_e}\frac{1}{(1-\varepsilon)/\tau_{SO}\sigma_V} - \frac{1}{V_{LNO}\sigma_{e,LNO}}\left(1-\frac{Z_V}{Z_C}\frac{\varepsilon/\tau_{MC}\sigma_C}{(1-\varepsilon)/\tau_{SO}\sigma_V}\right)\right\}}$		
	$J_C = C_3 = -J_V - J_{n,LNO}$		
	$J_{n,LNO} = C_5 = \frac{\varepsilon/\tau_{MC}\sigma_C RT\left(\ln\frac{P_{CO_2,L}}{P_{CO_2,0}}\right)}{LFZ_C} - J_v\left(1-\frac{Z_V}{Z_C}\frac{\varepsilon/\tau_{MC}\sigma_C}{(1-\varepsilon)/\tau_{SO}\sigma_V}\right)$		

Note: * Derivation of the analytical solutions are provided in ESI A, B and C; the number of charges associated with oxygen vacancy, electron, electron hole and carbonate ion are: Z_V=+2, Z_n=-1; Z_h=+1; Z_C=-2.

** C1, C2, C3, C5, and C6 are constants used in the solving process. Details could be found in the ESI C.

*** Analytical solution is only achievable for MOEECC membrane consisting of GDC/LNO/MC.

5.4 MATERIALS PROPERTY DATA

The materials properties are of critical importance to ensure the fidelity of a model. In this study, we adopted all the parameters from experimental data published in the open literature; they are listed in Table 5.5. The materials include 8% Y_2O_3 stabilized ZrO_2 (denoted as 8YSZ) and 20mol% Gd_2O_3-doped ceria oxide (denoted as GDC20), 10% Mn-doped ceria oxide (denoted as MDC) and lanthanum strontium cobalt ferrite perovskite (denoted as LSCF 6446) as MOEC, 52mol% Li_2CO_3-48mol% Na_2CO_3 eutectic as molten carbonate (denoted as MC), $Li_{1-x}Ni_{1+x}O_2$ (denoted as LNO) and silver (denoted as Ag) as the pure electronic conduction phase.

Table 5.5 Materials properties under different gas compositions/temperatures

Material	Properties	Correlation	Ref.
8YSZ	Conductivity (S/cm) vs T (K)	$\log_{10}(\sigma T) = 6.54509 - 5.46453 \cdot \frac{1000}{T}$	[97]
LSCF6446	Oxygen vacancy fraction vs p_{O_2} (atm)	$3-\delta = 2.98941 + 0.03445 \cdot \log 10(p_{O_2})$, 1073K $3-\delta = 3.01635 + 0.03128 \cdot \log 10(p_{O_2})$, 973K $3-\delta = 3.03491 + 0.02717 \cdot \log 10(p_{O_2})$, 873K	[98]
	Electron hole fraction	$p = [Sr'_{La}] - 2\delta$	-
GDC20	Oxygen vacancy fraction vs T(K), p_{O_2} (atm)	$\delta = \frac{9100}{\sqrt{[Gd'_{Ce}]}} \exp\left\{\frac{-220000}{RT}\right\} p_{O_2}^{-1/4} + \frac{[Gd'_{Ce}]}{2}$	[99]
	Electron fraction	$n = 2\delta - [Gd'_{ce}]$	[99]
	Oxygen vacancy mobility ($cm^2/V/s$) vs T(K)	$\log_{10}(\mu_{i,10} T) = 2.4656 - 3.40416 \cdot \frac{1000}{T}$ $\log_{10}(\mu_{i,20} T) = 2.36515 - 3.56931 \cdot \frac{1000}{T}$	[100]
	Electron mobility ($cm^2/V/s$) vs T(K)	$\log_{10}(\mu_{e,10} T) = 4.1943 - 4.30072 \cdot \frac{1000}{T}$ $\log_{10}(\mu_{e,20} T) = 2.63204 - 2.6264 \cdot \frac{1000}{T}$	[100]
	Diffusivity (cm^2/s)	$D_i = \frac{\mu_i RT}{F}$	-
	Conductivity (S/cm)	$\sigma_i = \frac{Z_i^2 F^2 D_i C_i}{RT} = Z_i^2 F \mu_i C_i$	-

	Fraction to molar volume concentration (mol/m^3)	$c_i = \frac{\delta}{V_m}$ $V_m = \frac{a^3 \cdot Na}{NA}$, molar volume, (m^3/mol) Na, Avagadro's number. NA, number of cation atoms in a unit cell.	-
MDC	Oxygen vacancy fraction vs T(K), p_{O_2} (atm)	$\delta = \left[Mn_{Ce}^{2-}\right] - 0.003\log_{10} p_{O_2}$	[101]
	Electron fraction	$n = 2\left(\delta - \left[Mn_{Ce}^{2-}\right]\right)$	[102, 103]
MC	Conductivity (S/cm) vs T (K)	$\sigma = -4.6866 + 8.533\cdot10^{-3}\cdot T - 1.325\cdot10^{-6}\cdot T^2$	[104]
LNO	Conductivity (S/cm) vs T (K)	$\ln\sigma = 1.9846 - \frac{1211.4}{T}$	[105]
Ag	Resistivity (Ω·m) vs T (K)	$\rho = 7\cdot10^{-11}\cdot T^{-5}\cdot10^{-9}$	[106]

For comparison purpose, Figure 5.2 compiles the conductivity of each material considered and groups them into three categories according to their magnitudes: 1) Ag with conductivity on the order of 10^7 S/m; 2) MC, LNO and LSCF with a conductivity on the order of 100 S/m; 3) GDC, MDC and YSZ with conductivity on the order of 10 S/m.

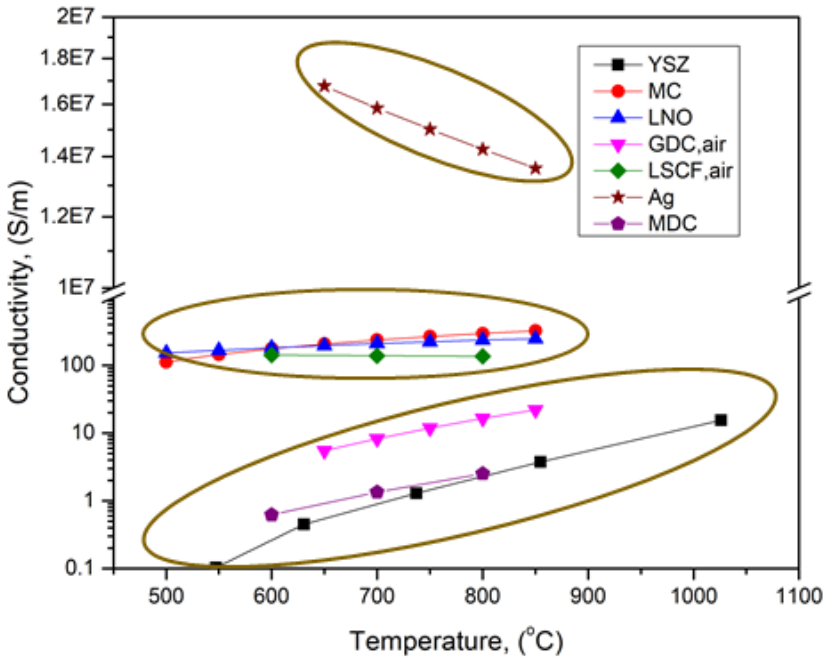

Figure 5.2 Total conductivity comparison among different materials

Operating temperature, gas composition, membrane thickness, porosity and tortuosity are kept the same for all case simulations to ensure a fair comparison; they are listed in Table 5.6. The baseline operating condition is defined as temperature: 800^{o}C, feed gas: 50% CO_2; sweep gas: 0.1%CO_2. If there is O_2 in the feed gas, the ratio of CO_2:O_2 ratio is kept at 2:1. In the parametric studies, temperature is varied between 650 and 850^{o}C, and pCO_2 at permeate-side is changed from 0.02 to 0.25atm. The third electronic LNO phase in MOEECC membrane is assumed to count for 0.5% of the total volume.

Table 5.6 Operating conditions and membrane parameter

Parameter	Value	Unit	Description
T	650-850	^{o}C	Temperature
$pCO_{2,0}$	0.5	atm	CO_2 partial pressure at feed side, x=0
$pCO_{2,L}$	0.02-0.25	atm	CO_2 partial pressure at permeate side, x=L
$pO_{2,0}$	0.25	atm	O_2 partial pressure at feed side, x=0
$pO_{2,L}$	0.01-0.125	atm	O_2 partial pressure at permeate side, x=L
L	0.5	mm	Membrane thickness
ε	0.5	1	Volume fraction of molten carbonate
τ	2	1	Tortuosity of the membrane
V_{LNO}	0.005	1	Volume fraction of LNO phase
Feed gas	50% CO_2: 25% O_2:25% N_2	-	Feed gas composition
Sweep gas	99.85% Ar:0.1%CO_2: 0.05%O_2	-	Sweep gas composition

Note: Tortuosity is assumed to be the same in all the phases.

5.5 RESULTS AND DISCUSSION

All the governing equations listed in Table 4.1 are solved in multiphysics software COMSOL 5.4. The computational domain is a 1D film spanning from 0 to L within which transport of multiple species (oxygen-vacancy, carbonate-ion, electron, or hole) and chemical reactions at gas/solid interface take place (see Table 5.2). The mesh is symmetrically distributed with dense grids at the two boundaries. Arithmetic sequence

growth formula is used to control the element ratio to be 10. A stationary solver is used to solve all the equations in the models. Meanwhile, the analytical solutions derived in this work, as given in Table 5.4, are also calculated in the corresponding COMSOL modules for comparison purposes.

In this section, we demonstrate analytical and numerical solutions of CO_2 flux for all the four types of membranes shown in Figure 4.1 as a function of T and pCO_2 at the permeate-side. The CO_2:O_2 ratio at the feed-side is kept at 2:1, see Table 6. For the first time, electrical potential profiles are correlated with CO_2 flux under different conditions, which is informative because the driving force for the CO_2 transport through a mixed conducting membrane is the electrochemical potential gradient that is the summation of chemical potential and static electric potential. The numerical solutions for MOCC and MECC membranes are also compared with their analytical counterparts. The numerical solution for MOECC membranes is compared to the existing analytical solution and the cause of discrepancy is discussed. Most importantly, the numerical solution for MOEECC membranes offers the evidence that the additional electronic conducting LNO phase can significantly enhance the CO_2 flux.

5.5.1 MOCC

For MOCC membranes, both SO phase and MC phase transport one single charge carrier, viz. oxygen vacancy and carbonate ion, respectively. Here, we simulate the two most popular SO materials: 8YSZ and GDC20. The performances of the two membranes are compared in terms of CO_2 flux.

5.5.1.1 YSZ/MC

Here, we select 8YSZ, a pure oxygen vacancy conductor, as the SO phase, and Li-Na eutectic, a pure carbonate ion conductor, as the MC phase, for the modeling. Figure 5.2 and 5.3 show CO_2 flux and electric potential in both MC and SO phases in the x (thickness) direction against temperature and permeate-side pCO_2, respectively. The solid lines and symbols represent data calculated from numerical and analytical methods, respectively. Evidently, the numerical and analytical results agree seamlessly. Figure 5.2a shows that the CO_2 flux increases nonlinearly from 1.0×10^{-8} to 9.0×10^{-8} mol/cm^2/s as temperature increases from 650 to 850^{o}C. This temperature-related increase in CO_2 flux is the result of increased ionic conductivity in MC and 8YSZ phases. Since the conductivity in MC is much higher than 8YSZ, see Figure 5.3, the electric potential gradient in the MC phase is much smaller than that in 8YSZ phase. For example, Figure 5.2b and 5.2c show that the variation of transmembrane electrical potential is $\Delta\phi_{MC}$~1.2 mV for MC phase under 850^{o}C, whereas it is $\Delta\phi_{SO}$ ~ 80 mV for 8YSZ phase. The change of temperature does not significantly change the transmembrane gradient of ϕ_{SO}, thus the flux enhancement is mainly resulted from its conductivity dependence on temperature; whereas the range of ϕ_{MC} does change considerably with temperature, implying that the flux enhancement by the conductivity of 8YSZ is more pronounced than that brought by the conductivity of MC phase. Overall, the conductivity of 8YSZ phase is a factor limiting the CO_2 flux. This assertion is also supported by the measurement of the effective conductivity of a MOCC membrane [107].

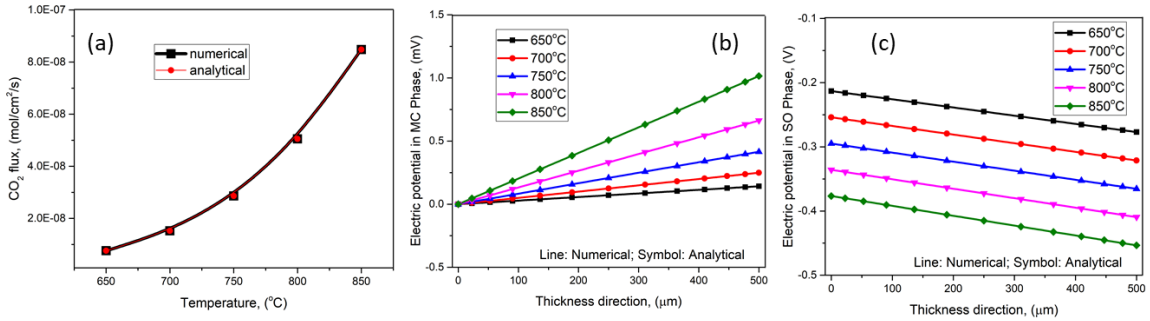

Figure 5.3 Numerical and analytical results of MOCC membrane at different temperatures with a fixed permeate-side pCO_2=0.1 atm:(a) CO_2 flux; (b) electric potential in MC phase; (c) electric potential in SO (8YSZ) phase

Figure 5.4 shows the same set of plots but with the permeate-side pCO_2 as a variable at a fixed T=800 °C. As expected, Figure 5.3a shows that the lower the permeate-side pCO_2, the higher the resultant CO_2 flux. From the mathematical point of view, change of permeate-side pCO_2 leads to a change in boundary conditions, thus in the chemical potential gradient. Correspondingly, Figure 5.3b and 5.3c show that the lower the permeate-side pCO_2, the greater the slope (gradient of electric potential). Hence, lower permeate-side pCO_2 is beneficial to improve the CO_2 flux, which is increased by nearly 5 times as pCO_2 decreases from 0.25 to 0.02 atm. This revelation also suggests that instant consumption of permeated CO_2 via a chemical conversion process such as reverse water-gas shift reaction can promote the transmembrane CO_2 flux.

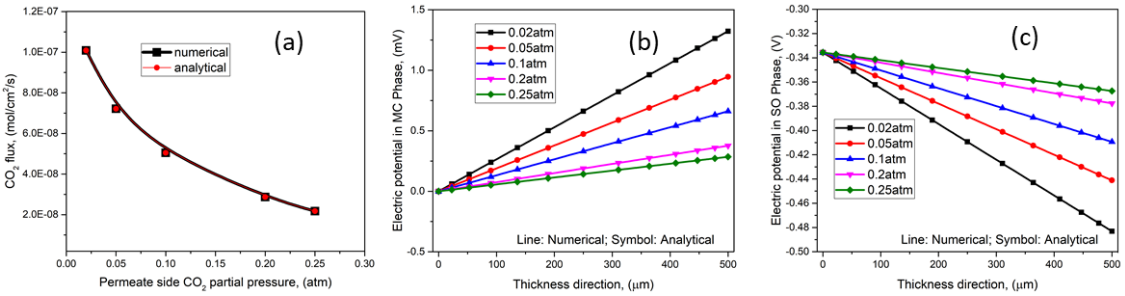

Figure 5.4 Numerical and analytical results of MOCC membrane under different permeate-site pCO_2 at a fixed T=800°C: (a) CO_2 flux; (b) electric potential in MC phase; (c) electric potential in SO (8YSZ) phase

5.5.1.2 MOCC: GDC/MC

In this modeling, YSZ phase is replaced by GDC, another oxide-ion conductor, to examine how oxide-ion conductivity affects the transmembrane CO_2 flux.

Figure 5.5 compares the calculated CO_2 flux for two membranes: YSZ/MC vs GDC/MC. It is evident that CO_2 flux of GDC/MC (red curve) is 4-9 times higher than that of YSZ/MC (red curve) in the temperature range of 650 and 850^{o}C, and 6-7 times higher in the permeate-side pCO_2 range of 0.02 and 0.25 atm. Therefore, replacing YSZ by GDC or a SO material with higher ionic conductivity in MOCC membranes should significantly improve the CO_2 flux.

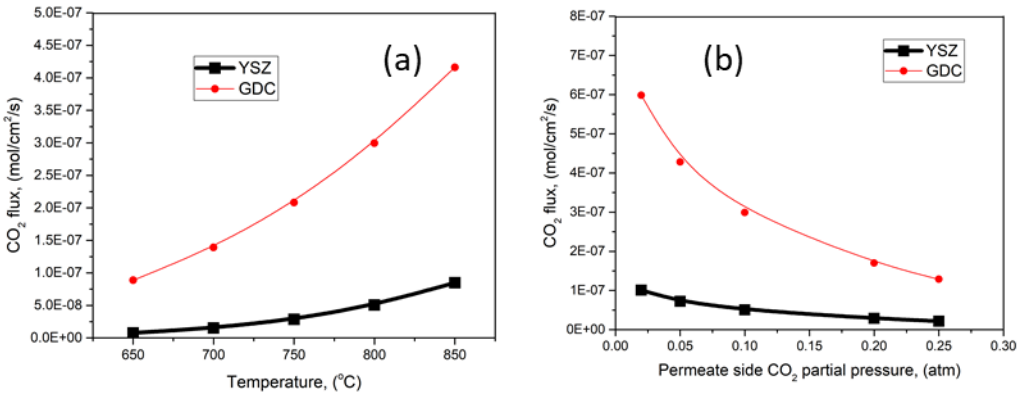

Figure 5.5 CO_2 flux(mol/cm^2/s), comparison between YSZ/MC and GDC/MC membranes;(a) different operating temperature, (^{o}C) with a fixed permeate-side pCO_2=0.1 atm; (b) different permeate-side CO_2 partial pressures, (atm) with a fixed T=800^{o}C

5.5.2 MECC: Ag/MC

For MECC membranes, silver is selected as the metal phase due to its high electrical conductivity and chemical inertness to MC. We built the MECC model using the governing equations in Table 5.1 and parameters in Table 5 to simulate CO_2 flux. Figures 5.5 and 5.6 show the numerical (solid lines) and analytical (symbols) results against T and permeate-site pCO_2, respectively. Different from MOCC membranes, both CO_2 and O_2 permeate, at

a flux ratio of CO_2:O_2=2:1, according to the reaction 3-1 in Table 5.2. Such a correlation is indeed confirmed in Figure 5.6a and 5.7a. Remarkably, the results produced from the two modeling methods are in excellent agreement.

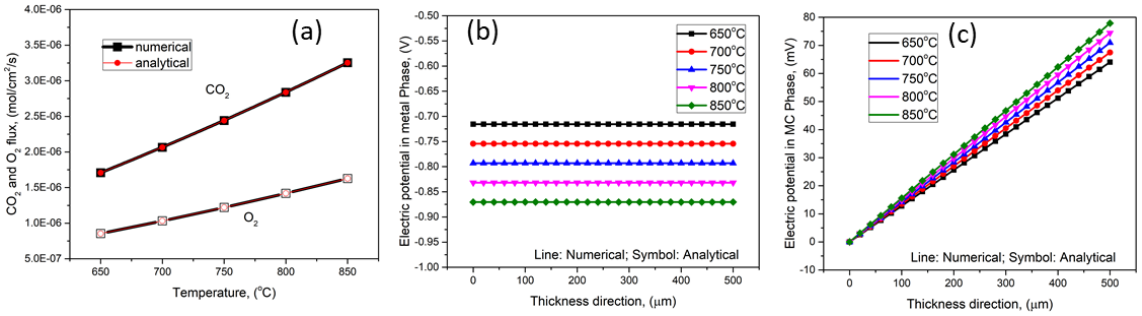

Figure 5.6 Numerical and analytical results of MECC (Ag/MC) membrane at different temperatures with a fixed permeate-side pCO_2=0.1atm: (a) CO_2 and O_2 flux; (b) electric potential in metal (Ag) phase; (c) electric potential in MC phase

Compared to the MOCC counterpart shown in Figure 5.2a, the CO_2 flux of Ag/MC membrane shown in Figure 5.5a is much higher, varying from 1.75×10^{-6} to 3.25×10^{-6} mol/cm^2/s at 650 to 850°C. Since the conductivity of silver is much higher than that of MC, the carbonate-ion transport in MC phase becomes the rate-limiting factor to CO_2 flux. Figure 5.5b and 5.5c further confirm this point by showing that the electrical potential in metal phase ϕ_e merely changes in the x direction at a given T but its absolute value increases with T, while ϕ_{MC} gradient increases with T, leading to a higher CO_2 flux.

Figure 5.7 further shows the same set of figures plotted under different permeate-side pCO_2 at T=800°C. The CO_2 flux nonlinearly increases from 1.22×10^{-6} to 5.67×10^{-6} mol/cm^2/s as the permeate-side pCO_2 decreases from 0.25 to 0.02 atm, see Figure 5.6a. A steeper slope (gradient of electric potential) is observed in Figure 5.6b and 5.6c for both metal and MC phases when the permeate-side pCO_2 decreases, which leads to a higher CO_2 flux. As expected from the high electrical conductivity, the variation of transmembrane

electric potential in the metal phase is much lower than the MC phase, $\Delta\phi_e$=0.5 mV vs. $\Delta\phi_{MC}$=150 mV. Overall, because of the much higher ionic conductivity of the transport-limiting MC phase in MECC membranes than that of SO phase in MOCC membranes, the former shows a much higher CO_2 flux than the latter under the same operating conditions.

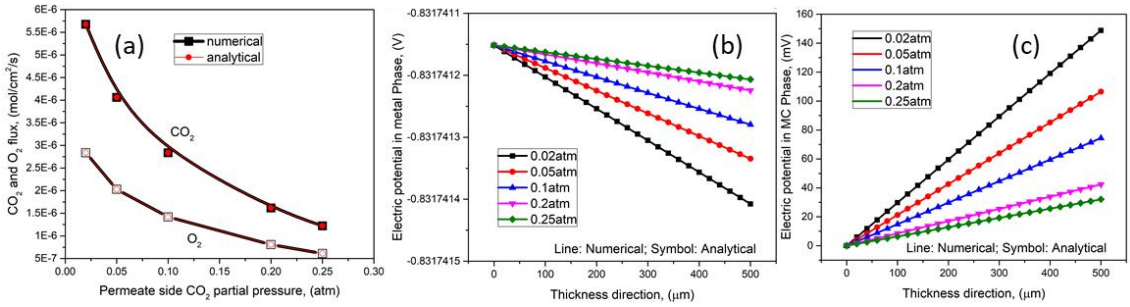

Figure 5.7 Numerical and analytical results of MECC membrane under different permeate-site pCO_2 at a fixed T=800°C: (a) CO_2 flux; (b) electric potential in metal phase; (c) electric potential in MC phase

5.5.3 MOECC: LSCF/MC

In this section, the pure ionic conducting YSZ phase is replaced by a MOEC: LSCF phase. The objective is to show how electronic component in the solid phase affects the total CO_2 and O_2 fluxes. The chemistries of such a MOECC membrane are illustrated in Figure 4.1c. Figure 5.8 shows profiles of electron-hole and oxygen-vacancy concentration along the thickness direction. A strong nonlinearity and opposite trending are observed for both charge carriers. The lower the pCO_2 the more pronounced the variation. Such a correlation is mainly dictated by the equilibrium of reaction 2-2 in Table 5.2.

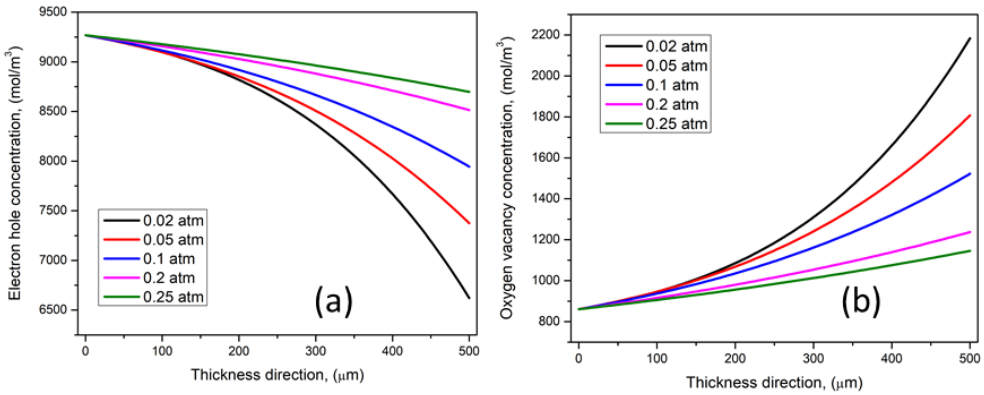

Figure 5.8 Transmembrane concentration profiles of electron holes and oxygen vacancies in LSCF/MC membrane under different permeate-side pCO_2 and a fixed T=800°C: (a) electron holes; (b) oxygen vacancies

Figure 5.9 compares the numerical (solid lines) and analytical (symbols) results obtained from literature [61] in fluxes of O_2, oxygen-vacancy and CO_2. Clearly, O_2, oxygen vacancy and CO_2 fluxes of the analytical solution show nonlinear variations across the membrane, which are contradicted to those calculated constant fluxes from the numerical method. The difference is rooted in the fact that the variations of oxygen vacancy and hole concentration are nonlinear across the membrane, see Figure 5.8. Unfortunately, the analytical method cannot solve this nonlinearity. The analytical results provided by ref. [20] are wrong for the reason explained above. Therefore, for more complex MOECC membranes, the numerical method is a better approach to calculating the flux. The constant flux profiles vs. membrane thickness by numerical method is consistent with the governing equation (gradient of flux equals 0 in the bulk) in Table 5.1.

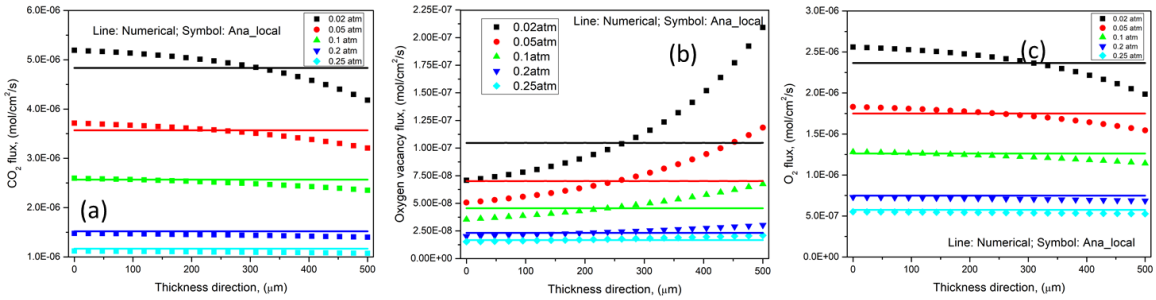

Figure 5.9 Comparison of transmembrane fluxes of LSCF/MC membrane under different permeate-side pCO_2 and a fixed T=800°C derived from numerical and analytical methods: (a) O_2 flux; (b) oxygen vacancy flux; (c) CO_2 flux

Figure 5.10 further compares CO_2, oxygen vacancy and O_2 fluxes vs. permeate-side pCO_2 derived from numerical and analytical methods. N_{CO2}, N_v and N_{O2} are molar fluxes of CO_2, oxygen vacancy and O_2 across the membrane, respectively. The subscripts numerical and ana represent numerical and analytical, respectively, and ana_avg, ana_x=0, ana_x=L represent analytical-derived from concentrations of oxygen vacancies and electrons of bulk average, at feed side and at permeate side, respectively. We find that if the average concentration is used in the analytical solutions, a good agreement can be reached between the numerical and analytical results for all the three fluxes, even though a large discrepancy exists in analytical solutions using local concentrations. Therefore, to use the analytical method to calculate the flux such as that in ref. [61], the average concentration instead of local one should be used. In addition, we also find that in the same reference, the author mistakenly set O_2 flux to be the half of the oxygen vacancy flux, which should have been a quarter of the electron flux. If there was no electron conduction in the SO phase, there would be no net O_2 flux.

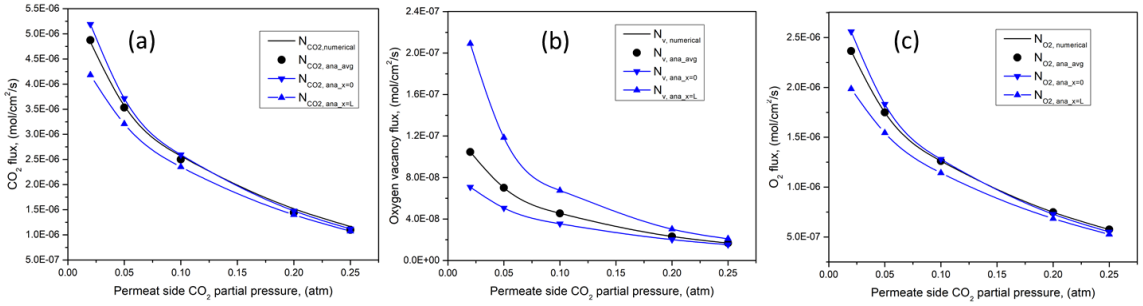

Figure 5.10 Comparison of transmembrane fluxes of LSCF/MC membrane derived from numerical and analytical methods vs different permeate-side pCO_2 and a fixed T=800°C: (a)CO_2 flux; (b) oxygen vacancy flux; (c) O_2 flux

5.5.4 MOEECC: MDC/MC/LNO

Recently, a new high CO_2-flux membrane with three parallel pathways is reported, in which a new electron conducting phase LNO is formed in situ between NiO and MC [21]. Three pathways result: surface reaction 1-1 (SO and MC phase, pathway 1), surface reaction 2-1 and 1-1 (SO and MC phase, pathway 2); surface reaction 3-2 (LNO phase, pathway 3). Here, we apply the numerical method to solve the governing equations given in Table 5.1 for CO_2 and O_2 fluxes of this three-phase membrane (previously denoted as MOEECC) consisting of MDC, MC and LNO. Due to the complexity of the system, analytical solution is very difficult; thus, we used numerical method to solve the governing equations in Table 5.1 and produce the flux data. The results are shown in Figure 5.11 and 5.12. Since the third electron conducting LNO phase is formed in-situ during operation, we assume it only counts for 0.5% of the total solid phase volume, see Table 5.6.

Figure 5.11a and 5.11b show the total and breakdown of CO_2 and O_2 flux of the membrane. The CO_2 flux can be split up into three partial fluxes, corresponding to the three pathways, ½ $N_{e,\ LNO}$ (pathway 3), -$N_{v,\ MOEC}$ (pathway 1), ½ $N_{e,\ MOEC}$ (pathway 2), respectively. The oxygen vacancy is transported in the opposite direction of CO_2; every 2 electrons will result in 1 CO_2. The results suggest that the additional pathway 3 increases

CO_2 flux by ~ 75% compared to MOEC/MC (denoted as MOECC) membrane. The O_2 flux is resulted from pathway 3 (½ $N_{O2,\,LNO}$) and pathway 2 (½$N_{O2,\,MOEC}$), and increased from 0 to 1.4×10^{-7} mol/cm^2/s as the permeate-side pCO_2 is decreased from 0.25 to 002 atm. Figure 5.11c further confirms that the flux ratio of CO_2/O_2 is higher than 2, and the higher the permeate-side pCO_2, the higher the ratio. The additional CO_2 comes from pathway 1-1. Overall, a small amount of LNO can enhance the CO_2 flux substantially by providing additional electronic pathway for CO_2 transport.

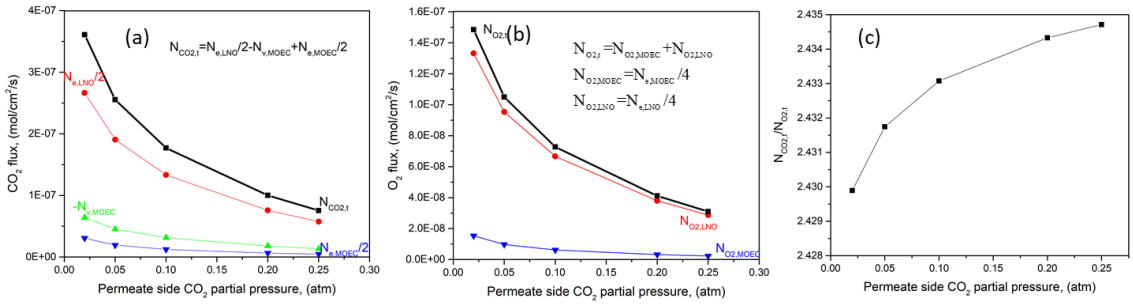

Figure 5.11 Breakdown of numerical CO_2 and O_2 fluxes of membrane under different permeate-side pCO_2 and a fixed T=800^{o}C: (a) CO_2 flux; (b) O_2 flux; (c) CO_2/O_2 ratio

Similarly, the temperature effect on the MOEECC membrane is shown in Figure 5.12. The enhancement brought by LNO phase is also ~ 75% in CO_2 flux, accompanied by a significant increase in O_2 flux. In Figure 5.13c, the flux ratio of CO_2/O_2 is > 2 and increases with operating temperature as a result of higher CO_2 flux contribution from pathway 1.

Note that if the SO phase (such as GDC) can be treated as a pure oxygen vacancy conductor, the analytical solution of the problem could be derived, which is given in chapter 4 and Table 5.4.

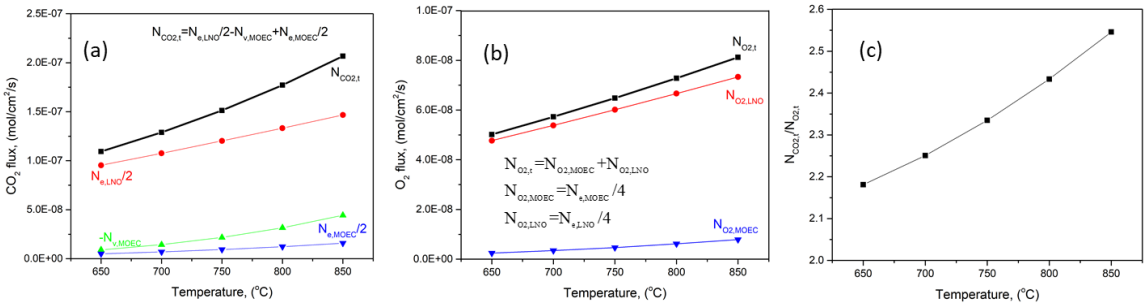

Figure 5.12 Comparison of numerical CO_2 and O_2 fluxes of membrane with and without LNO phase at different temperatures and a fixed permeated side pCO_2=0.1 atm: (a) CO_2 flux; (b) O_2 flux; (c) CO_2/O_2 ratio

If solid oxide phase was LSCF, the LNO phase will still be beneficial to boost the flux, however, since the electronic conductivity of LSCF is comparable to that of LNO, but the volume ratio of LSCF is much higher than that of LNO, the CO_2 flux will be dominated by the LSCF phase, whereas LNO phase could only contribute to a small portion of the total flux. However, the order of magnitude of the total CO_2 flux will be close that reported in Fig 5.10 for LSCF/MC membrane.

5.6 CONCLUSION

In this work, we have calculated CO_2/O_2 flux of four types of multiphase solid/MC membranes for CO_2 transport both numerically and analytically. For solids with a single charge carrier, oxygen vacancy or electron, analytical and numerical results are virtually identical. For solids of mixed oxide-ion and electron conductors, numerical methods are preferred over analytical counterparts due to the fact that the nonlinear variations of charge carrier concentrations across the membrane under large chemical potential gradient cannot be solved analytically. From the transport perspective of membranes, the models indicate that without O_2 in the feed, GDC/MC membrane is preferable over YSZ/MC membrane, yielding 4-9 times higher CO_2 flux over a temperature range of 650-850 ^oC and permeate-side pCO_2 range of 0.02-025 atm. With O_2 in the feed, Ag/MC membranes exhibit higher

CO_2/O_2 flux than LSCF/MC. This study also reveals that in the new MOEECC membrane including a new separate electron-conducting phase LNO, the CO_2/O_2 flux can be markedly enhanced by the additional electronic pathway and the resultant membrane is virtually a combination of MOCC and MECC membranes.

CHAPTER 6

PERFORMANCE PROJECTION OF A HIGH TEMPERATURE CO_2 TRANSPORT MEMBRANE REACTOR FOR COMBINED CO_2 CAPTURE AND METHANE-TO-ETHYLENE CONVERSION[3]

Direct conversion of methane into ethylene through oxidative coupling of methane (OCM) is a technically important reaction. However, conventional co-fed fixed-bed OCM reactors still face serious challenges in conversion and selectivity. In this paper, we apply a finite element model to simulate OCM reaction in a plug-flow CO_2/O_2 transport membrane (CTM) reactor with the directly captured CO_2 and O_2 mixture as a soft oxidizer. The CTM is made of three phases: molten carbonate, 20% Sm-doped CeO_2, and $LiNiO_2$. The membrane parameters are first validated by CO_2/O_2 flux data obtained from CTM experiments. The OCM reaction is then simulated along the length of tubular plug-flow reactors filled with a La_2O_3-CaO-modified CeO_2 catalyst bed, while a mixture of CO_2/O_2 is gradually added through the wall of the tubular membrane. A 12-step OCM kinetics is

---

[3] Xin Li, Kevin Huang, and Xinfang Jin, Submitted to Journal of The Electrochemical Society

considered in the model for the catalyst bed and validated by data obtained from a co-fed fixed-bed reactor. The modeled results indicate a much-improved OCM performance by membrane reactor in terms of C_2-yield and CH_4 conversion rate over the state-of-the-art, co-fed, fixed-bed reactor. The model further reveals that improved performance is fundamentally rooted in the gradual methane conversion with CO_2/O_2 offered by the plug-flow membrane reactor.

6.1 INTRODUCTION

A recent notable development in the energy field is the significantly increased production of natural gas (NG) from shale and tight oil [108]. If the newly available, low-cost NG is only used for producing heat and power as in the past, it will continue to emit significant amount of CO_2 into the atmosphere and add burdens to the current effort to mitigate global warming and climate change issues [109, 110]. Alternatively, NG can be directly converted into value-added products with minimal CO_2 emissions [20]. This direct methane conversion (DMC) approach is also economically attractive due to higher values of the final products [21, 90].

The most studied DMC technology is Oxidative Coupling of Methane (OCM), transforming CH_4 into ethylene (C_2H_4) with molecular O_2 as the oxidant in a single step [111]. A major technical challenge for the OCM process is to achieve high CH_4 conversion at high C2 selectivity [112]. A number of new reactor designs have been proposed based on the concept of controlling the oxygen content to prevent over-oxidation of the desirable C2 products [113].

From a design perspective, there are generally three types of reactors: moving or fluidized-bed reactor, fixed-bed reactor, and membrane reactor [114, 115]. For the moving or fluidized bed reactors, the solid catalysts need to be replenished at a high frequency in order to remove coke and achieve a C2 yield greater than 50% [116, 117]. However, it is energy intensive to invest on larger reactor vessels, regenerate large amount of solid catalyst, and provide high pumping power to move the catalyst. For the fixed-bed reactors, there is little control over the over-oxidation of C2 such that C2 yield is often limited to <25% [118]. There were some proposed fixed-bed reactors with the ability to control the oxygen concentration in a continuous reactor by distributing the oxygen feed during the reaction to reduce the over-oxidation of C2 products. But, to distribute oxygen feed in a reactor is not trivial and could become very costly [119]. The membrane reactors reported in the open literature are either porous membrane reactors or membrane reactors with solid-oxide O_2 transport materials (OTMs) [120, 121]. However, the improvement in C2 yield and selectivity demonstrated so far is still marginal [122].

To control oxygen concentration, previous studies have shown that using nitrogen oxide, carbon oxide or sulfur as a soft oxidizer can appreciably improve the conversion-selectivity relationship [123]. Here in this study, we investigate from a modeling perspective the performance of a membrane reactor to directly convert methane to ethylene via OCM using a mixture of CO_2/O_2. In this case, a multi-phase, high-temperature CO_2 transport membrane (CTM) is used to separate CO_2 and O_2 from a carbon source such as flue gas and simultaneously react with methane on the other side of the membrane to form ethylene in the presence of OCM catalysts. We combine experimental data from the most recent CTM study and reaction kinetics of La_2O_3-CaO-modified CeO_2 catalyst in a

Multiphysics micromodel to predict CH_4 conversion rate and C2 yield in a new plug-flow membrane reactor. The performance of the reactor is then compared with a fixed-bed reactor counterpart to show the advantages of the new technology.

6.2 TYPES OF REACTORS SIMULATED

In this study, we simulate a tubular plug-flow membrane reactor and a fix-bed reactor for validation and comparison purposes. The working principle of each reactor is schematically illustrated in Figure 6.1a and 6.1b. In the membrane reactor, the CTM consists of three phases: Sm-doped CeO_2 as the solid oxide (SO) phase, molten eutectic Li_2CO_3-Na_2CO_3 as the molten carbonate (MC) phase, and the $LiNiO_2$ (LNO) phase formed in-situ between NiO and MC working as the electron conducting phase [124]. With such a membrane composition, only CO_2 and O_2 in the flue gas can permeate through the membrane to react with methane on the other side. The central passage of the plug-flow membrane reactor is filled with La_2O_3-CaO-modified CeO_2 catalyst having a 34% porosity. A pure stream of methane is fed into the reactor through the catalyst bed, while a mixture of CO_2, O_2, and N_2 as a mockup of the flue gas from power plants is fed along the outer surface of the reactor. During operation, the CTM gradually adds CO_2 and O_2 into the methane chamber under the gradient of chemical potentials of CO_2 and O_2. There are eleven catalytic reactions (solid line in the reaction network shown in Figure 6.3b) on the surface and one bulk reaction in the gas phase (dashed line in the same plot) considered inside the reactor (methane chamber). The corresponding reaction kinetics have been listed in Table 6.1. Ethylene is the product in the outlet. A 2D axial symmetrical model was built to simulate the performance of membrane reactor coupled with a catalyst bed.

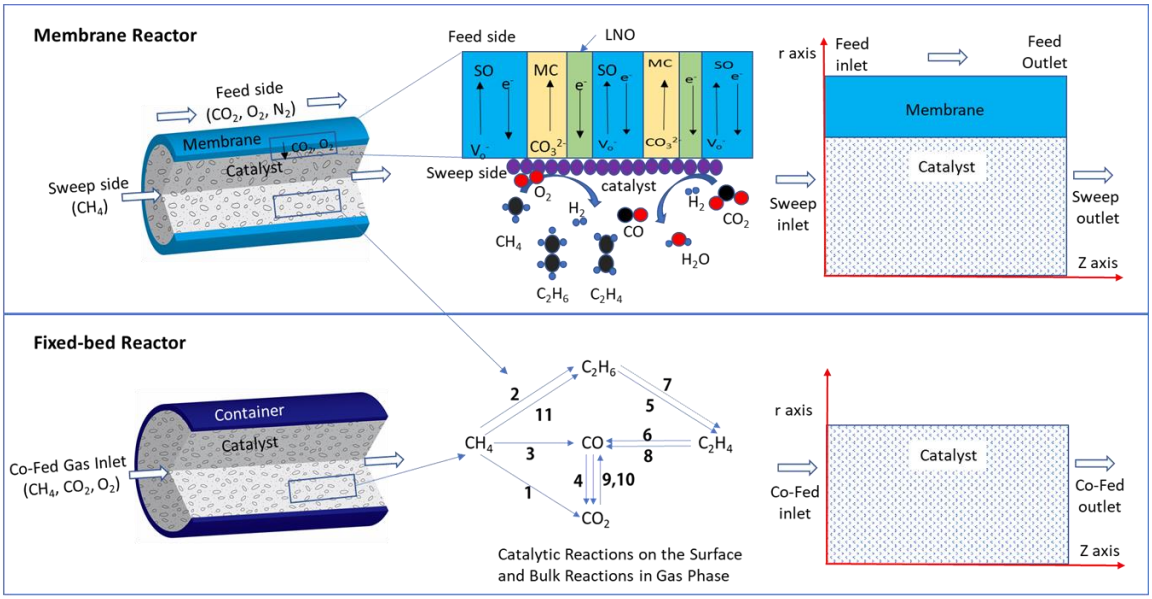

Figure 6.1 Schematic illustration of (a) membrane reactor; (b) co-fed fixed bed

In the fixed-bed reactor, the composition, diameter, and length, as well as the porosity of the catalyst bed, and the inlet CH_4 flow velocity are the same as the membrane reactor. There are, however, two major differences in the fixed-bed reactor modeling compared to the membrane reactor: 1) a mixture of CH_4 and CO_2/O_2 is co-fed at the inlet of the reactor; 2) there is only one computational domain for the catalyst bed.

6.3 MATHEMATICAL MODELS

In this section, we give more details about the mathematical models to simulate both OCM reactors. The reaction kinetics of OCM on La_2O_3-CaO-modified CeO_2 catalyst involves many species. A set of 10-step kinetic model was first proposed by Stansch et al. [26] for O_2 OCM. It describes the differential rates of formation of different species under a wide range of operating conditions ($1<p_{O2}<20$kPa, $10<p_{CH4}<95$kPa, $973<T<1228$K). The kinetic model includes thermal cracking, steam reforming and water gas shift reactions, see Table 1. The kinetic parameters are estimated based on experimental data obtained from a microcatalytic fixed bed reactor in the validation section [108]. The reaction rate

equations are either in Hougen-Watson type (reaction 1-6) or Power-law type (reaction 7-10). In addition, we also considered direct reaction between CH_4 and CO_2 as reaction (11) with the experimental data from Wang et al. [125].

Table 6.1 Reactions and kinetic rates

Index	Reaction	Reaction Kinetics
1	$CH_4 + 2O_2 \rightarrow CO_2 + 2H_2O$	$r_1 = \frac{\left(k_{01}\cdot e^{-\frac{E_a}{RT}}\right)\cdot P_{CH_4}^{m_1}\cdot P_{O_2}^{n_1} - k_b ve^{-\frac{E_a}{RT}}\cdot P_{CO_2}^{m_1}\cdot P_{H_2O}^{n_1}}{(1+K_{1,CO_2}\cdot e^{-\frac{\Delta H_{ad,CO_2,1}}{RT}}\cdot P_{CO_2})^2}$
2	$2CH_4 + 0.5O_2 \rightarrow C_2H_6 + H_2O$	$r_2 = \frac{k_{02}\cdot e^{-\frac{E_a}{RT}}\cdot (K_{0O_2}\cdot e^{-\frac{\Delta H_{adO_2}}{RT}}P_{O_2})^{n_2}P_{CH_4}}{[1+\left(K_{0,O_2}\cdot e^{-\frac{\Delta H_{ad,O_2}}{RT}}\cdot P_{O_2}\right)^n + K_{2,CO_2}\cdot e^{-\frac{\Delta H_{ad,O_2}}{RT}}P_{O_2}]^2}$
3	$CH_4 + O_2 \rightarrow CO + H_2O + H_2$	$r_3 = \frac{\left(k_{03}\cdot e^{-\frac{E_a}{RT}}\right)\cdot P_{CH_4}^{m_3}\cdot P_{O_2}^{n_3} - k_b\cdot e^{-\frac{E_a}{RT}}\cdot P_{CO_2}^{m_3}\cdot P_{H_2O}^{n_3}}{(1+K_{3,CO_2}\cdot e^{-\frac{\Delta H_{ad,CO_2,3}}{RT}}\cdot P_{CO_2})^2}$
4	$CO + 0.5O_2 \rightarrow CO_2$	$r_4 = \frac{\left(k_{04}\cdot e^{-\frac{E_a}{RT}}\right)\cdot P_{CH_4}^{m_4}\cdot P_{O_2}^{n_4} - k_b\cdot e^{-\frac{E_a}{RT}}\cdot P_{CO_2}^{m_4}\cdot P_{H_2O}^{n_4}}{(1+K_{4,CO_2}\cdot e^{-\frac{\Delta H_{ad,CO_2,4}}{RT}}\cdot P_{CO_2})^2}$
5	$C_2H_6 + 0.5O_2 \rightarrow C_2H_4 + H_2O$	$r_5 = \frac{\left(k_{05}\cdot e^{-\frac{E_a}{RT}}\right)\cdot P_{CH_4}^{m_5}\cdot P_{O_2}^{n_5} - k_b\cdot e^{-\frac{E_a}{RT}}\cdot P_{CO_2}^{m_5}\cdot P_{H_2O}^{n_5}}{(1+K_{5,CO_2}\cdot e^{-\frac{\Delta H_{ad,CO_2,5}}{RT}}\cdot P_{CO_2})^2}$
6	$C_2H_4 + 2O_2 \rightarrow 2CO + 2H_2O$	$r_6 = \frac{\left(k_{06}\cdot e^{-\frac{E_a}{RT}}\right)\cdot P_{CH_4}^{m_6}\cdot P_{O_2}^{n_6} - k_b\cdot e^{-\frac{E_a}{RT}}\cdot P_{CO_2}^{m_6}\cdot P_{H_2O}^{n_6}}{(1+K_{6,CO_2}\cdot e^{-\frac{\Delta H_{ad,CO_2,6}}{RT}}\cdot P_{CO_2})^2}$
7	$C_2H_6 \rightarrow C_2H_4 + H_2$	$r_7 = k_{07}\cdot e^{-\frac{E_{a7}}{RT}}P_{C_2H_6}$
8	$C_2H_4 + 2H_2O \rightarrow 2CO + 4H_2$	$r_8 = k_{08}\cdot e^{-\frac{E_{a8}}{RT}}P_{C_2H_4}^{m_8}\cdot P_{H_2O}^{n_8}$
9	$CO + H_2O \rightarrow CO_2 + H_2$	$r_9 = k_{09}\cdot e^{-\frac{E_{a9}}{RT}}P_{CO}^{m_9}P_{H_2O}^{n_9}$
10	$CO_2 + H_2 \rightarrow CO + H_2O$	$r_{10} = k_{10}\cdot e^{-\frac{E_{a10}}{RT}}P_{CO_2}^{m_{10}}P_{H_2}^{n_{10}}$
11	$2CH_4 + CO_2 \rightarrow C_2H_6 + H_2O+CO$	$r_{11} = k_{11}\cdot e^{-\frac{E_{a11}}{RT}}P_{CH_4}^{m_{11}}P_{CO_2}^{n11}$

Table 6.2 lists the governing equations and boundary conditions in both the membrane and the catalyst bed. The model was solved using commercial finite element package COMSOL 5.4, Mathematics/The General Form PDE interface. Mapped mesh with 3500 linear quadrilateral elements was used in discretization. According to the definition

of our previous work [126], the membrane consists of three phases: molten carbonate phase transporting carbonate ions, mixed oxide and electron conducting phase transporting both oxide-ions and electrons, and the LNO phase transporting electrons only. Therefore, there are four charge conservation equations in the membrane domain. The details of the governing equations and boundary conditions can be found in our previous work [126]. In the catalyst bed, the diffusion and convection of the gas species are described by transport of dilute species in porous media. The reaction kinetics at the catalyst surface or the bulk are given in Table 6.3. The velocity of the gas stream is assumed to be constant.

To evaluate the overall performance of the OCM reactors, three metrics are used: C2 yield (Y_{C_2}), selectivity (S_{C_2}), and CH_4 conversion rate (C_{CH4}), which are calculated by:

$$Y_{C_2} = S_{C_2} \cdot C_{CH4} \tag{6-1}$$

$$S_{C_2} = \frac{[2 \times (J_{C_2H_4,out} - J_{C_2H_4,in}) + 2 \times (J_{C_2H_6,out} - J_{C_2H_6,in})]}{J_{CH4,in} - J_{CH4,out}} \tag{6-2}$$

$$C_{CH4} = \frac{J_{CH4,in} - J_{CH4,out}}{J_{CH4,in}} \tag{6-3}$$

6.4 PARAMETERS AND MODEL VALIDATION

Validation of the CTM and the catalyst bed were done separately with different sets of experimental data. The 1D CTM model was validated by experimental data from button cell of our previous work [126]. Here, we extend the model from 1D [21] to 2D. Therefore, in Figure 6.2a, we compare the CO_2 fluxes calculated by both 1D and 2D models with experimental data and found good agreement among the three sets of data. So, we think the membrane parameters validated from experimental button cell data can be used to simulate the performance of a pilot-scale membrane.

Table 6.2 Governing equations and boundary conditions for different domains

Physics	Governing Eq.	B.C. @ Feed Side (Outer surface)	B.C. @ Sweep Side (Inner surface)
Membrane			
Oxygen vacancy conservation in SO phase	$\nabla \cdot J_V = -\frac{(1-\varepsilon)}{\tau_{SO}}\left(Z_V F D_V \nabla^2 C_V + \frac{{Z_V}^2 F^2 D_V C_V}{RT}\nabla^2 \emptyset_{SO}\right) = 0$	$\emptyset_{SO,0} = \frac{RT\left(\ln\frac{P_{CO_2,0}C^0}{P^0\ C_V}\right)-\beta}{FZ_V}$	$J_V + J_n + J_C + J_{n,LNO} = 0$
Molten carbonate ion conservation in MC phase	$\nabla \cdot J_C = -\frac{\varepsilon}{\tau_{MC}}\sigma_C \nabla^2 \emptyset_{MC} = 0$	$\emptyset_{MC}(x=0) = 0$	$\emptyset_{MC,L} = \frac{RT\left(\ln\frac{P_{CO_2,L}C^0}{P^0\ C_V}\right)-\beta}{FZ_C} - \frac{Z_V \emptyset_{SO,L}}{Z_C}$
Electron/hole conservation in SO phase	$\nabla \cdot J_n = -\frac{(1-\varepsilon)}{\tau_{SO}}\left(Z_n F D_n \nabla^2 C_n + \frac{Z_n^2 F^2 D_n C_n}{RT}\nabla^2 \emptyset_{SO}\right) = 0$	$C_n(0) = K_T^{1/2} C_v^{1/2} {P_{O_2,0}}^{1/2}$ $Z_V C_V + Z_n C_n + Z_D C_D = 0$	$C_n(L) = K_T^{1/2} C_v^{1/2} P_{O_2,L}^{1/2}$ $Z_V C_V + Z_n C_n + Z_D C_D = 0$
Electron conservation in metal phase	$\nabla \cdot J_{e,LNO} = -V_{LNO}\left(\sigma_{e,LNO}\nabla^2 \emptyset_{LNO}\right) = 0$	$\emptyset_{LNO,0} = \frac{\chi}{2Z_e F} - \frac{RT}{2Z_e F}\ln\frac{P_{CO_2,0}}{P^0}\left(\frac{P_{O_2,0}}{P^0}\right)^{0.5}$	$\emptyset_{LNO,L} = \frac{\chi}{2Z_e F} - \frac{RT}{2Z_e F}\ln\frac{P_{CO_2,L}}{P^0}\left(\frac{P_{O_2,L}}{P^0}\right)^{0.5} + \frac{Z_C}{2Z_e}\emptyset_{MC,L}$
Catalyst Bed			
Transport of diluted species in porous media	$\nabla \cdot N_i + \mathrm{u} \cdot \nabla c_i = R_i$ $N_i = -D_i \nabla C_i$	Inflow (Left inlet): $c_i = c_{0,i}$	Outflow (Right outlet): $\mathrm{n} \cdot D_i \nabla c_i = 0$

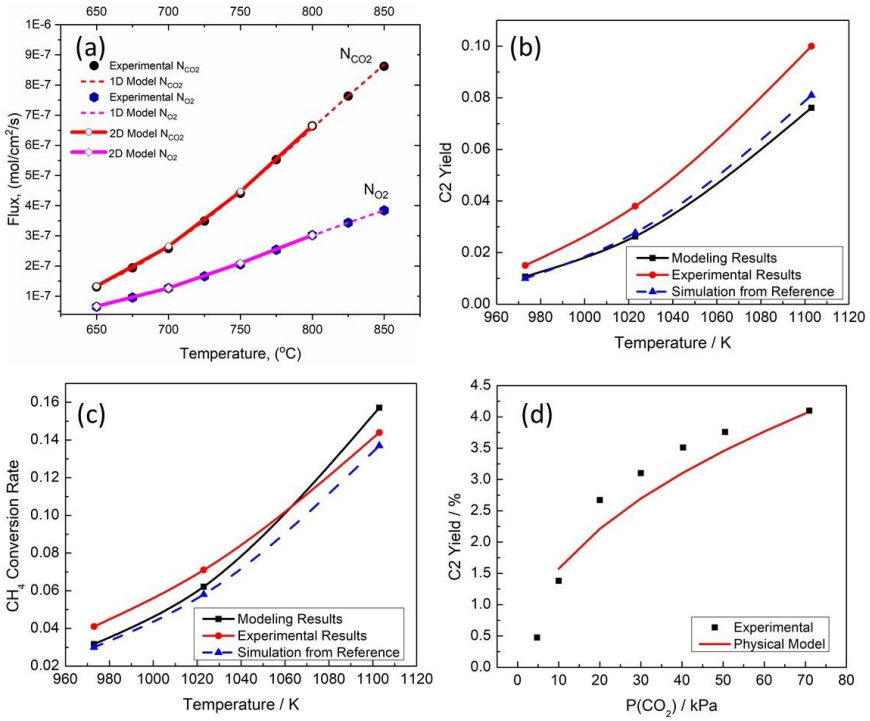

Figure 6.2 Validation of the reactors: (a) CO_2 flux validation of the membrane; (b) validation of O_2 OCM for the fixed catalyst bed in C2 yield; (c) validation of O_2 OCM for the fixed catalyst bed in CH_4 conversion rate; (d) Validation of CO_2 OCM for the fixed catalyst bed

Validation of the O_2 OCM catalyst bed is done by optimization of the C2 yield and CH_4 conversion rate to fit their experimental data obtained from a micro-catalytic fixed-bed reactor with La_2O_3/CaO catalyst as reported by Stansch [127, 128]; the results are shown in Figure 6.2b and 6.2c. With the obtained 10-step reaction kinetic parameters listed in Table 6.3, an actual micro-catalytic reactor shown in Figure 6.1 is simulated. Validation of reaction 11 with CaO/modified CeO_2 catalyst for CO_2 direct oxidation of CH_4 is done with experimental data [22]; the results are shown in Figure 6.4d.

Table 6.3 Kinetic parameters for catalytic and bulk reactions

Index	k_{0j} $mol^{-1}\times g^{-1}\times s^{-1}\times Pa^{-(m+n)}$	$E_{a,j}$	$K_{j,CO2}$	$\Delta H_{ad,CO2}$,kJ/mol	K_{O2},Pa^{-1}	$\Delta H_{ad,O2}$	m_j	n_j
1	0.2×10^{-5}	48	0.25×10^{-12}	-175	—	—	0.24	0.76
2	23.2	182	0.83×10^{-13}	-186	0.23×10^{-11}	-124	1	0.4
3	0.52×10-^{6}	68	0.36×10^{-13}	-187	—	—	0.57	0.85
4	0.11×10^{-3}	104	0.4×10^{-12}	-168	—	—	1	0.55
5	0.17	157	0.45×10^{-12}	-166	—	—	0.95	0.37
6	0.06	166	0.16×10^{-12}	-211	—	—	1	0.96
7	1.2×10^{7}	226	—	—	—	—	—	—
8	9.3×10^{3}	300	—	—	—	—	0.97	0
9	0.19×10^{-3}	173	—	—	—	—	1.0	1.0
10	0.26×10^{-1}	220	—	—	—	—	1.0	1.0
11	1.8×10^{-7}	140					2	0.5

After the validation, a composite catalyst La_2O_3/CaO/modified CeO_2 catalyst for both O_2 OCM and CO_2 OCM has been used in the model as the catalyst bed. It is then used to simulate the performance of a membrane reactor and a fixed-bed reactor with the same catalyst bed dimensions and operating conditions given in Table 4. The material properties in the table are obtained from validation.

Table 6.4 Parameters and operating conditions for both fixed-bed and membrane reactors

Parameter	Value	Reference
Common Parameters for Both Reactors		
Reactor length	0.4 [m]	[128]
Reactor diameter	0.018 [m]	
Operating temperature	973-1103 [K]	
Sweep gas composition	99.3% CH_4	
CH_4 stream velocity	0.39 [m/s]	
CO_2 diffusivity	$1.39\times10^{-4}[m^2/s]$	[129]
CO diffusivity	$1.45\times10^{-4}[m^2/s]$	
O_2 diffusivity	$1.52\times10^{-4}[m^2/s]$	
CH_4 diffusivity	$1.57\times10^{-4}[m^2/s]$	

C_2H_6 diffusivity	$1.31\times10^{-4}[m^2/s]$	
C_2H_4 diffusivity	$1.37\times10^{-4}[m^2/s]$	
H_2O diffusivity	$1.95\times10^{-4}[m^2/s]$	
H_2 diffusivity	$6.20\times10^{-4}[m^2/s]$	
Membrane Reactor Specific Parameters		
Membrane thickness	0.2 [mm]	[21]
Feed gas composition	15% CO_2: 10% O_2:75% N_2	[21]
Sweep gas composition	99.3% CH_4	—
LNO conductivity	$\ln\sigma = 5.8456 - \frac{463.9}{T}$ [S/m]	[21]
Molten Carbonate conductivity	$\sigma = -4.6866 + 8.533\cdot10^{-3}\cdot T - 1.325\cdot10^{-6}\cdot T^2$	[104]
SDC20 ionic conductivity	$\sigma_i = \frac{Z_i^2 F^2 D_i C_i}{RT} = Z_i^2 F \mu_i C_i$ $\log_{10}(\mu_{i,10}T) = 2.4656 - 3.40416\cdot\frac{1000}{T}$ $\log_{10}(\mu_{i,20}T) = 2.36515 - 3.56931\cdot\frac{1000}{T}$	[99, 100]
SDC20 electronic conductivity	$\log_{10}(\mu_{e,10}T) = 4.1943 - 4.30072\cdot\frac{1000}{T}$ $\log_{10}(\mu_{e,20}T) = 2.63204 - 2.6264\cdot\frac{1000}{T}$	[99, 100]
Tortuosity of the solid oxide phase	2.5	[126]
Tortuosity of the molten carbonate phase	$\ln\tau_{MC} = -9.2167 + \frac{11234.4}{T}$	[126]
Tortuosity of the LNO phase	$\tau_{LNO} = 0.5768 + 0.0055\cdot T$	[126]
Volume fraction of molten carbonate	0.5	[126]
Volume fraction of LNO phase	0.01	[126]
Fixed-Bed Reactor Specific Parameters		
Inlet gas composition	8.7%CO_2, 4.3%O_2, 87% CH_4	[128]

6.5 SET UP FOR COMSOL MULTIPHYSICS

For the 2-D model, membrane thickness is along the r direction and the reactor flow is along the reverse of the z direction. An additional "transport of dilute species (tds)" interface under "Chemical Species Transport" is needed. It is used to calculate the concentration profile of all the gas species transported by diffusion and convection as well as reaction. All species are assumed to be diluted. There are 8 species and 10 reactions for

the oxidative coupling of methane (Chapter 6), and 5 species and 6 reactions for the dry-oxy reforming of methane (Chapter 7) taken into consideration. The velocity of the gas mixture is given as a constant. The diffusion coefficient of each species is added in the materials node. Also, the reaction rates for both bulk and catalytic reactions are defined in this model. The inflow gas concentration and initial values are given. In the fixed-bed reactors, the gas composition of the inflow is a mixture of $CH_4/CO_2/O_2$, whereas in the membrane reactor, only methane was fed at the inlet, oxygen and carbon dioxide, are permeated through the membrane.

After the boundary conditions and governing equations are implemented, the model is ready to be meshed, in which the geometry of the model is broken down into smaller pieces (elements). A finer mesh will result in a more accurate solution, but it requires more time to compute. Therefore, balancing the accuracy and the computation time is necessary for a complicate model. For the 1D model, the "physics-controlled mesh" was used to build the extremely fine mesh, while for the 2D model, the "user-controlled mesh" is used to build the desired mesh distribution. Mesh of the 2-D model built in this work is shown in Figure 6.3.

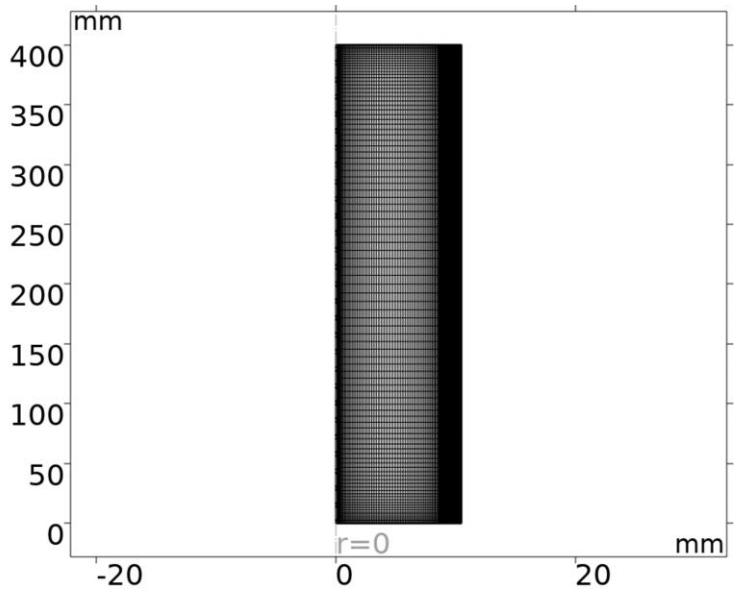

Figure 6.3 Mesh of the 2-D model of the tubular membrane reactor

The last step is to specify the study settings. Since this problem is a stationary problem, the stationary solver is used. Then, a parametric study is created to sweep the parameter through a specified range. Parameter such as temperature, partial pressure and reactor length are used as sweeping parameters to study their influence on the performance of the membrane, the membrane reactor and the fixed-bed reactor.

6.6 RESULTS AND DISCUSSION

In this section, we compare the simulated performance of a membrane reactor and a fixed-bed reactor with the same catalyst bed and operating conditions. The operating temperature is varied between 973K and 1103K. The purpose of this study is to demonstrate the improved performance with the new membrane reactor over the state-of-the-art fixed-bed reactor.

6.6.1 Fixed-Bed Reactor

Figure 6.4 shows 2D axial symmetric molar fraction profiles of gas species in a co-fed fixed-bed reactor under 1103K. Note that the 2D domain will be rotated around its vertical orientation to form a cylinder in 3D. CH_4 and CO_2/O_2 streams are co-flowing from the top inlet to the bottom outlet of the cylindrical catalyst bed. To ensure a fair comparison, CO_2/O_2 flowrates are the same as their equivalent flowrates permeated through the membrane in the membrane reactor. The wall of the container is under zero-flux boundary condition. It can be seen that CH_4 and CO_2/O_2 have been continuously converted to CO, C_2H_6, C_2H_4, H_2O and H_2, as the stream move toward the outlet (bottom) of the tubular reactor.

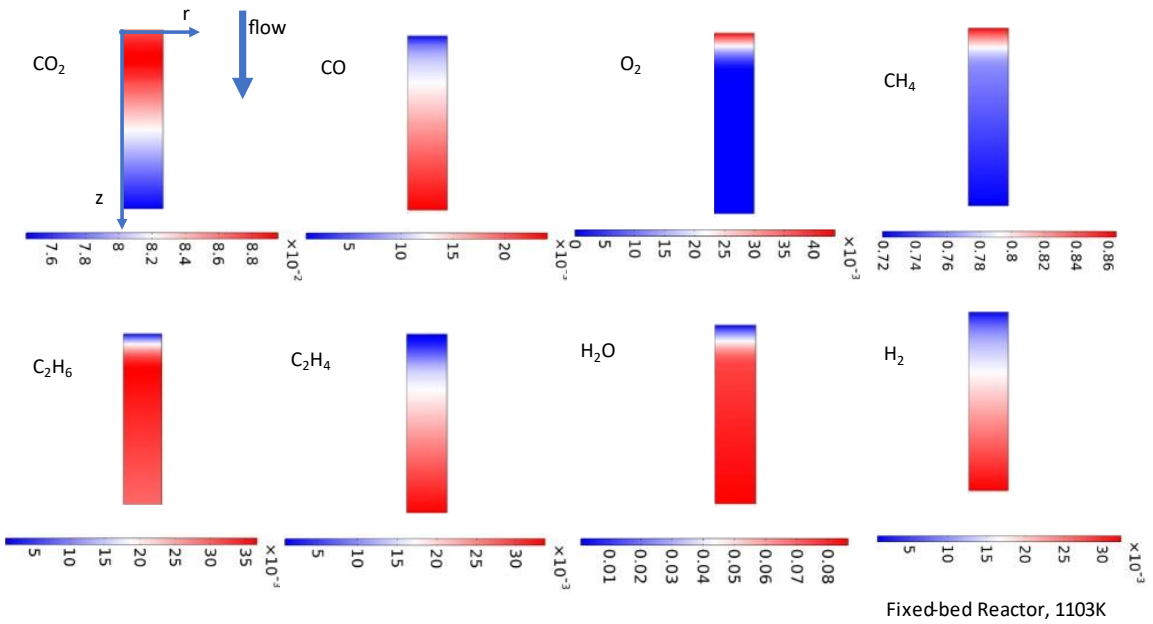

Figure 6.4 2D axial symmetric gas species molar fraction profiles in the fixed-bed reactor under 1103K

To show the gas species molar fraction profiles along the flow direction under different temperatures quantitatively, we plotted their profiles along the z-axis of the cylindrical catalyst bed, see Figure 6.5. Since CH_4 molar fraction is much higher than the

rest of the species, it is not plotted here. CH_4 conversion rate will be discussed in section 6.6.3. The inlet corresponds to z=0mm and outlet is at z=400mm. The following trends are observed: 1) The molar fraction of C_2H_6 increases with temperature from 973K to 1023K, and then decreases sharply toward 1103K. 2) The produced molar fraction of C_2H_4 surpassed that for C_2H_6 at 1103K. 3) The molar fraction of H_2O rises sharply first and then stays flat around 0.09 as temperature increases. 4) CO molar fraction is below 0.02 for all three cases. 5) O_2 molar fraction decreases fast with temperature and then becomes depleted at 1103K. 6) CO_2 molar fraction profiles are quite stable for the lower temperatures but started to decrease largely at 1103K.

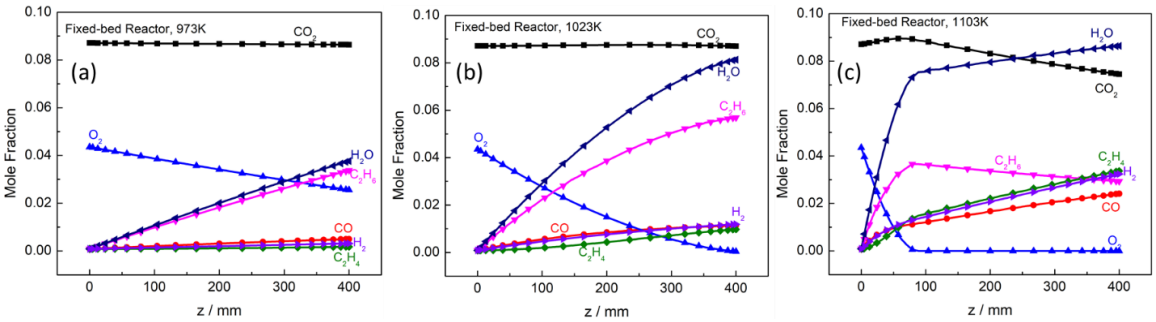

Figure 6.5 Molar fractions of gas species in the co-fed fixed-bed reactor along the z axis under: (a) 973K; (b) 1023K; (c) 1103K

To understand the molar fraction profiles of all species and its relationship with the catalytic and bulk reactions in the fixed-bed reactor, the reaction rates of all 11 reactions listed in Table 1 are plotted along the z-axis of the reactor. There are 10 catalytic reactions (1-6, 8-11) with a unit of mol/kg/s, and 1 bulk reaction (7) with a unit of $mol/m^3/s$. The catalytic reactions are plotted against the left y-axis in Fig. 5 and the bulk reaction is plotted against the right y axis. Reaction 3 (producing undesirable C1), reaction 2 and 11 (producing desirable C2) are the most significant reactions. Reaction 3 shows a decreasing trend along the z axis and decreases faster at higher temperatures. The bulk reaction 7 converts C_2H_6 to C_2H_4 and its reaction rate is enhanced by higher temperatures. Its profile

in the z axis direction is correlated to the reactant C_2H_6 molar fraction. Even though reaction 2 and 11 (C2 reaction) and reaction 7 (from C_2H_6 to C_2H_4) has been significantly enhanced at 1103K, reaction 5 (convert C_2H_6 to C_2H_4) and 6 (convert C_2H_4 to CO) has also been facilitated, which prevents further increase of C2 product in Figure 6.5.

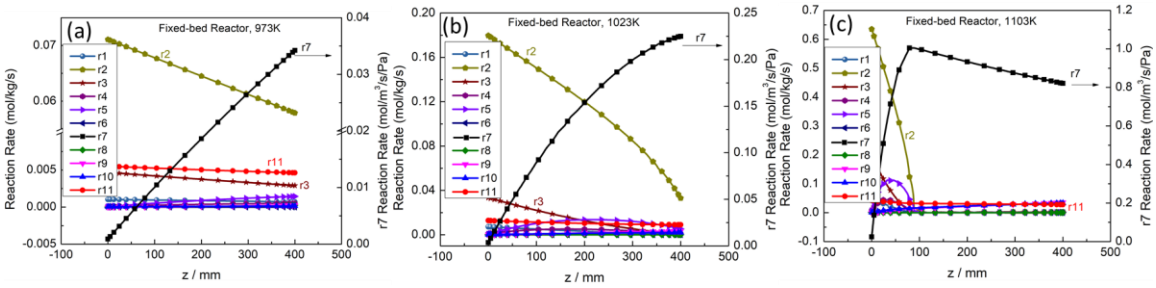

Figure 6.6 Reaction rates in the fixed-bed reactor along the z axis under:(a) 973K; (b) 1023K; (c) 1103K

6.6.2 Membrane Reactor

Different from the fixed-bed reactor, in the membrane reactor, pure CH_4 is fed at the inlet, while CO_2/O_2 is gradually added into the reactor through the CTM. The catalyst bed of the membrane reactor is the same as that for the fixed-bed. The CH_4 inflow velocity is the same as that for the fixed-bed reactor. The flux of CO_2/O_2 is determined by the in-situ CO_2/O_2 partial pressure gradients across the membrane and varies along the z-axis. Their overall flux is the same as that at the inlet of the fixed bed reactor.

Figure 6.7 shows 2D axial symmetric gas species molar fraction profiles along the membrane reactor at 1103K, from which we can see that: 1) CO_2 and O_2 are gradually added into the reactor through the wall of the membrane reactor. 2) CH_4 is consumed in the bulk of the reactor and there is a significant variation along the radial direction since there are more abundant O_2 and CO_2 permeated from the membrane at the inner surface. 3) Both C2 products (C_2H_6 and C_2H_4) are produced in the bulk of the reactor, and their molar fraction are slightly higher along the membrane inner surface. 4) Large amounts of

H_2O and H_2 are also produced at the outlet of the reactor. 5) CO molar fraction is the lowest in the reactor.

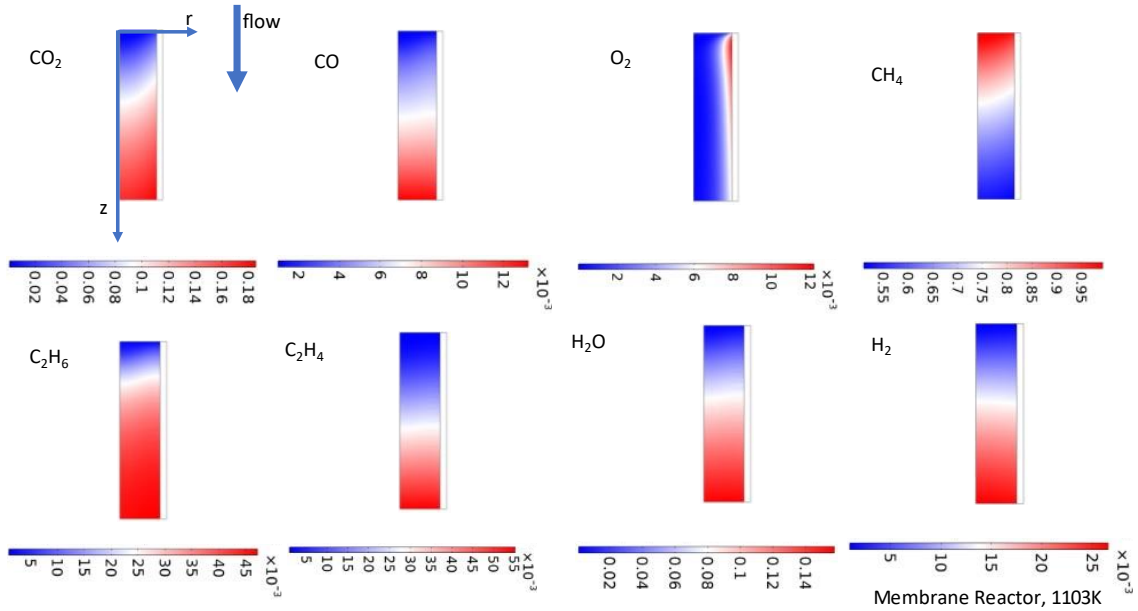

Figure 6.7 2D axial symmetric gas species molar fraction profiles in the membrane reactor under 1103K

Figure 6.8 shows the molar fraction variations along the membrane inner surface in the z-axis direction. Compared to their counterparts' plots for fixed-bed reactors, there are three major differences: 1) C2 (C_2H_4 and C_2H_6) molar fractions are higher for the membrane reactor, especially at higher temperature 1103K. 2) H_2O product mole fraction is one time higher compared with that for the fixed-bed reactor. 3) CO_2 molar fraction becomes dominant species in the product stream, indicating successful capture of the high flux of CO_2 from the flue gas. As temperature increases, CO_2 domination has been weakened by H_2O.

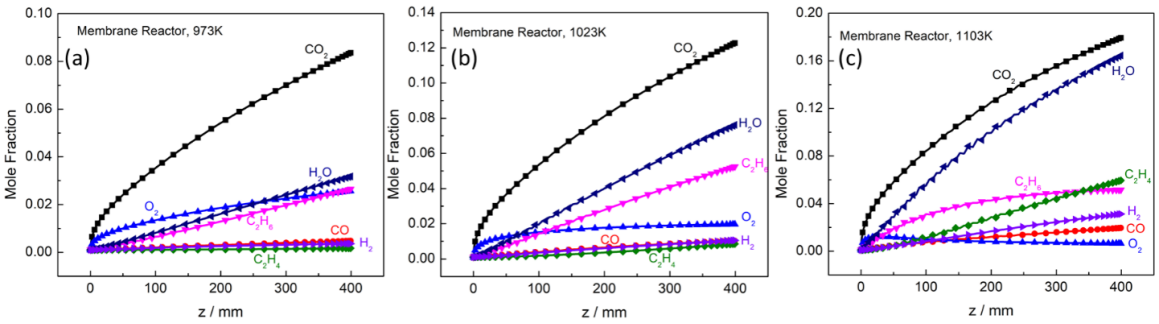

Figure 6.8 Molar fractions of gas species in the membrane reactor along the z-axis under: (a) 973K; (b) 1023K; (c) 1103K

Figure 6.9 further confirms the enhanced reaction kinetics for more desirable reactions, such as reaction 2 and 11 (producing C_2H_6), reaction 5 (producing C_2H_4), especially towards the outlet of the reactor. Therefore, elongating the reactor in the flow direction could further improve its performance by enhancing CO_2/O_2 OCM reaction.

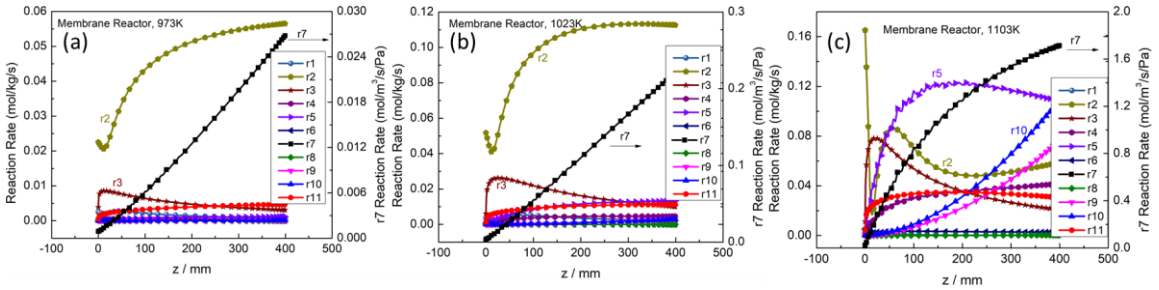

Figure 6.9 Reaction rates in the membrane reactor along the z-axis under: (a)973K; (b)1023K; (c)1103K

6.6.3 Performance Comparison

To compare the overall performance of the two different OCM reactors, C2 yield and selectivity, as well as CH_4 conversion rate from Eq. (6-1)-(6-3) are plotted against operating temperature in Figure 6.10. One can see that 1) for the fixed bed reactor, C2 yield reaches the maximum of ~15% around 1023K, whereas for the membrane reactor, it continues to increase as the temperature increases; 2) C2 selectivity for the membrane reactor could maintain above 93% while that for the fixed-bed falls under 91% at 1103K; 3) The CH_4 conversion rate for the membrane reactor is more than two times of that for the

fixed-bed reactor at 1103K. At the same time, significant amount of CO_2 has been captured in the membrane reactor from the flue gas.

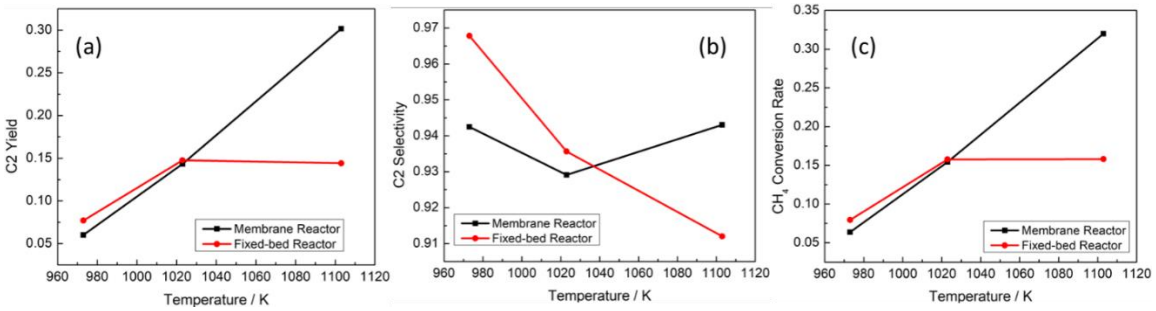

Figure 6.10 Performance comparison between membrane and fixed-bed reactors: (a) C2 yield; (b) C2 selectivity; (c) CH_4 conversion rate

In Figure 11a, CO_2/O_2 flux along the membrane inner surface in the z-axis direction is plotted; it increases with temperature. But it decreases exponentially along the z-axis from the inlet to the outlet at a given temperature. At the inlet, large amount of CO_2/O_2 is needed to convert CH_4 to C2 products; as the stream approaches the outlet, CO_2/O_2 concentration in the membrane reactor increases, which will reduce the driving force for the chemical potential driven diffusion process and leads to reduced CO_2/O_2 flux. In Figure 6.11b, CH_4 molar fraction is plotted against the z-axis. It decreases along the z-axis from the inlet to the outlet. The CH_4 molar fraction decreases more abruptly along the z axis in the membrane reactor than that in the fixed-bed reactor, which is consistent with the CH_4 conversion rate shown in Figure 6.10c.

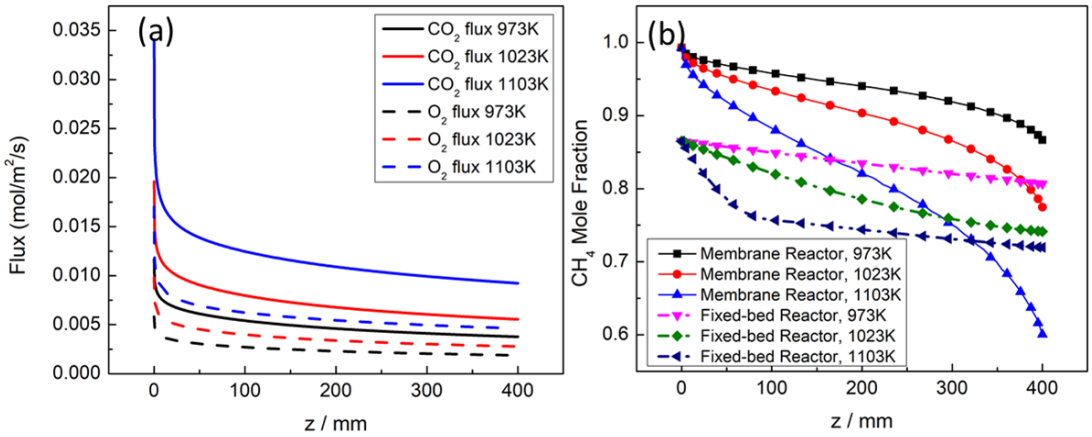

Figure 6.11 (a) CO_2 flux along the gas/membrane interface in the membrane reactor; (b) CH_4 molar fraction comparison between membrane and fixed-bed reactors

The comparison results in Figure 6.10 and Figure 6.11 indicate that the membrane reactor shows improved performance under higher temperature in terms of C2 yield/selectivity and CH_4 conversion rate. However, in practical operation, lower operating temperature is preferred to maintain a longer lifetime of the reactor. An alternative solution to improve the reactor performance at lower temperatures is to increase the length of the reactor. The fixed-bed reactor has the well-known limitation in C2 yield. As shown in Figure 6.12, C2 yield is plateaued at 20% with a reactor length higher than 1.4 m. But for the membrane reactor, as the length increases, C2 yield linearly increases and could reach as high as 32% with a reactor length of 2 m. Therefore, it is economically beneficial to run a longer membrane reactor for combined CO_2 capture and OCM under lower temperature.

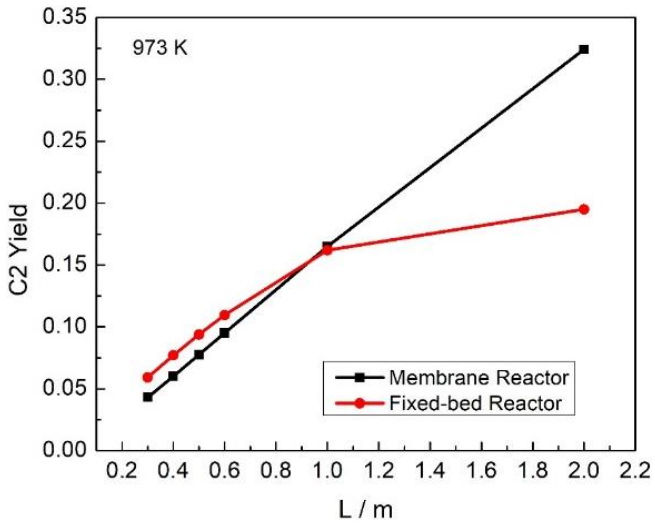

Figure 6.12 C2 yield as a function of reactor length

6.6.4 Coking resistance

Coke formation during OCM reaction is thermodynamically and kinetically favorable, particularly under controlled oxygen condition to avoid over-oxidation, leading to loss of catalyst's activity via pore blockage, collapse of the catalyst support or physical blockage of the tube in the fixed-bed reactor [130]. Coking is a major challenge for OCM to be commercially viable. We here assess the coking possibility of OCM in fixed-bed and membrane reactors by analyzing thermodynamic equilibrium with the gas composition calculated from the COMSOL model under different temperatures. The results are shown in Figure 6.13. Coking selectivity is defined as the moles of carbon produced divided by the moles of CH_4 consumed. From the figure, we find that: 1) for the fixed bed reactor, coking selectivity decreases by more than 100% as temperature increases from 970K to 1120K, which is the result of fast reaction kinetics and abundance of CO_2/H_2O in the gas stream. 2) For the membrane reactor, a similar trend with temperature is observed, but the coking selectivity is slightly higher at low temperature and much lower at high temperature than the co-fed fixed-bed reactors. Such improved coking resistance at higher temperature

is due to the excellent CH_4 conversion rate of the membrane reactor. Therefore, we conclude that longer membrane reactor design and higher operating temperature are beneficial to suppress coke formation. Along the CH_4 flow direction of the tubular membrane, as more CO_2 and O_2 are added, coking can be further suppressed.

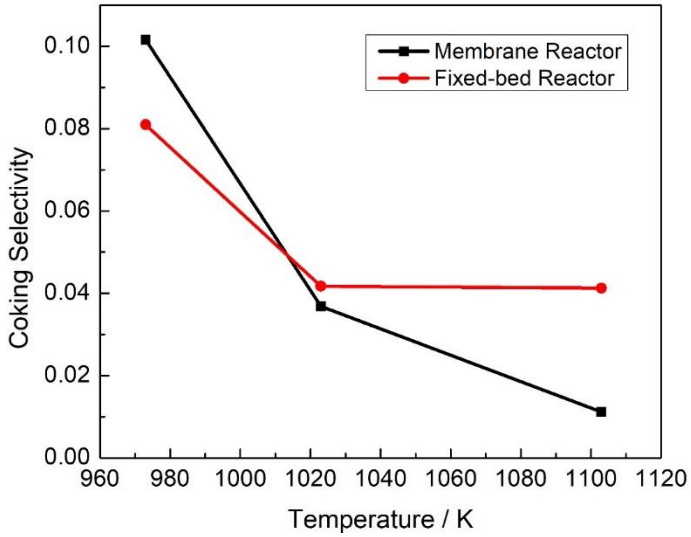

Figure 6.13 Coking selectivity as a function of operating temperature

6.6.5 Direct CO_2 oxidative coupling of methane

For the results presented in section 6.6.1-6.6.3, direct oxidation of methane by CO_2 (reaction 11) has been included. Compared to O_2-OCM (reaction 2), CO_2-OCM is more difficult given the nature of stable CO_2 molecule. However, using CO_2 as an oxidizer for OCM has implications to mitigating CO_2 emission. In recent years, explorative studies on direct CO_2-OCM have reported [34, 131], but with very low C2 yields (3 - 6% depending on CO_2 partial pressure in the gas mixture). In this study, we use the experimental data produced from CaO-modified CeO_2 catalyst [125] to obtain the reaction kinetics parameter for reaction 11 in Table 6.3 and then incorporate the reaction into the models for fixed-bed reactor and membrane reactor. Referring to the C2 yield for OCM with O_2 in Figure 6.13, Figure 6.14 shows that the maximum C2 yield increase vs. temperature of direct CH_4

oxidation by CO_2, which is similar for fixed-bed and membrane reactors, 2.5% for the fixed-bed reactor vs. 2% for the membrane reactor at the highest temperature 1120K and a reactor length of 0.4 m. For longer reactors, there will be longer residence time for CO_2 to react with CH_4. However, it is evident that CO_2-OCM contribution is marginal compared to O_2-OCM, regardless of the type of reactor. New catalysts would be needed to boost CO_2-OCM. As of now, the ability to capture CO_2 and incremental addition of O_2 (diluted by the captured CO_2) into CH_4 stream for OCM are the major advantages for the membrane reactors.

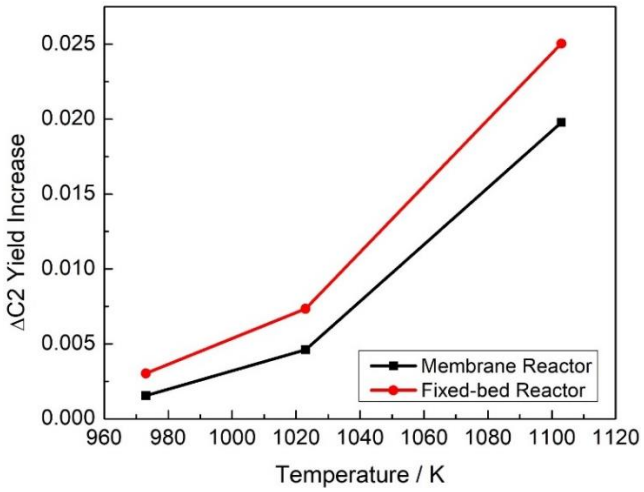

Figure 6.14 C2 yield increase for membrane reactor and fixed-bed reactor considering the OCM by CO_2

6.7 CONCLUSION

In summary, we have developed a membrane reactor model to simulate the performance of a combined CO_2 capture and CH_4 oxidative coupling reaction. The model parameters are obtained by validating experimental data of C2 yield and CH_4 conversion rate from a microcatalytic fixed-bed reactors, as well as CO_2 flux in a lab-scale membrane. The results show that the membrane reactor has the following advantages over its

counterpart fixed-bed reactor design. 1) The membrane reactor can overcome C2 yield limitation faced by the fixed bed reactor under higher operating temperatures or longer reactor length, achieving over 30% C2 yield. 2) CO_2 molar fraction becomes dominant in the membrane reactor product stream, indicating successful capture of the high flux of CO_2 from the flue gas. 3) Longer membrane reactor shows better coking resistance compared to its fixed-bed counterpart design. 4) Direct oxidation of CH_4 by CO_2 could only improve the C2 yield in the membrane reactor by 2%, suggesting that OCM is mainly carried out by O_2. We show that the membrane reactor with high intrinsic CO_2 flux can become an efficient bifunctional device for simultaneous CO_2 capture and CH_4-to-C_2H_4 conversion through OCM reaction. Further technoeconomic analysis will be conducted to assess the commercialization potential of the technology in the future.

CHAPTER 7

PERFORMANCE PROJECTION OF A HIGH-TEMPERATURE CO_2 TRANSPORT MEMBRANE REACTOR FOR METHANE-TO-SYNGAS CONVERSION

This chapter focus on the modeling of a high-temperature CO_2 transport membrane reactor for methane-to-syngas conversion. The traditional approach to produce syngas from methane is to react methane with steam at high temperatures and high pressures. However, this reaction is very energy-intensive and endothermic. A better alternative method is to utilize the CO_2 captured for upgrading CH_4, an abundant and affordable fuel of today, into syngas as precursor for liquid fuels [132-134]and methanol[135]. This method is commonly known as Dry Methane Reforming (DMR). Compared to its rivalry steam methane reforming (SMR) and partial oxidation of methane (POM), DMR is an environmentally friendly catalytic process because it combines two harmful greenhouse gases to make value-added products. The DRM reaction proceeds as follows:

$$CH_4 + CO_2 \rightarrow 2CO + 2H_2 \quad (7\text{-}1)$$

The other commonly used oxidant is pure oxygen, with which "Dry-Oxy Methane Reforming" (DOMR) occurs. The partial oxidation of methane by oxygen reaction is:

$$CH_4 + {}^1/_2\, O_2 \rightarrow CO + 2H_2 \quad (7\text{-}2)$$

In this chapter, the high-temperature CO_2/O_2 co-transport membrane reactor is studied for DOMR process, which involves both CO_2 and O_2 as oxidants to convert methane to syngas and are advantageous in conversion over DMR. Both reaction (7-1) and reaction (7-2) are taken into consideration in the presence of a composite bifunctional catalyst.

Besides these two main reactions, oxidative methane reforming proceeds with a rather complex reaction pathway:[136, 137]; the following reactions occur simultaneously.

$$CH_4 + 2O_2 \leftrightarrow CO_2 + 2H_2O \quad (7\text{-}3)$$

$$CH_4 + O_2 \leftrightarrow CO + H_2O + H_2 \quad (7\text{-}4)$$

$$CO + {}^{1}/_{2}\, O_2 \leftrightarrow CO_2 \quad (7\text{-}5)$$

$$CO + H_2O \leftrightarrow CO_2 + H_2 \quad (7\text{-}6)$$

$$CO_2 + H_2 \leftrightarrow CO + H_2O \quad (7\text{-}7)$$

These reactions are included in the model described in the following section.

7.1 MEMBRANE REACTOR

This modeling work was carried out in the high-temperature CO_2/O_2 co-transport membrane described in Chapter 5. The catalyst used in this work is the metallic Ni-based $Ni_{0.2}Mg_{0.8}O$ containing 1 wt % Pt (NMP) catalyst, which can effectively catalyze the DOMR. The transport membrane of the membrane reactor consists of three phases: Sm-doped CeO_2 as the solid oxide phase, eutectic Li_2CO_3-Na_2CO_3 as the molten carbonate phase and $LiNiO_2$ formed in-situ between NiO and Li_2CO_3 at high temperature as the electronic phase. Flue gas consists of CO_2, O_2, N_2 mixture are fed along the surface of the

membrane reactor, CO_2 and O_2 from the feed gas permeate through the membrane to the permeate side. Methane is fed to the permeate side in the reactor from the inlet. The schematic is shown in Figure 7.1. The annulus of the membrane reactor is filled with catalyst with density 0.5854kg/m^3. At a desired temperature, methane is partially oxidized to CO and H_2 syngas in the presence of catalyst. A 2D axial symmetrical model was built to simulate the performance of a membrane reactor coupled with a catalyst bed. The domain is the same as Figure 6.1 in Chapter 6.

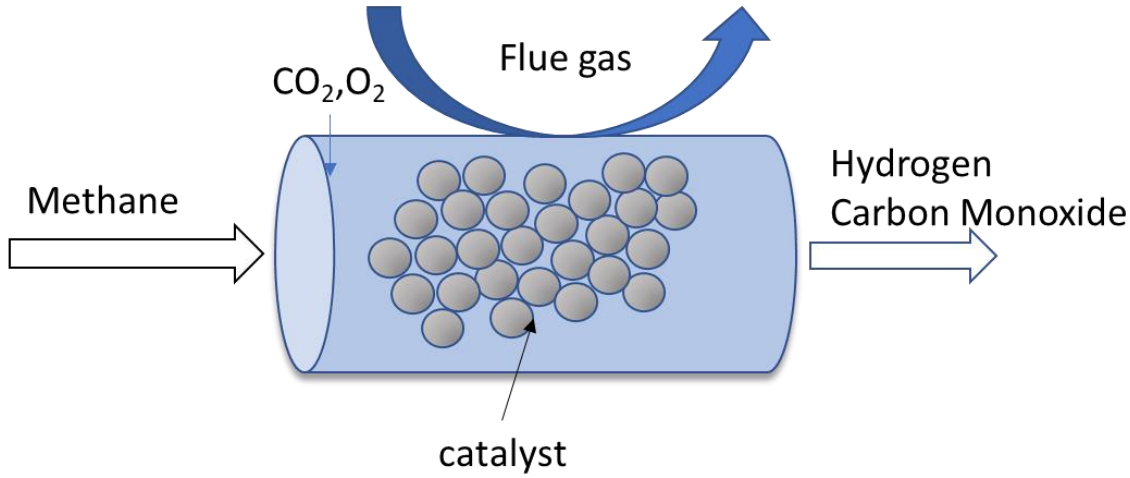

Figure 7.1 Schematic of the membrane reactor for dry-oxy reforming

7.2 MATHEMATICAL MODELS

In this section, more details about the mathematical models to simulate the membrane reactors for DOMR are given. The reaction kinetics of DOMR involve 5 species and 6 reactions in this reactor at the reaction temperature. The corresponding reaction kinetics are listed in Table 7.1. The reaction rate equations are either in Hougen-Watson type (reactions 1-3) or Power law type (reactions 4-6).

Table 7.1 Reaction kinetics of all DOMR reactions

Index	Reaction	Reaction Kinetics
1	$CH_4 + 2O_2 \rightarrow CO_2 + 2H_2O$	$r_1 = \frac{\left(k_{01} \cdot e^{-\frac{E_a}{RT}}\right) \cdot P_{CH4}^{m_1} \cdot P_{O_2}^{n_1} - k_b ve^{-\frac{E_a}{RT}} \cdot P_{CO_2}^{m_1} \cdot P_{H_2O}^{n_1}}{(1 + K_{1,CO_2} \cdot e^{-\frac{\Delta H_{ad,CO_2,1}}{RT}} \cdot P_{CO_2})^2}$
2	$CH_4 + O_2 \rightarrow CO + H_2O + H_2$	$r_2 = \frac{\left(k_{03} \cdot e^{-\frac{E_a}{RT}}\right) \cdot P_{CH4}^{m_3} \cdot P_{O_2}^{n3} - k_b \cdot e^{-\frac{E_a}{RT}} \cdot P_{CO_2}^{m_3} \cdot P_{H_2O}^{n_3}}{(1 + K_{3,CO_2} \cdot e^{-\frac{\Delta H_{ad,CO_2,3}}{RT}} \cdot P_{CO_2})^2}$
3	$CO + 0.5O_2 \rightarrow CO_2$	$r_3 = \frac{\left(k_{04} \cdot e^{-\frac{E_a}{RT}}\right) \cdot P_{CH4}^{m_4} \cdot P_{O_2}^{n4} - k_b \cdot e^{-\frac{E_a}{RT}} \cdot P_{CO_2}^{m_4} \cdot P_{H_2O}^{n_4}}{(1 + K_{4,CO_2} \cdot e^{-\frac{\Delta H_{ad,CO_2,4}}{RT}} \cdot P_{CO_2})^2}$
4	$CO + H_2O \rightarrow CO_2 + H_2$	$r_4 = k_{09} \cdot e^{-\frac{E_{a9}}{RT}} P_{CO}^{m_9} P_{H_2O}^{n_9}$
5	$CO_2 + H_2 \rightarrow CO + H_2O$	$r_5 = k_{10} \cdot e^{-\frac{E_{a10}}{RT}} P_{CO_2}^{m_{10}} P_{H_2}^{n_{10}}$
6	$CH_4+CO_2 \rightarrow 2CO+2H_2$[138]	$r_6 = \frac{\frac{P_{CH_4} \cdot P_{CO_2}}{P_{H_2}^{0.5}} - K_{r,CH_4} \cdot K_{r,CO_2} \cdot k_{r1} \cdot {P_{H_2}}^{1.5} \cdot {P_{CO}}^2}{(1 + \frac{P_{CH_4}}{P_{H_2}^{0.5}} \cdot K_{r,CH_4} + P_{CO_2} \cdot K_{r,CO_2})^2}$

According to the membrane models in chapter 5 and 6, there are three phases, including molten carbonate phase conducting carbonate ions, solid oxide phase conducting oxide ions and the in-situ formed LNO phase conducting electrons. The boundary conditions and governing equations are the same as Chapter 6. The velocity of the gas stream is assumed to be constant, which is 18cm/s.

To evaluate the overall performance of the membrane reactor, two metrics are used, which are methane conversion rate (X_{CH_4}) and CO_2 conversion rate (X_{CO_2}); they are calculated by:

$$X_{CH_4}(\%) = \frac{F_{CH_4}(in) - F_{CH_4}(out)}{F_{CH_4}(in)} \quad (7\text{-}8)$$

$$X_{CO_2}(\%) = \frac{J_{CO_2}(total) - J_{CO_2}(unconsumed)}{J_{CO_2}(total)} \quad (7\text{-}9)$$

7.3 VALIDATION

Validation of the membrane has been done in Chapter 5 and 6. For the reaction kinetics in the catalyst bed of the reactor, validation is done with the experimental data obtained from Zhang's experimental work on DOMR [21]. To be specific, the validation work is done by optimization of the CH_4 and CO_2 conversion rates to fit with the experimental data obtained with NMP catalyst. The experimental and fitting results are shown in Figure 7.2, from which the following reaction rate and kinetic parameter values are obtained:

$$r_{ref} = \frac{k_{r,1} K_{r,CH_4} K_{r,CO_2} (p_{CH4} p_{CO2} / {p_{H2}}^{0.5} - {p_{H2}}^{1.5} p_{CO}{}^2 / K_{ref})}{(1 + p_{CH4} / {p_{H2}}^{0.5} K_{r,CH4} + p_{CO2} K_{r,CO2})^2} \quad (7\text{-}10)$$

$$k_{r,1} = 3.59 \times 10^{21} \exp\left(\frac{284.44}{RT}\right) \quad (7\text{-}11)$$

$$K_{r,CH4} = 2.89 \times 10^{-8} \exp\left(-\frac{16015}{RT}\right) \quad (7\text{-}12)$$

$$K_{r,CO2} = 3.53 \times 10^{-8} \exp\left(-\frac{16000}{RT}\right) \quad (7\text{-}13)$$

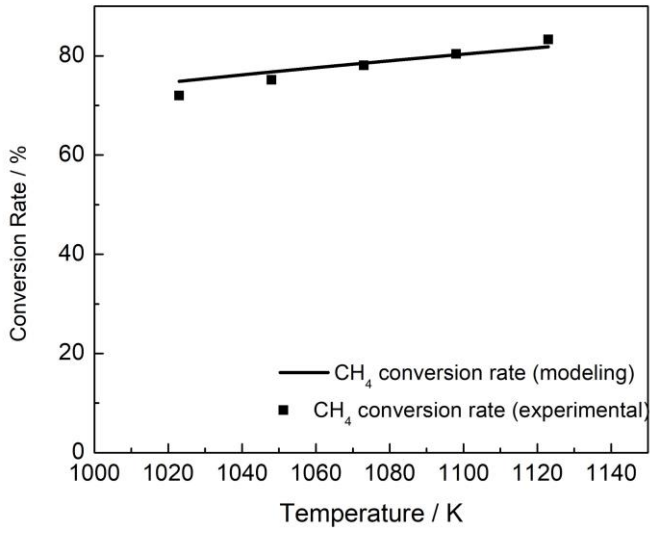

Figure 7.2 Validation of the DOMR kinetics for the membrane reactors with Zhang's data[21]

After the validation, a NMP catalyst is considered in the model of the catalyst bed. It is then used to simulate the performance of the membrane reactor for the DOMR. The material properties and operating conditions in Table 7.2 are also obtained from validation.

Table 7.2 Parameters and conditions of the DOMR validation

Parameter	**Value**
Reactor length	0.4(m)
Reactor inner diameter	0.018(m)
Temperature	850(K)
Pressure	1.1(atm)
Catalyst BET	173(m^2/g)
Catalyst density	0.5854(kg/m^3)
Stream velocity	0.18(m/s)
CO_2 diffusivity	1.39×10^{-4}(m^2/s)
CO diffusivity	1.45×10^{-4}(m^2/s)
O_2 diffusivity	1.52×10^{-4}(m^2/s)
CH_4 diffusivity	1.57×10^{-4}(m^2/s)
H_2 diffusivity	6.20×10^{-4}(m^2/s)

7.4 RESULTS AND DISCUSSION

In this section, the DMR and DOMR on the same membrane reactor are simulated and compared. The purpose of this study is to demonstrate the importance of reactant CO_2 and O_2 contributions to the methane reforming.

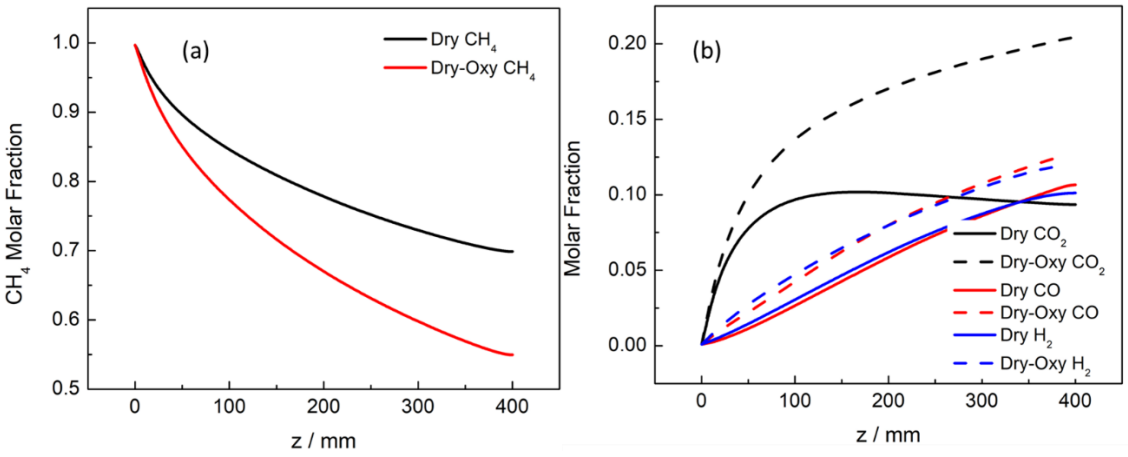

Figure 7.3 Molar fractions profiles of (a) CH_4; (b) Gas species produced from the DMR and DOME reactions

Figure 7.3 shows the molar fraction profiles of CH_4 and CO_2, CO, H_2 along the flow direction in the reactors, when DMR and DOMR reactions are considered in two separate reactor models. It could be seen that CH_4 molar fraction from DMR is generally higher than that of that from DOMR in Figure 7.2a. Therefore, more CO_2, CO and H_2 are produced from DOMR, as shown by the dashed lines in Figure 7.2b.

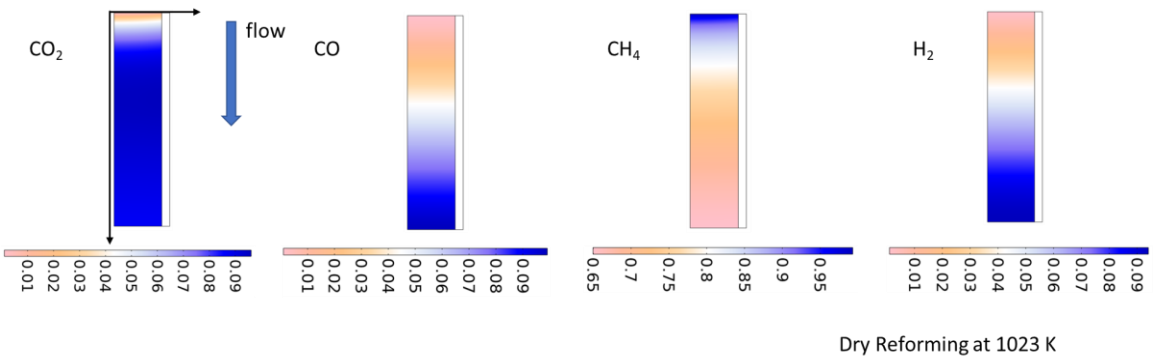

Figure 7.4 2D axial symmetric gas species molar fraction profiles in the membrane reactor under 1023K for the dry reforming reaction

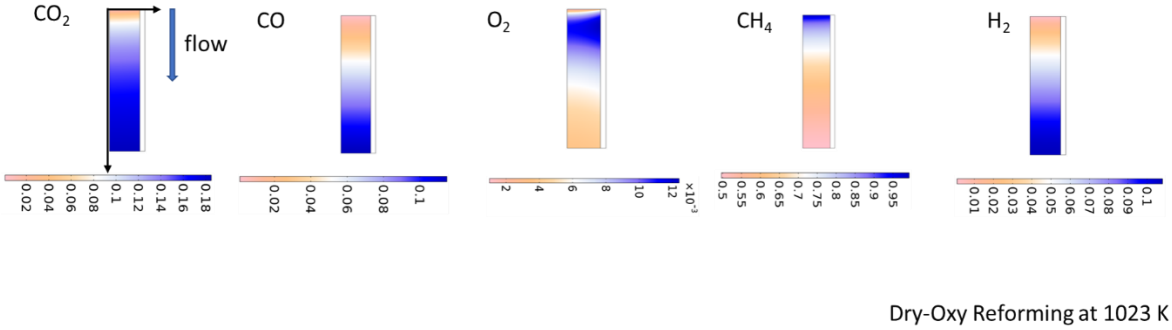

Figure 7.5 2D axial symmetric gas species molar fraction profiles in the membrane reactor under 1023K for the DOMR reactions

Figure 7.4 and Figure 7.5 illustrate 2D axial symmetric molar fraction profiles of gas species in a membrane reactor under 1023K for the DMR and DOMR reactions, respectively. The 2D domain could be revolved around the vertical axis to form a cylinder in 3D. Methane stream is flowing from the top inlet to the bottom outlet of the reactors, while CO_2 or CO_2 and O_2 mixture for DMR or DOMR reactors are permeating through the membrane. It can be seen that methane and CO_2/O_2 have been continuously converted to syngas of CO and H_2 in both reactors. Comparing the profiles of DMR and DOMR reactors, the latter produces more syngas, which is consistent with Figure 7.2b.

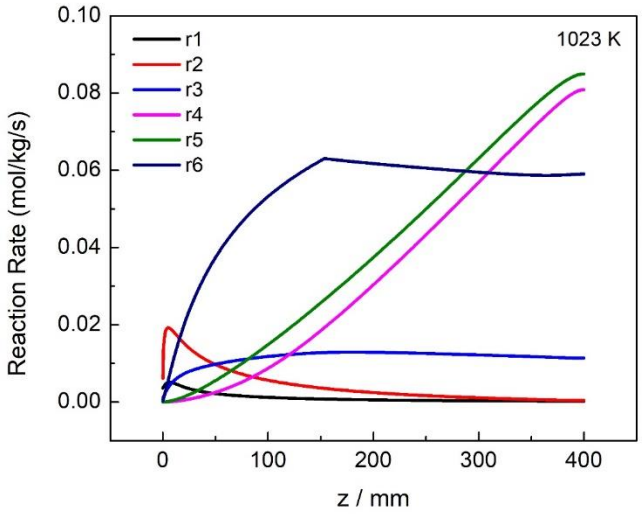

Figure 7.6 Reaction rates of the DOMR reactions under 1023K

Figure 7.6 shows the main reaction rates of the DOMR under 1023K. All the six reactions are considered as catalytic reactions. Among all the six reactions listed in Table 7.1, reactions 1, 2, 6 are the main reactions of methane reacting with CO_2 and O_2. In reactions 3 and 4, CO is further oxidized by O_2 and water, which is undesirable. Reaction 5 is the water gas shift reaction, with reactions 4 as its inverse reaction. Reaction 5 has slightly higher reaction rate than reaction 4.

In conclusion, comparing to the DMR reactor, the DOMR reactor exhibits the following trends: 1) More methane is converted and the methane consuming ratio by CO_2 and O_2 in DOMR reactor is about 2:1. 2) With oxygen introduced, the concentration of all products CO_2, CO and H_2 are increased. 3) Water gas shift reaction is negligible in DOMR reactor model.

7.5 CONCLUSION

In this chapter, we used a 2D axial symmetrical membrane reactor model to study the performance of dry methane reforming and dry-oxy methane reforming reactions. The DOMR reaction kinetic parameters are validated by Zhang's experimental work. DOMR shows higher methane conversion and syngas production rate than the DMR reaction. The DOMR reactor converts 45% of methane while the DMR reactor only converts 30% of methane under the same reactor condition.

CHAPTER 8

CONCLUDING REMARKS

The objectives of this thesis work are synthesis of a new high-temperature mixed oxide-ion, carbonate-ion and electron conducting membrane with enhanced partial O_2 pressure in the permeated CO_2-O_2 mixture and the mathematical modeling of the charge transport in the membrane and conversion in the reactor.

From the experiment, the 6% Mn-doped CeO_2 (MDC) was found to be the upper limit of Mn-doping and exhibit the highest oxide-ion and electronic conductivity. It was, therefore, selected as a part of the matrix material for the high-temperature CO_2/O_2 co-transport membrane to be further evaluated for flux and conversion performance. The MDC-NiO mixture powder was synthesized by co-precipitation method and then used to blend with carbon as pore former to achieve porous matrix after high temperature sintering. A eutectic molten carbonate (MC) was then allowed to fill the pores and in-situ react with NiO to form electronically conducting LNO phase. The best MC loading was determined to be 0.1g for a matrix with 16% porosity, 0.916 cm^2 surface area and 0.75 mm thickness dimension. With this membrane, the flux densities of CO_2 and O_2 were obtained and the CO_2 and O_2 pathways were confirmed by specially designed experiments.

The CO_2/O_2 flux density of four types of multiphase solid/MC membranes for CO_2 transport have been calculated both numerically and analytically. For solids with a single charge carrier, viz. oxygen vacancy or electron, analytical and numerical results are virtually identical. For solids of mixed oxide-ion and electron conductors, numerical methods are preferred over analytical counterparts due to the fact that the nonlinear variations of charge carrier concentrations across the membrane under large chemical potential gradient cannot be solved analytically. From the transport perspective of membranes, the models indicate that without O_2 in the feed, GDC/MC membrane is preferable over YSZ/MC membrane, yielding 4-9 times higher CO_2 flux over a temperature range of 650-850 ^oC and permeate-side pCO_2 range of 0.02-025 atm. With O_2 in the feed, Ag/MC membranes exhibit higher CO_2/O_2 flux than LSCF/MC. This study also reveals that in the new MOEECC membrane including a new separate electron-conducting phase LNO, the CO_2/O_2 flux can be markedly enhanced by the additional electronic pathway and the resultant membrane is virtually a combination of MOCC and MECC membranes.

Finally, a membrane reactor model has been developed to simulate the performance of a combined CO_2 capture and CH_4 oxidative coupling reaction (OCM). The model parameters were obtained by validating experimental data of C2 yield and CH_4 conversion rate from a microcatalytic fixed-bed reactors, as well as CO_2 flux in a lab-scale membrane. The results show that the membrane reactor has the following advantages over its counterpart fixed-bed reactor design. 1) The membrane reactor can overcome C2 yield limitation faced by the fixed-bed reactor under higher operating temperatures or longer reactor length, achieving over 30% C2 yield. 2) CO_2 molar

fraction becomes dominant in the membrane reactor product stream, indicating successful capture of the high flux of CO_2 from the flue gas. 3) Longer membrane reactor shows better coking resistance compared to its fixed-bed counterpart design. 4) Direct oxidation of CH_4 by CO_2 could only improve the C2 yield in the membrane reactor by 2%, suggesting that OCM is mainly carried out by O_2. We show that the membrane reactor with high intrinsic CO_2 flux can become an efficient bifunctional device for simultaneous CO_2 capture and CH_4-to-C_2H_4 conversion through OCM reaction.

REFERENCES

1. Marchetti, C., *On geoengineering and the CO2 problem.* Climatic Change, 1977. **1**: p. 59-68.
2. Adamu, A., F. Russo-Abegão, and K. Boodhoo, *Process intensification technologies for CO2 capture and conversion – a review.* BMC Chemical Engineering, 2020. **2**(1).
3. Rubin, E.S., et al., *The outlook for improved carbon capture technology.* Progress in Energy and Combustion Science, 2012. **38**(5): p. 630-671.
4. Theo, W.L., et al., *Review of pre-combustion capture and ionic liquid in carbon capture and storage.* Applied Energy, 2016. **183**: p. 1633-1663.
5. Jansen, D., et al., *Pre-combustion CO2 capture.* International Journal of Greenhouse Gas Control, 2015. **40**: p. 167-187.
6. Smit, B., *Carbon Capture and Storage: introductory lecture.* Faraday Discuss, 2016. **192**: p. 9-25.
7. Luis, P., T. Van Gerven, and B. Van der Bruggen, *Recent developments in membrane-based technologies for CO2 capture.* Progress in Energy and Combustion Science, 2012. **38**(3): p. 419-448.
8. Wang, M., et al., *Post-combustion CO2 capture with chemical absorption: A state-of-the-art review.* Chemical Engineering Research and Design, 2011. **89**(9): p. 1609-1624.
9. Oexmann, J., et al., *Post-combustion CO2 capture: chemical absorption processes in coal-fired steam power plants.* Greenhouse Gases: Science and Technology, 2012. **2**(2): p. 80-98.
10. Aaron, D. and C. Tsouris, *Separation of CO2 from Flue Gas: A Review.* Separation Science and Technology, 2011. **40**(1-3): p. 321-348.
11. Yu, C.-H., C.-H. Huang, and C.-S. Tan, *A Review of CO2 Capture by Absorption and Adsorption.* Aerosol and Air Quality Research, 2012. **12**(5): p. 745-769.
12. Ramasubramanian, K. and W.S.W. Ho, *Recent developments on membranes for post-combustion carbon capture.* Current Opinion in Chemical Engineering, 2011. **1**(1): p. 47-54.
13. Park, H.B., et al., *Polymers with cavities tuned for fast selective transport of small molecules and ions.* Science, 2007. **318**(5848): p. 254-8.
14. Do, Y.S., et al., *Thermally rearranged (TR) bismaleimide-based network polymers for gas separation membranes.* Chem Commun (Camb), 2016. **52**(93): p. 13556-13559.
15. Park, H.B., et al., *Thermally rearranged (TR) polymer membranes for CO2 separation.* Journal of Membrane Science, 2010. **359**(1-2): p. 11-24.
16. Han, S.H., et al., *Tuning microcavities in thermally rearranged polymer membranes for CO2 capture.* Phys Chem Chem Phys, 2012. **14**(13): p. 4365-73.
17. Budd, P.M., et al., *Solution-Processed, Organophilic Membrane Derived from a Polymer of Intrinsic Microporosity.* Advanced Materials, 2004. **16**(5): p. 456-459.
18. Aroon, M.A., et al., *Performance studies of mixed matrix membranes for gas separation: A review.* Separation and Purification Technology, 2010. **75**(3): p. 229-242.

19. He, X., *A review of material development in the field of carbon capture and the application of membrane-based processes in power plants and energy-intensive industries.* Energy, Sustainability and Society, 2018. **8**(1).
20. Zhang, P., et al., *The current status of high temperature electrochemistry-based CO2 transport membranes and reactors for direct CO2 capture and conversion.* Progress in Energy and Combustion Science, 2021. **82**.
21. Zhang, P., J. Tong, and K. Huang, *Self-Formed, Mixed-Conducting, Triple-Phase Membrane for Efficient CO2/O2 Capture from Flue Gas and in Situ Dry-Oxy Methane Reforming.* ACS Sustainable Chemistry & Engineering, 2018. **6**(11): p. 14162-14169.
22. Li, X., et al., *Removal of Carbon Dioxide from Flue Gas by Ammonia Carbonation in the Gas Phase.* Energy & Fuels, 2002. **17**(1): p. 69-74.
23. Ito, T. and J.H. Lunsford, *Synthesis of ethylene and ethane by partial oxidation of methane over lithium-doped magnesium oxide.* Nature, 1985. **314**(6013): p. 721-722.
24. Keller, G., *Synthesis of ethylene via oxidative coupling of methane I. Determination of active catalysts.* Journal of Catalysis, 1982. **73**(1): p. 9-19.
25. Zavyalova, U., et al., *Morphology and Microstructure of Li/MgO Catalysts for the Oxidative Coupling of Methane.* ChemCatChem, 2011. **3**(6): p. 949-959.
26. Stansch, Z., L. Mleczko, and M. Baerns, *Comprehensive Kinetics of Oxidative Coupling of Methane over the La2O3/CaO Catalyst.* Industrial & Engineering Chemistry Research, 1997. **36**(7): p. 2568-2579.
27. Arndt, S., et al., *Mn–Na2WO4/SiO2 as catalyst for the oxidative coupling of methane. What is really known?* Applied Catalysis A: General, 2012. **425-426**: p. 53-61.
28. Beck, B., et al., *Oxidative coupling of methane—A complex surface/gas phase mechanism with strong impact on the reaction engineering.* Catalysis Today, 2014. **228**: p. 212-218.
29. Narui, K., et al., *Effects of addition of Pt to PdO/Al2O3 catalyst on catalytic activity for methane combustion and TEM observations of supported particles.* Applied Catalysis A: General, 1999. **179**(1-2): p. 165-173.
30. Arndt, S., et al., *A Critical Assessment of Li/MgO-Based Catalysts for the Oxidative Coupling of Methane.* Catalysis Reviews, 2011. **53**(4): p. 424-514.
31. Warren, B.K., *The role of chlorine in chlorine-promoted methane coupling catalysts.* Catalysis Today, 1992. **13**(2-3): p. 311-320.
32. Pak, S. and J.H. Lunsford, *Thermal effects during the oxidative coupling of methane over Mn/Na2WO4/SiO2 and Mn/Na2WO4/MgO catalysts.* Applied Catalysis A: General, 1998. **168**(1): p. 131-137.
33. Shahri, S.M.K. and S.M. Alavi, *Kinetic studies of the oxidative coupling of methane over the Mn/Na2WO4/SiO2 catalyst.* Journal of Natural Gas Chemistry, 2009. **18**(1): p. 25-34.
34. Cai, X. and Y.H. Hu, *Advances in catalytic conversion of methane and carbon dioxide to highly valuable products.* Energy Science & Engineering, 2019. **7**(1): p. 4-29.
35. Lang, J., *Experimentelle Beiträge zur Kenntnis der Vorgänge bei der Wasser- und Heizgasbereitung.* Zeitschrift für Physikalische Chemie, 1888. **2U**(1): p. 161-183.
36. Gadalla, A.M. and B. Bower, *The role of catalyst support on the activity of nickel for reforming methane with CO2.* Chemical Engineering Science, 1988. **43**(11): p. 3049-3062.
37. Pakhare, D. and J. Spivey, *A review of dry (CO2) reforming of methane over noble metal catalysts.* Chem Soc Rev, 2014. **43**(22): p. 7813-37.
38. Mortensen, P.M. and I. Dybkjær, *Industrial scale experience on steam reforming of CO 2 -rich gas.* Applied Catalysis A: General, 2015. **495**: p. 141-151.

39. Usman, M., W.M.A. Wan Daud, and H.F. Abbas, *Dry reforming of methane: Influence of process parameters—A review.* Renewable and Sustainable Energy Reviews, 2015. **45**: p. 710-744.
40. Argyle, M. and C. Bartholomew, *Heterogeneous Catalyst Deactivation and Regeneration: A Review.* Catalysts, 2015. **5**(1): p. 145-269.
41. Wang, S., G.Q. Lu, and G.J. Millar, *Carbon Dioxide Reforming of Methane To Produce Synthesis Gas over Metal-Supported Catalysts: State of the Art.* Energy & Fuels, 1996. **10**(4): p. 896-904.
42. Jang, W.-J., et al., *Combined steam and carbon dioxide reforming of methane and side reactions: Thermodynamic equilibrium analysis and experimental application.* Applied Energy, 2016. **173**: p. 80-91.
43. Zhang, J., H. Wang, and A. Dalai, *Development of stable bimetallic catalysts for carbon dioxide reforming of methane.* Journal of Catalysis, 2007. **249**(2): p. 300-310.
44. Nikoo, M.K. and N.A.S. Amin, *Thermodynamic analysis of carbon dioxide reforming of methane in view of solid carbon formation.* Fuel Processing Technology, 2011. **92**(3): p. 678-691.
45. Arora, S. and R. Prasad, *An overview on dry reforming of methane: strategies to reduce carbonaceous deactivation of catalysts.* RSC Advances, 2016. **6**(110): p. 108668-108688.
46. Miriyala, K. and B.K. Inguva, *Kinetic studies on oxidative coupling of methane to ethylene over catalysts supported by mixed-oxides.* International Journal of Advanced Technology and Engineering Exploration, 2019. **6**(53): p. 92-100.
47. Wang, Z., et al., *Catalytic mixed conducting ceramic membrane reactors for methane conversion.* Reaction Chemistry & Engineering, 2020. **5**(10): p. 1868-1891.
48. Tong, J.H., et al., *Novel and ideal zirconium-based dense membrane reactors for partial oxidation of methane to syngas.* Catalysis Letters, 2002. **78**(1-4): p. 129-137.
49. Zhu, X. and W. Yang, *Composite membrane based on ionic conductor and mixed conductor for oxygen permeation.* AIChE Journal, 2008. **54**(3): p. 665-672.
50. Wang, H., et al., *A Cobalt-Free Oxygen-Permeable Membrane Based on the Perovskite-Type Oxide Ba0.5Sr0.5Zn0.2Fe0.8O3-δ.* Advanced Materials, 2005. **17**(14): p. 1785-1788.
51. Luo, H., et al., *Performance of a ceramic membrane reactor with high oxygen flux Ta-containing perovskite for the partial oxidation of methane to syngas.* Journal of Membrane Science, 2010. **350**(1-2): p. 154-160.
52. Ritchie, J.T., J.T. Richardson, and D. Luss, *Ceramic membrane reactor for synthesis gas production.* AIChE Journal, 2001. **47**(9): p. 2092-2101.
53. Zhu, X., et al., *Partial oxidation of methane to syngas in BaCe0.15Fe0.85O3−δ membrane reactors.* Catalysis Letters, 2006. **111**(3-4): p. 179-185.
54. Markov, A.A., et al., *Reaction control and long-term stability of partial methane oxidation over an oxygen membrane.* Journal of Solid State Electrochemistry, 2010. **15**(2): p. 253-257.
55. Yaremchenko, A.A., et al., *Methane oxidation over mixed-conducting SrFe(Al)O3-delta-SrAl2O4 composite.* Phys Chem Chem Phys, 2007. **9**(21): p. 2744-52.
56. Tan, X., et al., *Oxyfuel combustion using a catalytic ceramic membrane reactor.* Catalysis Today, 2008. **131**(1-4): p. 292-304.
57. ten Elshof, J.E., H.J.M. Bouwmeester, and H. Verweij, *Oxidative coupling of methane in a mixed-conducting perovskite membrane reactor.* Applied Catalysis A: General, 1995. **130**(2): p. 195-212.
58. Chen, C.-s., et al., *Conversion of Methane to Syngas by a Membrane-Based Oxidation–Reforming Process.* Angewandte Chemie, 2003. **115**(42): p. 5354-5356.

59. Sunarso, J., et al., *Perovskite oxides applications in high temperature oxygen separation, solid oxide fuel cell and membrane reactor: A review.* Progress in Energy and Combustion Science, 2017. **61**: p. 57-77.
60. Wade, J., K. Lackner, and A. West, *Transport model for a high temperature, mixed conducting CO2 separation membrane.* Solid State Ionics, 2007. **178**(27-28): p. 1530-1540.
61. Rui, Z., et al., *Modeling and analysis of carbon dioxide permeation through ceramic-carbonate dual-phase membranes.* Journal of Membrane Science, 2009. **345**(1-2): p. 110-118.
62. Zhang, L., et al., *Flux of silver-carbonate membranes for post-combustion CO2 capture: The effects of membrane thickness, gas concentration and time.* Journal of Membrane Science, 2014. **455**: p. 162-167.
63. Chung, S.J., et al., *Dual-Phase Metal−Carbonate Membrane for High-Temperature Carbon Dioxide Separation.* Industrial & Engineering Chemistry Research, 2005. **44**(21): p. 7999-8006.
64. Hammel, E.C., O.L.R. Ighodaro, and O.I. Okoli, *Processing and properties of advanced porous ceramics: An application based review.* Ceramics International, 2014. **40**(10): p. 15351-15370.
65. Kovářík, T., et al., *Synthesis of open-cell ceramic foam derived from geopolymer precursor via replica technique.* Materials Letters, 2017. **209**: p. 497-500.
66. Fraga, S.C., et al., *Steady-state and transient transport studies of gas permeation through dense membranes using on-line mass spectrometry.* Separation and Purification Technology, 2018. **197**: p. 18-26.
67. Kultayeva, S., et al., *Effects of porosity on electrical and thermal conductivities of porous SiC ceramics.* Journal of the European Ceramic Society, 2020. **40**(4): p. 996-1004.
68. Chae, S.-H., et al., *Porosity control of porous silicon carbide ceramics.* Journal of the European Ceramic Society, 2009. **29**(13): p. 2867-2872.
69. Van Soest, J.J.G. and D.B. Borger, *Structure and properties of compression-molded thermoplastic starch materials from normal and high-amylose maize starches.* Journal of Applied Polymer Science, 1997. **64**(4): p. 631-644.
70. Song, J.H. and J.R.G. Evans, *The injection moulding of fine and ultra-fine zirconia powders.* Ceramics International, 1995. **21**(5): p. 325-333.
71. Luyten, J., S. Mullens, and I. Thijs, *Designing with Pores - Synthesis and Applications.* KONA Powder and Particle Journal, 2010. **28**(0): p. 131-142.
72. Colombo, P., C. Vakifahmetoglu, and S. Costacurta, *Fabrication of ceramic components with hierarchical porosity.* Journal of Materials Science, 2010. **45**(20): p. 5425-5455.
73. Ji, S., Q. Gu, and B. Xia, *Porosity dependence of mechanical properties of solid materials.* Journal of Materials Science, 2006. **41**(6): p. 1757-1768.
74. Dong, H. and G.M. Koenig, *A review on synthesis and engineering of crystal precursors produced via coprecipitation for multicomponent lithium-ion battery cathode materials.* CrystEngComm, 2020. **22**(9): p. 1514-1530.
75. Yoshimoto, S., et al., *Independently driven four-probe method for local electrical characteristics in organic thin-film transistors under controlled channel potential.* Rev Sci Instrum, 2011. **82**(9): p. 093902.
76. Choi, K. and D. Kang, *Measurement of Figure of Merit of Thermoelectric Materials.* Journal of the Korean Society for Nondestructive Testing, 2017. **37**(3): p. 192-198.
77. Sherman, S.R., et al., *Combustion-assisted CO2 capture using MECC membranes.* Journal of Membrane Science, 2012. **401-402**: p. 323-332.

78. Zhang, L., et al., *High CO2 permeation flux enabled by highly interconnected three-dimensional ionic channels in selective CO2 separation membranes.* Energy & Environmental Science, 2012. **5**(8).
79. P. Zhang, K.H., *Materials and Processes for CO2 Capture and Conversion*. Electrochemical CO2 Capture and Conversion, ed. W.W. L. Li, K. Huang. 2018: John Wiley & Sons.
80. Wade, J.L., et al., *Composite electrolyte membranes for high temperature CO2 separation.* Journal of Membrane Science, 2011. **369**(1-2): p. 20-29.
81. Tong, J., et al., *Electrochemical separation of CO2 from a simulated flue gas with high-temperature ceramic–carbonate membrane: New observations.* Journal of Membrane Science, 2015. **477**: p. 1-6.
82. Fang, J., et al., *CO2 capture performance of silver-carbonate membrane with electrochemically dealloyed porous silver matrix.* Journal of Membrane Science, 2017. **523**: p. 439-445.
83. Xu, N., et al., *Silver-molten carbonate composite as a new high-flux membrane for electrochemical separation of CO2 from flue gas.* Journal of Membrane Science, 2012. **401-402**: p. 190-194.
84. Zhang, L., et al., *Surface modified silver-carbonate mixed conducting membranes for high flux CO2 separation with enhanced stability.* Journal of Membrane Science, 2014. **453**: p. 36-41.
85. Zhang, P., et al., *Stabilizing a high-temperature electrochemical silver-carbonate CO2 capture membrane by atomic layer deposition of a ZrO2 overcoat.* Chem Commun (Camb), 2016. **52**(63): p. 9817-20.
86. González-Varela, D., B. Alcántar-Vázquez, and H. Pfeiffer, *Structural evolution and reaction mechanism of lithium nickelate (LiNiO2) during the carbonation reaction.* Journal of Materiomics, 2018. **4**(1): p. 56-61.
87. Xu, N., et al., *Mixed Conductors for Electrochemical CO2 Separation.* ECS Transactions, 2012. **45**(1): p. 87-96.
88. Fang, J., J. Tong, and K. Huang, *A superior mixed electron and carbonate-ion conducting metal-carbonate composite membrane for advanced flue-gas carbon capture.* Journal of Membrane Science, 2016. **505**: p. 225-230.
89. Fang, J., X. Jin, and K. Huang, *Life cycle analysis of a combined CO2 capture and conversion membrane reactor.* Journal of Membrane Science, 2018. **549**: p. 142-150.
90. Zhang, P., J. Tong, and K. Huang, *A Study of Low-Cost NiO-MC Dual-Phase Membrane for High-Flux and Selective Electrochemistry-Based CO2Capture.* ECS Transactions, 2017. **80**(10): p. 861-870.
91. Zhang, P., J. Tong, and K. Huang, *Combining Electrochemical CO2 Capture with Catalytic Dry Methane Reforming in a Single Reactor for Low-Cost Syngas Production.* ACS Sustainable Chemistry & Engineering, 2016. **4**(12): p. 7056-7065.
92. Zhang, P., J. Tong, and K. Huang, *Role of CO2 in Catalytic Ethane-to-Ethylene Conversion Using a High-Temperature CO2 Transport Membrane Reactor.* ACS Sustainable Chemistry & Engineering, 2019. **7**(7): p. 6889-6897.
93. Zhang, P., J. Tong, and K. Huang, *Dry-Oxy Methane Reforming with Mixed e–/CO32– Conducting Membranes.* ACS Sustainable Chemistry & Engineering, 2017. **5**(6): p. 5432-5439.
94. Wade, J.L., K.S. Lackner, and A.C. West, *Transport model for a high temperature, mixed conducting CO2 separation membrane.* Solid State Ionics, 2007. **178**(27): p. 1530-1540.

95. Zhang, L., et al., *Fast electrochemical CO2 transport through a dense metal-carbonate membrane: A new mechanistic insight.* Journal of Membrane Science, 2014. **468**: p. 373-379.
96. Wagner, B.J. and S.M. Gorelick, *A Statistical Methodology for Estimating Transport Parameters: Theory and Applications to One-Dimensional Advectivec-Dispersive Systems.* Water Resources Research, 1986. **22**(8): p. 1303-1315.
97. Asadikiya, M. and Y. Zhong, *Oxygen ion mobility and conductivity prediction in cubic yttria-stabilized zirconia single crystals.* Journal of Materials Science, 2018. **53**(3): p. 1699-1709.
98. Hashimoto, S.-i., et al., *Oxygen nonstoichiometry and thermo-chemical stability of La0.6Sr0.4Co1-yFeyO3-δ (y=0.2, 0.4, 0.6, 0.8).* Solid State Ionics, 2010. **181**(37): p. 1713-1719.
99. Atkinson, A., *Chemically-induced stresses in gadolinium-doped ceria solid oxide fuel cell electrolytes.* Solid State Ionics, 1997. **95**(3): p. 249-258.
100. Wang, S., et al., *Electrical and Ionic Conductivity of Gd-Doped Ceria.* Journal of The Electrochemical Society, 2000. **147**(10): p. 3606.
101. Pereira, G.J., et al., *Densification and electrical conductivity of fast fired manganese-doped ceria ceramics.* Materials Letters, 2005. **59**(10): p. 1195-1199.
102. Kang, C.Y., et al., *Preparation, characterization and electrical property of Mn-doped ceria-based oxides.* Solid State Ionics, 2006. **177**(19): p. 1799-1802.
103. Santos, E.L., R. Muccillo, and E.N.S. Muccillo, *Densification and Electrical Conductivity of Mn-Doped CeO2.* Materials Science Forum, 2008. **591-593**: p. 639-643.
104. Kojima, T., et al., *Physical Properties of Molten Li2CO3-Na2CO3(52:48 mol%) and Li2CO3-K2CO3(62:38 mol%) Containing Additives.* Journal of The Electrochemical Society, 2013. **160**(10): p. H733-H741.
105. Molenda, J., P. Wilk, and J. Marzec, *Structural, electrical and electrochemical properties of LiNiO2.* Solid State Ionics, 2002. **146**(1): p. 73-79.
106. Cheng, Z., et al., *Temperature dependence of electrical and thermal conduction in single silver nanowire.* Sci Rep, 2015. **5**: p. 10718.
107. Li, X., G. Xiao, and K. Huang, *Effective Ionic Conductivity of a Novel Intermediate-Temperature Mixed Oxide-Ion and Carbonate-Ion Conductor.* Journal of The Electrochemical Society, 2011. **158**(2).
108. Lin, L.C., et al., *In silico screening of carbon-capture materials.* Nat Mater, 2012. **11**(7): p. 633-41.
109. Pierrehumbert, R.T., *High levels of atmospheric carbon dioxide necessary for the termination of global glaciation.* Nature, 2004. **429**(6992): p. 646-9.
110. Schultz, H., *Climate change and viticulture: A European perspective on climatology, carbon dioxide and UV-B effects.* Australian Journal of Grape and Wine Research, 2000. **6**(1): p. 2-12.
111. Lunsford, J.H., *The Catalytic Oxidative Coupling of Methane.* Angewandte Chemie International Edition in English, 1995. **34**(9): p. 970-980.
112. Schweer, D., L. Meeczko, and M. Baerns, *OCM in a fixed-bed reactor: limits and perspectives.* Catalysis Today, 1994. **21**(2-3): p. 357-369.
113. Wozny, S.J.H.R.G.H.A.-G.G., *Oxidative Coupling of Methane: Reactor Performance and Operating Conditions.* Computer Aided Chemical Engineering, 2010. **28**: p. 6.
114. Kiatkittipong, W., et al., *Comparative study of oxidative coupling of methane modeling in various types of reactor.* Chemical Engineering Journal, 2005. **115**(1-2): p. 63-71.

115. Cruellas, A., et al., *Advanced reactor concepts for oxidative coupling of methane.* Catalysis Reviews, 2018. **59**(3): p. 234-294.
116. Tonkovich, A.L., R.W. Carr, and R. Aris, *Enhanced c2 yields from methane oxidative coupling by means of a separative chemical reactor.* Science, 1993. **262**(5131): p. 221-3.
117. Jašo, S., et al., *Experimental investigation of fluidized-bed reactor performance for oxidative coupling of methane.* Journal of Natural Gas Chemistry, 2012. **21**(5): p. 534-543.
118. Yaghobi, N. and M.H.R. Ghoreishy, *Oxidative coupling of methane in a fixed bed reactor over perovskite catalyst: A simulation study using experimental kinetic model.* Journal of Natural Gas Chemistry, 2008. **17**(1): p. 8-16.
119. Dautzenberg, F.M., et al., *Catalyst and reactor requirements for the oxidative coupling of methane.* Catalysis Today, 1992. **13**(4): p. 503-509.
120. Bhatia, S., C.Y. Thien, and A.R. Mohamed, *Oxidative coupling of methane (OCM) in a catalytic membrane reactor and comparison of its performance with other catalytic reactors.* Chemical Engineering Journal, 2009. **148**(2-3): p. 525-532.
121. Wang, W. and Y.S. Lin, *Analysis of oxidative coupling of methane in dense oxide membrane reactors.* Journal of Membrane Science, 1995. **103**(3): p. 219-233.
122. Kao, Y.K., L. Lei, and Y.S. Lin, *A Comparative Simulation Study on Oxidative Coupling of Methane in Fixed-Bed and Membrane Reactors.* Industrial & Engineering Chemistry Research, 1997. **36**(9): p. 3583-3593.
123. Arinaga, A.M., M.C. Ziegelski, and T.J. Marks, *Alternative Oxidants for the Catalytic Oxidative Coupling of Methane.* Angew Chem Int Ed Engl, 2021. **60**(19): p. 10502-10515.
124. Zhang, P., J. Tong, and K. Huang, *A self-forming dual-phase membrane for high-temperature electrochemical CO2 capture.* Journal of Materials Chemistry A, 2017. **5**(25): p. 12769-12773.
125. Wang, Y., Y. Takahashi, and Y. Ohtsuka, *Carbon Dioxide as Oxidant for the Conversion of Methane to Ethane and Ethylene Using Modified CeO2 Catalysts.* Journal of Catalysis, 1999. **186**(1): p. 160-168.
126. Li, X., K. Huang, and X. Jin, *Mathematical Modeling of High-Temperature Multiphase Solid/Molten Carbonate Membranes for CO2 Capture.* Journal of The Electrochemical Society, 2020. **167**(16): p. 164512.
127. Stansch, Z., *Kinetics for oxidative coupling of methane process over La2O3/CaO catalyst*. 1995, Ruhr-University Bochum, Bochum.
128. Tye, C.T., A.R. Mohamed, and S. Bhatia, *Modeling of catalytic reactor for oxidative coupling of methane using La2O3/CaO catalyst.* Chemical Engineering Journal, 2002. **87**(1): p. 49-59.
129. ToolBox, E. *Air - Diffusion Coefficients of Gases in Excess of Air*. 2018; Available from: https://www.engineeringtoolbox.com/air-diffusion-coefficient-gas-mixture-temperature-d_2010.html.
130. Ginsburg, J.M., et al., *Coke Formation over a Nickel Catalyst under Methane Dry Reforming Conditions: Thermodynamic and Kinetic Models.* Industrial & Engineering Chemistry Research, 2005. **44**(14): p. 4846-4854.
131. Zhang, Y., et al., *CO2 oxidative coupling of methane using an earth-abundant CaO-based catalyst.* Sci Rep, 2019. **9**(1): p. 15454.
132. Ashcroft, A.T., et al., *Partial oxidation of methane to synthesis gas using carbon dioxide.* Nature, 1991. **352**(6332): p. 225-226.

133. Porosoff, M.D., B. Yan, and J.G. Chen, *Catalytic reduction of CO2 by H2 for synthesis of CO, methanol and hydrocarbons: challenges and opportunities.* Energy & Environmental Science, 2016. **9**(1): p. 62-73.
134. He, M., Y. Sun, and B. Han, *Green carbon science: scientific basis for integrating carbon resource processing, utilization, and recycling.* Angew Chem Int Ed Engl, 2013. **52**(37): p. 9620-33.
135. Sun, N., et al., *Effect of pore structure on Ni catalyst for CO2 reforming of CH4.* Energy & Environmental Science, 2010. **3**(3).
136. Vernon, P.D.F., et al., *Partial oxidation of methane to synthesis gas, and carbon dioxide as an oxidising agent for methane conversion.* Catalysis Today, 1992. **13**(2-3): p. 417-426.
137. Wang, B., et al., *Propagating DFT Uncertainty to Mechanism Determination, Degree of Rate Control, and Coverage Analysis: The Kinetics of Dry Reforming of Methane.* The Journal of Physical Chemistry C, 2019. **123**(50): p. 30389-30397.
138. Barroso Quiroga, M.M. and A.E. Castro Luna, *Kinetic Analysis of Rate Data for Dry Reforming of Methane.* Industrial & Engineering Chemistry Research, 2007. **46**(16): p. 5265-5270.